

THE REDUCTION OF DRAG OF TWO-DIMENSIONAL BLUNT-BASED
BODIES BY BLOWING

A Thesis presented to the Department of
Mechanical Engineering.

The University of Manitoba

In partial fulfillment of the requirements
for the Degree of Master of Science in
Mechanical Engineering.

by

A. W. M. Bertels

April 1970.



To

My wife Mimi

whose never ending encouragement made this thesis possible.

TABLE OF CONTENTS

| | Page |
|---|------|
| List of Notation. | I |
| Summary. | IV |
| 1. General Introduction. | 1 |
| 2. The Reduction of the Drag of Cylindrical Blunt-Based Bodies by Blowing. | 2 |
| 2.1 Introduction. | 2 |
| 2.2 Review of Previous Work. | 3 |
| 2.3 Basis of Present Investigations. | 11 |
| 2.4 The Windtunnel. | 14 |
| 2.5 Basic Models, Base Configurations and Bleed Arrangement. | 16 |
| 2.6 Pressure Measurements and Determination of Drag. | 18 |
| 2.7 The Flow Visualization. | 24 |
| 2.7.1 An Improved Streamer Method. | 26 |
| 2.7.2 The Photography. | 33 |
| 2.8 A Flow Model for Separated Base Flows with Fixed Separation Points. | 34 |
| 2.9 Results from Photographic Observations. | 39 |
| 3. Correlation and Discussion of Results for the Pressure Measurements and Flow Visualization. | 45 |
| 3.1 Correlation of Results. | 45 |
| 3.2 The Effect of Base Geometry on Base Pressure and the Entrainment Length in the Absence of Base Bleed. | 48 |
| 3.2.1 The Effect of Chamfer (Boat-tailing) as Compared to the Blunt Trailing Edge. | 49 |
| 3.2.2 The Source Effect. | 50 |

| | Page |
|--|------|
| 3.2.3 The Reattachment Effect. | 51 |
| 3.2.4 The Effect of the Spine Attached to Base Cylinders. | 52 |
| 3.2.5 Base Drag, Base Pressure Distribution and the Entrainment Length for Configurations without the Spine. | 53 |
| 3.2.6 The Effect of the Spine on Base Pressure and the Entrainment Length. | 59 |
| 3.3 Bleed, Base Pressure and the Entrainment Length. | 62 |
| 3.3.1 Bleed Effect on Geometries Without the Spine. | 66 |
| 3.3.2 The Effect of Bleed on Spine Geometries. | 69 |
| 3.4 Concluding Summary of Factors Affecting the Near Wake Structure and its Relation to the Base Pressure. | 71 |
| 4. General Conclusions and Recommendations. | 72 |
| APPENDIX A | 77 |
| A Fluidic Windtunnel Speed Stabilization System. | |
| APPENDIX B | 78 |
| Turbulent Free Shearlayers | |
| List of References | 79 |
| Figures | 81 |

I

LIST OF NOTATION

a lateral spacing of vortices in a vortex street.

b width of the mixing zone.

C_d $\frac{D}{\frac{1}{2}\rho U_\infty^2 d}$, drag coefficient.

C_p $\frac{P-P_\infty}{\frac{1}{2}\rho U_\infty^2}$, pressure coefficient.

C_{Pb} base pressure coefficient.

$C_{P_{sep}}$ pressure coefficient at separation.

$C_{P_{step}}$ pressure coefficient for a step.

$\overline{C_p}$ average pressure coefficient.

C_μ $\frac{U_{bl} \cdot W_{sl}}{U_{\infty t_{max}}}$, bleed coefficient.

c proportionality factor.

C_M $\frac{2t_{max}}{h} C_\mu^2$, momentum coefficient.

D drag.

D_{pr} $\oint p dy$, pressure force.

d body height.

$\frac{db}{dx}$ rate of spread

F streamwise force.

f $\frac{F}{\frac{1}{2}\rho U_{\infty t_{max}}^2}$, streamwise force coefficient.

II

| | |
|-------------------|--|
| G_d | $\left \frac{\Delta C_d}{\Delta C_\mu} \right _{\text{lin}}$, drag gain over the approximately linear portion of a $C_d \sim C_\mu$ curve. |
| h | base height. |
| h_s | transversal spacing of vortices |
| L_d | diffusion length. |
| L_f | length of formation region. |
| l_e | entrainment length |
| l_{spin} | spinning length |
| l_{form} | formation length |
| M | bleed momentum |
| \dot{m}_{bl} | bleed mass flow rate |
| N | vortex shedding frequency on one side of the vortex street. |
| p | static pressure |
| Re | $\frac{U_\infty \times \text{body length}}{v}$, Reynolds number |
| r | = velocity ratio |
| S | $\frac{N \cdot h}{U_{\text{sep}}}$, strouhal number |
| s | step height. |
| t_{max} | model maximum thickness |
| U, u | velocities |
| v | perturbation velocity. |
| W_{sl} | total width of "open" part of the base |

III

| | |
|------------|------------------------------|
| X, Y | coordinates for models. |
| x, y | coordinates for shearlayers. |
| γ | boat-tail angle. |
| Γ | vortex strength |
| δ | boundary layer thickness. |
| Δ | finite change in a quantity. |
| ϵ | eddy or effective viscosity. |
| ϵ | vortex transfer fraction. |
| η | y/x , similarity variable. |
| ν | kinematic viscosity. |
| ρ | fluid density. |
| ϕ_b | base cylinder diameter. |
| χ | experimental constant. |

IV

SUMMARY

The effect of changes in the base geometry and the bleedvents on the drag of blunt-based bodies is investigated at high Reynolds numbers ($Re \approx 10^5$). A maximum drag coefficient $C_d = .640$ and a minimum of $C_d = .270$ is found for very small bleedrates. The previously found drag gain with bleed of $G_d = 3.0$ could be improved to $G_d = 74.0$. Drag variations could be related to the flow pattern in the near wake by means of two newly defined length scales l_e and l_{spin} through the use of a newly developed streamer method. A uniformly valid correlation between l_e and l_{spin} is found which is thought to make the formation of vortex streets behind bluff objects dependent on l_e only.

ACKNOWLEDGEMENTS

The author wishes to acknowledge his appreciation to Dr. J. Tinkler for suggesting the topic and for his valuable criticisms given as thesis advisor. Special thanks to Dr. Azad and Messrs. F. Christian, J. Schink, L. Wilkins, B. Wilton and D. Ruth for their advice and technical assistance.

1. General Introduction

The present study of the drag reduction by blowing is part of a programme concerned with a system for the speed stabilization of a windtunnel, using fluidic devices.

The invention in 1960, of the first fluid amplifiers opened the way for a rapidly expanding new technology now commonly known as fluidics, or fluid amplification. These devices made possible the development of control-and logic systems using only the properties of moving fluids - "pure fluid" systems.

The attractive feature of many now known fluidic devices is that they contain no moving parts and can operate under widely varying environmental conditions giving rise to the expectation of prolonged life and dependability of the systems. In all the devices, use is made of interaction of jets and phenomena relating to separated-and re-attached flows. The application of common sense and imagination to combining these principles has played and still plays an extremely important role in the conception of new fluidic devices and control systems; the investigation here presented is a result of such a development.

It was thought that an automatic windtunnel speed stabilization system using the fluidic principle of no moving parts, would have distinct advantages over partly electrical, partly mechanical systems. The fluidic system basically senses the windtunnel speed and counteracts any changes in the speed by varying the aerodynamic resistance of the tunnel circuit.

The realization of the system requires the development of a number

of devices, namely:

- a speedsensor
- a comparator
- power amplifier
- variable tunnel resistance.

Of these devices the speedsensor incorporating the comparator has been completed and the no-load static performance investigated (Ref. 1).

The power amplifier is under investigation. The variable resistance is proposed to be brought about by two methods: (1) variation of the drag of blunt bodies by means of base bleed, (2) diffuser efficiency control by inducing local separation by blowing. The air supply for the resistances and part of the power amplifier is to be taken from the settling chamber of the windtunnel itself, making those parts of the system independent of external power.

A more detailed description of the speed stabilization system is presented in appendix A.

2. The Reduction of the Drag of Cylindrical Blunt Based Bodies by Blowing.

2.1 Introduction

It is well known that ill-streamlined bodies show a considerable drag compared to well-streamlined bodies. This effect is caused by the inability of the boundary layer to remain attached to the body in the presence of high adverse pressure gradients over the rear part of the body. The flow therefore separates from the body leaving a so called "dead air" region behind the body and a wake which may be periodic. This "dead air" region, having a low pressure, creates a high drag.

Although these effects were extensively reported in the early days of fluid dynamics by Prandtl, von Kármán, Kirchoff, Helmholtz and others, they remained of academic interest only - blunt shapes were simply avoided in aerodynamic design - until quite recently.

Extensive research (Ref. 2) into the drag reduction at supersonic and transonic speeds resulted in the use of airfoils with cut-off trailing edges. Although advantageous at high speeds, they gave rise to a considerable penalty in aerodynamic efficiency at subsonic speeds due to the low lift and high drag characteristics. The high drag is mainly due to the low pressure region immediately behind the body called the base drag. Reduction of the base drag was found to be obtained by a continuous injection of fluid from the base of bodies and even relatively low bleed rates were found to be effective (Ref. 3,4). For use in the speed stabilization system, however, these bleed rates would be high compared to the tunnel mass flow, requiring the search for even more effective bleed modes.

From studying the effects of changes in the geometry of the base and bleedvents, insight into more efficient means of drag reduction by base bleed is anticipated so that higher drag gain, $|\Delta C_D / \Delta C_u|$, than demonstrated in References 3 and 4, can be obtained.

2.2. Review of Previous Work

Although quite a complete review of research on the separated flows behind bluff bodies was presented in 1962 by Nash (Ref. 2), more

recent work is of sufficient importance to be reviewed and its connection with older work noted.

Investigations by Prandtl (Ref. 5) on the flow around bluff objects showed that the flow pattern changed very significantly with Reynolds number. At extremely low Reynolds number ($Re \approx 1$), a flow pattern like the potential flow was observed. A slightly higher Reynolds number up to $Re \approx 50$, was characterized by the separation of the laminar boundary layer, well before the rear stagnation point, forming a stable forced vortex pair (Fig. 1^a). Increasing the Reynolds number beyond $Re \approx 50$ resulted in the vortex pair becoming unstable and the well-known vortex street was formed. This vortex street could be observed for Reynolds numbers beyond the critical value-transition to turbulent boundary layers and turbulent separation - as high as $Re \approx 10^5$ (Ref. 6). Beyond that the value the vortex street broke down and the wake became a periodic.

A close approximation of the behaviour of periodic vortex streets was given by von Kármán using a potential flow solution. He found a unique relationship between the geometry of the vortex street, the strength of the individual vortices and the velocity with which the vortex street moves downstream with respect to the body (Fig. 1^b).

$$U_s = \frac{\Gamma_s}{2a} \tanh \frac{\pi h_s}{a}, \quad (1)$$

where: U_s = velocity of the vortex street relative to the body,

Γ_s = strength of each of the vortices in the street

a, h_s = lateral and transversal spacing of the vortices respectively.

Stability investigations on different geometrical configurations of periodic vortex streets revealed that only one stable condition exists, namely when:

$$\sin\left(\frac{\pi h_s}{2}\right) = 1,$$

$$\text{or } \frac{h_s}{a} = 0.281 \quad (2)$$

Carrying through a time averaged drag calculation by momentum considerations it was found (Ref. 6) that the drag coefficient is given by:

$$C_d = \frac{D}{\frac{1}{2}\rho U_\infty^2 d} = \frac{a}{d} \left[1.59 \frac{U_s}{U_\infty} - 0.63 \left(\frac{U_s}{U_\infty} \right)^2 \right], \quad (3)$$

where: C_d = drag coefficient, D = drag

U_∞ = free stream velocity

$$\frac{U_s}{U_\infty} = \frac{N \cdot a}{U_\infty}, \quad (4)$$

N = vortex shedding frequency on one side

$$\Gamma_s = 2 \sqrt{2} a U_s, \quad (5)$$

ρ = density

d = body height.

Measurements of the frequency and spacing ratio only are needed to calculate the drag.

A method for predicting the frequency and spacing ratio for a given body shape, however, was not available. Attempts to calculate the drag of bluff body shapes resulted in the Helmholtz-Kirchoff free stream-line theory. Basic assumptions of this theory were that in the average the highly turbulent wake could be replaced by a dead-air region at

ambient pressure being separated from the free stream by the free shear layers. These free shear layers were replaced by free streamlines springing from the separation points. For bodies with fixed separation points such as flat plates normal to the stream the potential flow solution obtained by the free streamline theory yielded forebody pressure distributions which resembled the measured distributions. However, the drag values obtained were not in agreement with the observations. Only quite recently (1954) Roshko (Ref. 7) succeeded in obtaining a more satisfactory potential flow solution for the periodic flow around bluff body shapes by joining the free-streamline solution to the von Kármán vortex street as illustrated in Fig. 2. But this solution is also semi-empirical in that one parameter, namely the vortex transfer fraction ϵ has to be determined from experiments. This parameter represents the fraction of the vorticity, shed from the separation points, which enters the vortex street. The rate of flow of vorticity in one shear layer may be found (Ref. 3,4) to be.

$$\frac{d\Gamma}{dt} = \frac{U_1^2 - U_2^2}{2}, \quad (6)$$

where:

U_2 = velocity on the outside of the free shear layer,

U_1 = velocity on the inside of the free shear layer.

The rate of flow of vorticity in one half of the von Kármán vortex street is simply

$$\frac{d\Gamma_s}{dt} = N \cdot \Gamma_s \quad (7)$$

The vortex transfer fraction is therefore

$$\epsilon = \frac{\frac{d\Gamma_s}{dt}}{\frac{d\Gamma}{dt}} = \frac{2N \cdot \Gamma_s}{U_1^2 - U_2^2} \quad (8)$$

Using experimentally determined values of ϵ by Fage and Johansen (Ref. 8), Roshko (Ref. 7) was able to compute fairly accurate base pressures and base drags for certain body shapes.

The vortex transfer fraction ϵ in fact describes quantitatively the transformation of the free shear layers into concentrated vortices and the cancellation of part of the vorticity shed from the separation points by dissipative action in the near wake. It is especially processes like

- entrainment in the shear layers and vortices
- mixing and rolling up of the shear layers,
- dissipation in the near wake

which determine the character of the flow, but which are still very little understood.

Since then, some light has been shed on the problem. It was demonstrated in 1962 by Abernathy and Kronauer (Ref. 9) that two vortex layers which are free to interact are unstable and break down into concentrated vortices. Hence steady reversed flow bubbles behind bluff bodies cannot exist in the presence of disturbances as created by turbulent free shear layers - turbulent wakes are inherently unstable - but may exist in the case of almost disturbance free laminar shear layers (extremely low Reynolds numbers). The mechanics of the formation of eddies for relatively high Reynolds numbers was discussed by Gerrard in 1966 (Ref. 10). He suggested that two characteristic lengths in the near wake determine the structure of the vortex street.

- (a) The scale of the formation region L_f , measured as the horizontal distance between the separation points and the point where irrotational fluid is first drawn across the wake axis
- (b) The width to which the shear layers diffuse before they come together L_d .

These two lengths determine respectively the frequency of shedding and the strength of the vortices. Fig. 3 shows a schematic of the formation process according to Gerrard. The free shearlayer I begins to roll up. The other shearlayer and some irrotational fluid which is gradually entrained in the formation process starts to be drawn into the formation region by the forming vortex I. This fluid is distributed into the directions a, b and c. Part a is entrained by the vortex I, part b by the shearlayer I while part c enters the formation region. As soon as the shearlayers - bearing vorticity of opposite sign - come together, less circulation from the shearlayer I enters vortex I. Finally it is cut-off from shearlayer I and vortex I is shed from the body. Vortex II is then beginning to form. Roshko (Ref. 7.) defined the universal Strouhal number (non-dimensional frequency) as

$$S = \frac{N \cdot d}{U_{sep}} \quad (9)$$

where $U_{sep} = U_{\infty} \sqrt{1 - C_{psep}}$ (9^a)

and U_{sep} = velocity in the free stream at the separation point

C_{psep} = pressure at separation point.

Gerrard discusses how its variation with Reynolds number is due to the behaviour of the turbulent free shearlayers. In appendix B a short treatment of turbulent free shearlayers is presented. It is shown that the volume flow (the entrainment) in the layers is approximately equal to the mean velocity times the width of the shearlayer. The width can be shown to increase linearly downstream even in the presence of streamwise pressure gradients and curvature of the "mean streamlines", as long as the layers possess a similarity behaviour. Because of this linearity and the fact that the velocity at the inner-side of the shearlayers at the separation point is zero Gerrard assumes that the entrainment may be taken to be proportional to $U_{sep} \cdot L_f$ (the length of the shearlayer) if the effects of curvature are neglected. Also, he found experimentally that with changes in Reynolds number the change in vortex strength Γ_s is approximately proportional to the change in turbulent entrainment and, therefore, to $(U_{sep} \cdot L_f)$. From equations (4) and (5) it can be seen that an increase in Γ_s results in a reduction in the frequency N or $(-\Delta N) \propto \Delta(U_{sep} \cdot L_f)$. However, there is an opposing trend. Gerrard found that the frequency of shedding decreases as the diffusion length L_d increases or $(-\Delta N) \propto (\Delta L_d)$. Since for a given body height the position where the shearlayers meet on the centreline (L_f) varies inversely with the rate spread of the shearlayers (L_d) it follows that $L_f \cdot L_d \approx \text{constant}$. It can now be seen that if the entrainment $U_{sep} \cdot L_f$ increases, (lower diffusion) the diffusion length decreases. An increase in entrainment tends to decrease the

frequency but the related diffusion length tends to increase the frequency. This accounts for the almost constant strouhal number with Reynolds number as found experimentally as long as the shearlayers are turbulent and the shedding is periodic ($10^3 < Re < 10^5$).

This description of the vortex formation process and the behaviour of the shearlayers provides a basis for the explanation of the phenomena associated with the behaviour of the shearlayers in the case of wake interference in which artificial means of changing the formation process are used.

The contributions of Bearman and Wood (Ref. 3,4,11) to the understanding of the behaviour of the free shearlayers behind bluff bodies serve as a starting point to the present work. Both authors studied the wake interference due to base bleed and splitter plates on airfoils with more or less elliptical leading edges and cut-off trailing edges, using wide open and partly open bases as shown in Fig. 4. They showed independently that the base pressure coefficient, C_{p_b} , is essentially constant over the base height and increases almost linearly with bleed coefficient, C_μ , for $C_\mu < 0.15$, (Fig. 5^a) resulting in drag reductions in the order of 50%. Increasing the bleedrate beyond $C_\mu = 0.15$ resulted in only slight increases in the base pressure. Also, it was found that the wide open base configuration was the most efficient.

Wake investigations performed on the same models showed that for the base shapes used there was a unique relationship between base pressure and vortex formation distance, L_f , and a dependence on boattail

angle γ . (Fig. 5^b) Splitter plate investigations on the models yielded close agreement with the behaviour shown in Fig. 5^b. This means that for the models used the method of wake interference is irrelevant as far as the base pressure and vortex formation distance is concerned. A clearly defined vortex street appeared to be present if the bleed-rate was small. At bleed rates approaching the bleedrate where the base pressure levels off (Fig. 5^a), the vortex street gradually broke down into an a-periodic, turbulent wake. Fig. 6 shows wake configurations as suggested by different authors for the blunt-based airfoils.

In the case of a fully open base bleed and in the absence of the vortex street, an approximate but almost complete solution for bleed coefficients $0.20 < C_{\mu} < \infty$ is given by Abramovich (Ref. 12) in his theory of coflowing jets. He also indicates that for smaller bleed-rates ($C_{\mu} < .2$) the underlying assumption of constant pressure in the wake is violated due to strong curvature of the separating streamlines. Vortices are formed where the free shearlayers meet. He indicates a strong displacement effect of the outer stream by the free shearlayers which, lowering the pressure at the trailing edge considerably, gives rise to the base drag.

2.3 Basis of Present Investigations

The description of the formation process given in section 202 makes it obvious that attempts to change the base drag must be aimed at interfering with the free shearlayers to modify the entrainment mechanisms, since these completely determine the flow and the shape of

the near wake. The shape of the near wake in its turn, due to its displacement effect on the free stream, determines the base pressure and thus the base drag. As concluded by Zdravkovich, 1969 (Ref. 13) from his recent investigations on the formation of vortex streets at low Reynolds numbers ($Re \approx 100$), it is necessary and sufficient to prevent either the instability (rolling up) of the shearlayers or to decrease the rate of generation of vorticity in order to suppress the formation of vortex streets. These conditions hold also for turbulent shearlayers although some instability will always be present. Combinations of the two mechanisms mentioned above are employed in the present investigation of wake interference by base bleed. It should be mentioned, however, that the instability is not necessarily independent of the rate of generation since the instability, apparently being self induced (Ref. 14,15), would depend on the concentration of vorticity in the shear layers, and therefore on the rate of generation of vorticity.

From the base blowing experiments by Bearman and Wood (Ref. 3,4, and 11) it can be learned that the most efficient wake interference is obtained by direct interference with the shear layers - bleed adjacent to the main stream - as shown in Fig. 6, thus lowering the rate of generation of vorticity and, due to the coupled effects of lowered entrainment and displacement, lowering the base drag. If, however, the interference is not directly with the shearlayers, but with the entrainment mechanisms in the formation region, as is the case with the narrow central base slot configurations mentioned in section 2.2, a less strongly influenced drag

behaviour is found. This is due a) to the formation of vortex pairs behind the solid base shoulders preventing direct interaction of the bleed and the shearlayers and b) the effectively unchanged rate of generation of vorticity at low bleed rates (no or weak vortices behind the solid base shoulders) and the increased rate of generation at high bleedrates (strong vortices behind the solid base areas.)

It is quite obvious but never mentioned explicitly by investigators of base bleed that for a blunt-based airfoil with no boat-tailing as used by Ref. 4 and 11, the highest possible base pressure is attained at a bleedrate for which $C_{\mu}=1$, so that the displacement effect of the airfoil and the wake would be the same as for a semi-infinite halfbody of the same trailing edge thickness. For higher or lower bleed-coefficients the free stream would be displaced outwards; hence a lower base pressure would result.

It was mentioned by several investigators (Refs. 2,3,4,11) that a so called "base cavity effect" was found; the base pressure on models with open unrestricted, hollow bases showed lower base pressures than identical models but with a solid base. This indicates that the base geometry might have an important effect on the base pressure and hence on the drag.

From the foregoing it can be concluded that more efficient wake bleed modes than the ones demonstrated (Refs. 3,4,11) should be aimed at interfering with the free shearlayers only, i.e. bleedvents should be located near the separation points only. Extreme changes in the base

geometry might lead to configurations allowing boundary layer re-attachment which would yield base pressures in excess of the maximum base pressure on the semi-infinite halfbody mentioned before. A model with a number of interchangeable base shapes allowing pressure measurements was therefore to be constructed as reported in detail in section 2.4.

Since a correlation of base pressure behaviour with the flow pattern in the wake is essential for the understanding and explanation of the behaviour of the different configurations, a flow visualization method was to be devised as described in section 2.7.

2.4 The Windtunnel

The windtunnel stabilization system described in appendix A is to be applied to the closed circuit open test section windtunnel of the department of mechanical engineering at the University of Manitoba. The control resistance using base bleed is to be installed in a cylindrical conduit of 18" diameter where the maximum operating speed is 150 ft./sec., but typical operation would be at 100 ft./sec. A first estimate of bodies to produce the drag changes suggested an array of bodies with 6" x $\frac{1}{2}$ " bases. Hence a 6" x 6" open circuit model tunnel in which full size tests on the base bleed cylinders could be performed was designed and is shown in Fig. 7. The Reynolds number based on the basic model chord was $Re = 1.03 \times 10^5$.

Air was taken from the atmosphere into the fan, blown through a flexibly connected rectangular effuser, through the 6" square and 5 ft. long test section, through the one to four area ratio and $4 \frac{2}{3}$ ft. long diffuser to discharge back into the atmosphere. A honeycomb at the fan exhaust straightened the flow. Two single (32 Mesh) screens before and after the flexible coupling, and one double screen at the effuser exhaust were employed to obtain a more uniform velocity distribution.

Two plexiglass windows formed the sides of the test section, from 6" until 36" downstream of the effuser discharge. The upperside of this section was also made of plexiglass, the lowerside of plywood which also contained a circular access door of 4" in diameter. Static pressure tappings were installed at suitable points in the test section in the tunnel floor. A total head tube which could be traversed in vertical direction was installed at 7.5" downstream of the effuser discharge in the vertical centreplane of the tunnel. A total head tube for complete wake traverses was installed at $4\frac{1}{2}$ ft. downstream of the effuser. The result of traverses done with the total head tubes upstream and downstream of the test section are shown in Figs. 8 and 9 respectively.

The suspension of the models described in section 2.5 was achieved by clamping it in between the window panes and securing it by a bolt through one of the panes at 12.5" downstream of the effuser discharge. Bleed intakes and different base configurations could be entered through holes in the window panes. A more detailed description is given in Ref. 22.

2.5 Basic Models, Base Configurations and Bleed Arrangement

A basic model (Fig. 10^a) of .644" maximum thickness, 2.0" chord and with parallel trailing edges (Model I) was used. This model was later modified by grinding a slight boattail angle of 3° onto the trailing edges (Model II, Fig. 10^b). The leading edge was approximately elliptical with a ratio of major-to-minor axis of 3.3. This model was obtained by (Fig. 11) forming a 0.040" thick steel plate around a streamline strut extrusion. The hollow shell thus obtained was fitted with two end plates. In one end plate two 0.50" tubes served as inlets for the bleedflow while the other end plate served as primary attachment of the model in the windtunnel (see Fig. 11). The attachment consisted of a bolt connection through the ¼" plexiglass windowpane of the windtunnel test section.

Thirteen static pressure holes nominally 0.010" in diameter were installed in the centre section of model I and were connected to 1/16" brass hypodermic tubes which were glued to the hollow inside of the model. The tubes were led out of the model through a hole in one of the end plates and cut-off in different lengths to allow easy handling and designation of the pressure hole numbers. Two symmetrically situated bleedvents of different size were obtained by installing a number of cylindrical tubes which were ground to exact dimensions as shown in Fig. 12^a. The tubes were held in position by interchangeable plexiglass rings in the window panes of the tunnel test section. A ¼" long cusped spine could be symmetrically installed behind the base tubes,

yielding configurations as shown in Fig. 12^b. A 0.020" static pressure hole was installed in each tube and a traversing mechanism to which the tubes could be attached allowed both transverse and circumferential pressure measurements on the base cylinders. Additionally, a solid flat base made of wood and a curved hollow base made of 0.010" of shimbrass as shown in Fig. 12^c, each containing one static pressure hole at the model centreline, could be mounted.

Combining model II with the different base cylinders, the spine, the hollow and the flat base yielded configurations similar to those shown in Fig. 12a,b,c.

The bleed flow through the model was "driven by the static pressure difference between the open circuit - closed working section of the windtunnel"(see section 2.4) and the atmosphere using the arrangement shown in Fig. 13. The amount of base bleed was measured with a venturimeter of 0.500" throat diameter which was smoothly connected to two bleed inlet tubes by means of a nominally 1.00" inside diameter flexible plastic hose and a forked copper distributing tube as shown in Fig. 13. The bleedrate could be adjusted by a clamp on the plastic hose. In case of extreme sensitivity of the base pressure to bleed, a .460" plug was inserted into the venturi throat to yield an increased sensitivity of the throat depression to bleedrate. Three deflector vanes were used to obtain a uniform spanwise bleed velocity by adjusting the vanes until at $C_{p,max}$ the base pressure was as uniform as possible. Variations of up to 5% in $C_{p,b}$ were found over 75% of the span for small cylinders and larger cylinders at the centreline while up to 10% variation occurred along the trailing edges for large ϕ_b .

2.6 Pressure Measurements and Determination of Drag

The determination of the forces acting on bodies suspended in an airstream is a relatively simple problem. The following methods are available.

- a) force balance
- b) pressure distribution integration
- c) wake momentum integration

Method (a) could have been used but tends to be complex when air has to be fed to the model. Therefore, methods (b) and (c) remained.

Before the static pressure holes in model I were installed it was attempted to determine the drag by method (c) using the total head traversing mechanism described in section 2.4. It was soon apparent that at such a distance behind the model (approximately 80 base heights) the spread of the wake resulted in a redistribution of the flow over the full height of the tunnel. Integration over the tunnel height including the boundary layers would be necessary to determine the drag; a time consuming operation. Closer to the model this redistribution would not take place and the momentum decrement due to the model resistance would be confined to a relatively narrow wake region. The increased fluctuating components of the velocity, however, would render the total head traversing method less reliable. It is thought that a large error in the drag may result for the bodies under investigation (by using method (c)). Also, due to the likely variation of this error with bleedrate the slope of the measured drag-bleed behaviour might show peculiarities which are

not consistent with the body static pressure behaviour. The discrepancy in drag behaviour as found by method (c) may be detected from the base pressure behaviour, since an increase in base pressure must result in a decrease in drag. Evidence of such a discrepancy can be located in the results of Wood (Ref. 3). A reversal of the slope of drag vs. bleed curve was observed while the base pressure increased with bleed, but remained unexplained.

Wake fluctuations could introduce errors in the body static pressure readings when using method (b). Bearman (Ref. 4) showed that the intensities of the fluctuating components became quite low close to the body. Therefore, the integration of the static pressure distribution would yield reliable results. It was decided to use body static pressure integration to determine the drag.

The pressures were measured using a multitude manometer bank of adjustable inclination, containing ethanol alcohol (s.g. 0.795). Readings of all the pressures on the forebody of the models and the static and total head readings in the tunnel could be taken. The pressure tapping on the base cylinder was displayed and recorded as the cylinder was rotated. This gave the pressure distribution over the base cylinder. Throughout all the tests the inclination of the manometer bank was set at 30° thus increasing the actual pressure differences by a factor two. The pressures could be read to the nearest millimeter.

In Figures 14^a, 14^b and 15^a, 15^b are examples of the pressure distributions plotted versus horizontal X and vertical coordinate Y , for Model I and Model II.

The cases chosen for these figures show the most significant changes in the pressure distributions for the two models to indicate:

- how far upstream, pressure changes due to bleed and base geometry were observed,
- how assumptions regarding the behaviour of the pressure in the vicinity of the bleed slots were arrived at.

Figures 14^a and 15^a show that pressure changes due to bleed and base geometry are "felt" as far upstream as 0.3" or 1.7" from the separation points. More important is it to determine the effect of these changes on the stream wise force acting on the body. Consider unit span of the two dimensional model. The total stream-wise force F , acting on the section is due to the pressure forces D_{pr} and the momentum addition M to the wake by the bleed flow, or,

$$F = D_{pr} - M, \quad (10)$$

where:

$$D_{pr} = \int p dy, \quad (11)$$

$$M = \dot{m}_{bl} U_{bl} \quad (12)$$

assuming U_{bl} is in the X-direction and

p = static pressure on the model

\dot{m}_{bl} = bleed mass flow rate

U_{bl} = bleed velocity at the model trailing edge.

Integrating the static pressure over the forebody and the base of the body and rendering the equations non-dimensional, there is obtained:

$$\frac{F}{\frac{1}{2}\rho_{\infty}U_{\infty}^2t_{\max}} = f = C_d - C_m \quad \text{or,} \quad (13^a)$$

$$f = \bar{C}_{P_{\text{forebody}}} - \bar{C}_{P_{\text{base}}} \left(\frac{h}{t_{\max}}\right) - \left(\frac{2t_{\max}}{W_{sl}}\right) C_{\mu}^2 \quad (13^b)$$

where: \bar{C}_p = average pressure

t_{\max} = model maximum thickness

ρ_{∞} = fluid density, assuming $\rho_{bl} = \rho_{\infty}$

$$C_{\mu} = \frac{U_{bl} W_s}{U_{\infty} t_{\max}} = \text{Non. dim. bleedflow rate} \quad (14)$$

with W_{sl} = total height of open part of the base

h = base height

$$C_d = \bar{C}_{P_{\text{forebody}}} - \bar{C}_{P_{\text{base}}} \left(\frac{h}{t_{\max}}\right) = \text{drag coefficient} \quad (15)$$

$$C_M = \frac{2t_{\max}}{W_{sl}} C_{\mu}^2 = \text{momentum coefficient} \quad (16)$$

The behaviour of C_M can be computed a priori from equation (16) and for the different configurations tested. It is seen that C_M becomes more significant for smaller bleed slots.

Fig. 14^b (Model I) shows that the effect of changes in the base flow character only affects the average forebody pressure by slightly less than the equivalent of 1mm. of ethanol which is negligible compared to the inaccuracy. The same is found for Model II, Fig. 15^b if the pressure changes over the chamfered trailing edges are excluded. Therefore the average forebody pressure was assumed constant and the variations of the pressure over the chamfer were included in the average base pressure considering the base height to be equal to the maximum model thickness t_{\max} . Due to

possible blockage of the bleed slots by connecting tubes no pressure taps could be installed in the region from $\frac{1}{2}$ " upstream of the trailing edge, round the trailing edges, up to the crest of the base cylinders. Therefore assumptions had to be made regarding the pressure behaviour in that region. It was assumed that for all the configurations tested, the pressure over the stepheight - slot width plus trailing edge thickness - was uniform and equal to the pressure at the crest of the cylinder. The pressure distribution over the $\frac{1}{2}$ " upstream of the trailing edge is not significant for Model I (no boat-tail angle), but has a significant contribution to the drag for Model II.

The average pressure on the chamfer was found to be approximately equal to the average base pressure. Thus it was found that the actual change in the drag of the models was adequately represented by the change in the average base pressure only.

The above assumptions simplified the pressure integrations to a great extent since changes due to bleedrate and bleed geometry could be accounted for by integrations over the rear of the models only. Integrations were performed graphically with the aid of a planimeter.

The overall drag behaviour with bleed for the configurations with the blunt trailing edges (no boat-tail angle) is presented in Fig. 16 and the results for configurations with the chamfered trailing edges in Fig. 17. The results for the cases with the spine attached to the base cylinders are shown in Figures 18 and 19, for the blunt and chamfered trailing edges respectively. The maximum contribution of C_M to f (streamwise force) is found to be $C_{M_{max}} = 0.04$ ($\phi_D = .550$ ", $\max. C_u$) which being relatively small is not taken into account.

For the cases without the spine the results are best summarized by separately considering the effects of geometry on the drag coefficient at zero bleed, $C_{d_{C_{\mu} = 0}}$ shown in Fig. 20 and the effects of bleed (Figures 21,22) in the approximately linear portion of the C_d-C_{μ} curves. This linear part was chosen such that the drag coefficient decreased monotonely over the largest possible range of the bleed rate as exhibited by a curve under consideration. Thus was obtained the drag change $\Delta C_{d_{lin}}$, the related bleed rate change ΔC_{μ} and the drag gain,

$$G_d = \left| \frac{\Delta C_d}{\Delta C_{\mu}} \right|_{lin} .$$

It can be seen (Fig. 20) that for the cases with the blunt trailing edge a sharp drag reduction at zero bleed is obtained for cylinders bigger than 0.500". Also a small increase in the drag gain is obtained in that region (Fig. 21). For the chamfered configurations without the spine (Fig. 20) an undulating behaviour was found for the drag at zero bleed in the region from .460" until .520". This was followed by a sharp reduction for base cylinder diameters bigger than .520". In the latter region (.520" and up) the drag gain (Fig. 22) showed a sharp increase from $G_d = 5.6$ at .530" to $G_d = 74.2$ at .550". This increase in gain is essentially due to the extremely low bleedrate required ($C_{\mu} = 0.002$), (See Fig. 22) for a reduction in drag coefficient of 0.156 (30% of the drag at zero bleed.)

The results for the configurations including the spine are not as easily summarized due to the lack of adequately wide linear ranges of the drag behaviour with bleed. In general, the drag at zero bleed is greatly reduced by introducing the spine. The drag gain, however, is

either considerably lower than the configurations without the spine, or varies so widely over the bleed range obtained that an extremely limited linear range results. The lowest drag coefficient of all the geometries tested is obtained using the spine in conjunction with the champhered trailing edge, base cylinder diameter of .520" and $C_{\mu} = 0.036$ (Fig. 19).

A more detailed analysis of the drag behaviour is presented later along with the wake flow patterns for the different configurations.

2.7 The Flow Visualization

In previous chapters it has been discussed that the separated flow over the two-dimensional blunt based models at high Reynolds number as used in the present study, is characterized by a violently fluctuating near wake region, possibly followed by a periodic vortex street or a turbulent wake. Also, because of the high Reynolds number the boundary layers at the separation points would be turbulent, resulting in turbulent free shear layers. The wake interference methods employed were aimed at changing the flow mechanisms in the near wake to bring about considerable changes in the base drag and therefore also in the base pressure. Flow visualization should therefore give insight into the changes in the flow mechanisms due to varying the base geometry and bleed rate.

It is clear that the most important requirement of flow investigation techniques should be the ability to exhibit the main features of the near wake flow. The ability of a visualization method to show flow

phenomena in the far wake might be an important requirement since the amount of instability or the periodicity of the near wake flow should be detectable in the far wake flow. The usefulness of existing methods of flow visualization was considered to be questionable for the reasons discussed below. Broadly speaking the existing methods can be divided into : tracers, like smoke; streamers, using wool or silk tufts; optical methods, based on density variation like the Schlieren, shadow graph or interferometer.

The technique using smoke requires the introduction of the tracer into the flow somewhere upstream of the region which one wants to investigate. Although extremely useful at low Reynolds numbers and low speeds, the diffusive three-dimensional character of the turbulent flow at high Reynolds numbers and high speeds renders the smoke to scattered yielding partly obscured flow patterns. The large amounts of smoke needed to make the smoke dense enough to see at high Reynolds numbers makes the use of it impractical because it becomes difficult to introduce without producing significant disturbances. Also if introduced into the main stream upstream of the separation region, not much detail of the near wake will be exhibited and only part of the far wake flow field. This can be seen from the smoke pictures in References 4 and 13. For the type of configurations presently under investigation, some work has been done on mixing large quantities of smoke with the bleed flow, as reported in Reference 3. A vortex-street was clearly discernible at a certain bleedrate although photography was impractical due to the laboratory rapidly filling up with smoke. It will be obvious however,

that at zero bleedrate no flow patterns can be observed at all.

The well known method of streamers or wool tufts could possibly give some indication of relatively quiet regions with low turbulence levels in the separated near wake but the tufts would not be well detectable in the regions of high turbulence levels because of three dimensional effects. High quality photography of the tufts would therefore not be simple to obtain due to the vague image of the tufts in a highly fluctuating stream. The density sensitive optical methods have been used at Mach numbers greater than 0.4 (Ref. 2), and show some features of the wake flow. The usefulness of these methods has not yet been investigated, but it would be difficult to detect the minute density changes in natural low speed flows and injection of different density fluid might be necessary.

It will be clear that adequate visualization of the near wake in air at high Reynolds numbers using existing methods is almost impossible. Due to the strong need for such a method as emphasized by the above discussion, an improved technique was sought.

2.7.1 An Improved Streamer Method

From an analysis of the existing visualization techniques and the way flow pictures are interpreted, it became apparent that it is necessary and sufficient to determine a two-dimensional instantaneous and time averaged picture of the flow directions at an adequate number of points in the flow field to obtain accurate flow patterns. Too great a sensitivity of a visualization technique to the instantaneous three-dimensional components of velocity in turbulent flows only leads to

27,28,29

Page numbering error.

partly obscured pictures of the flow patterns. These conclusions pointed at a method of clearly distinguishable accurate flow direction indicators capable of showing only the two dimensional instantaneous directions. Also these indicators should be sensitive to the macroscale of the turbulence because this will indicate the amount of instability of the wake flow. Using the above considerations it was thought that small and light, but relatively stiff strips of aluminum foil, suspended in the air stream by a thin wire such that friction with the wire and inertia of the strips would be negligible and such that they could spin and fluctuate in the plane of the main stream only, would satisfy most of the requirements for studying the two-dimensional separated wakeflow.

After attempting a number of different techniques for making the strips and testing their behaviour on a 2" x 2½" wake rake attached to a 0.500" base cylinder as shown in Fig. 23, the results presented in Figures 24^a and 24^b were obtained at a free stream velocity of 100 ft./sec. and a shutter speed of 1/125 sec. The strips were made by folding a rectangular piece (originally 2" x 1", becoming 2" by ½") of aluminum foil (0.001" thick) on a round piano wire of 0.020" in diameter which was covered with a releasing agent. After the cement had set the aluminum strip was removed from the piano wire and cut into approximately 0.020" wide and 0.070" long strips each containing the 0.020" eye left by the piano wire. The strips were then threaded onto 0.003" round piano wires which were attached to the wake rake. Only those strips were retained which were extremely flat, contained only a thin layer of epoxy cement and which

were spinning freely. Only a limited number of useful strips remained. The wires were mounted at different angles with respect to the rake, to yield as much information as possible with the least number of strips and wires. The rake itself was intentionally warped around an axis normal to the base cylinder for the same reason.

Having assumed the strips to exhibit negligible inertia and friction with the wires, they will show the actual instantaneous direction of the flow. Therefore it can be inferred, that strips in a flow which periodically reverses its direction will, if photographed, appear to be either "spinning" (turn 360°) or flip-flopping (turn 180°) if the exposure time is long compared to the cycling time of the oscillating fluid motion, examples of which may be seen in Figures 24^a and 24^b. Direct observations of the flip-flopping shows that at a given instant the strips may point upstream fluctuating violently, then suddenly reverse direction and point downstream. This type of reversal occurs at a relatively low frequency and also apparently takes place at the boundary of regions where strips are spinning.

The pictures shown in Figures 24^a, were taken with the wake rake at different angles with respect to the free stream, and with zero bleed rate. The free stream direction is indicated by the strips attached to the second wire in the top-left picture. Part of the model and the base cylinder are seen in the bottom left corner. The set of strips closest to the body clearly shows the highly turbulent character in the near wake, away from the symmetry axis and a relatively quiet back flow region (bottom right picture) on the symmetry axis terminated by the spinning strips.

The turbulent movement is extremely exaggerated because the supporting piano wire became slack and could not be tightened due to kinks in the wire. It can also be seen from the series of pictures that when the rake is rotated towards the axis, the strips on the second wire gradually start fluctuating indicating they are entering the turbulent wake.

Figure 24^b shows pictures with the wake rake close to the symmetry axis at the same conditions as in Fig. 24^a but at the maximum possible bleedrate. Comparison of the pictures without bleed and with maximum bleed shows the shift in the highly turbulent zone at the symmetry axis away from the body due to base bleed.

The photographs discussed above showed the need for a method of keeping the strips approximately equally spaced for the well tightened wires to avoid vibrations of the wire itself. All the pictures shown in Fig. 24^a are for one (zero) bleedrate only and clearly illustrate the number of pictures of a simple rake needed to obtain quantitative measures of the complete near wake flow pattern. Therefore, a frame containing a grid of strips as shown in Figure 25 was made. The technique of making the strips was similar to the earlier wake-rake but the piano wires were replaced by 0.009" nylon monofilaments because the piano wire kinked easily making it almost impossible to apply a high tension. The strips exhibited more friction on the thicker nylon supports. Widening the eyes of the strips gave limited improvement, some strips would spin freely, some not. Because the near wake was considered to be more important for the analysis of the wake flow changes, extra attention

was given to the first 3" of the frame (closest to the model). In the process of improving this front part, a better method for making the strips was found. A "double sided tape" (plastic tape with glue on both sides) was used instead of the epoxy cement. Well performing strips were obtained and used in most of the front part of the wake frame. Figure 26^a shows the wake frame placed in the tunnel behind the model and held in position by nylon wires.

2.7.2 The Photography

The shape of the grid, as seen in Fig. 25, was chosen for maximum information with the least possible number of wires and strips. At the same time, however, sufficient light reflection from the strips, as seen from the bleed intake sight (Fig. 26) was obtained using one light source pointed to the open side of the grid for photographic purposes.

With the prototype wake rake discussed earlier it was noticed that the quality of pictures was very sensitive to small changes in angle between the light source and the camera. Because of the necessity of having the light source and camera on the same side of the window care had to be taken to avoid extreme reflections in the window pane. The arrangement of camera, grid and light source as shown in Figures 26^a, 26^b was found to yield satisfactory pictures although minor reflections were still present.

The pictures were taken with a 35 mm. camera using a f/2.8 macro-photography lens, allowing close-ups without distortion as close as 2".

Except for the light source the room was darkened so that the only light entering the camera was that reflected from the strips. The light sources used were respectively a 500 watts flood light and a flashlight equipped with a light quantity measuring device which regulated the flash duration from 1/1000 sec. for distant objects down to 1/50,000 sec. for objects closer than 16". The flashlight was used for instantaneous pictures of the rapidly fluctuating strips, the flood light gave a representation of the magnitude of the fluctuations in the flow by using long exposure times compared to the cycling time of phenomena in the wake.

To avoid extreme enlargements of the pictures, the camera was set up at 8" from the centreline of the tunnel. Sufficient depth of field for the 2" deep grid required a small aperture which necessitated a high speed film (1,600 A.S.A.) for the available light, subsequently high contract photographic paper was used for all the printing.

2.8 A Flow Model for Separated Base Flows with Fixed Separation Points

Since the flow pictures obtained with the visualization method described in section 2.7 will yield flow directions at only a limited number of points, it is thought better to suggest general flow-models and to seek confirmation in the pictures. The flow-models are arrived at partly through previous (Ref. 11,13) and partly from the present investigation.

For the case of a fully open model base suggested flow patterns are presented in Fig. 27^{a,b,c,d}. When no bleed fluid is injected into

the base area ($C_u=0$) the flow picture (Fig. 27^a) is assumed to be similar to those for circular cylinder as shown in Ref. 13. It can be seen that vortex A is just shed from the body and draws fluid across the wake assisting the growth of vortex B. The latter, however, has grown so big that shearlayer II starts to entrain fluid from vortex B and also begins to roll up into vortex C. Between the rolling up vortices and the rear of the model, reverse flow is seen to exist. Approximate positions of the boundaries of the shearlayers and also the lines of flow reversal are indicated, thus showing the extent of the viscous entrainment (Shearlayer boundaries are defined similarly to the outer edge of boundary layers.). Downstream of the above described near wake region vortex A is seen to become almost detached from the forming vortices B and C and to enter the fully developed vortex street. Vortex B is then going to be shed under the action of the growing vortex C and the diminishing influence of vortex A. This process repeats itself in time resulting in vortices being shed alternately from above and below the x-axis.

Fig. 27^b shows the effect of the injection of a small amount of bleed fluid. Contrary to the assumptions of Refs. 3,4,11 all this fluid comes out in a two narrow regions at the trailing edges at a high velocity rather than as a uniform stream at the relatively low average bleed velocity (see Ref. 18). This effect is due to the high entrainment rate in the shearlayers and the action of the reversed flow in the near wake. As already observed by several other investigators the bleed gradually shifts the vortex formation process downstream. Detailed information of the flow

processes in the near wake, however, (especially the reversed flow) has not previously been obtained.

The flow pattern depicted in Fig. 27^b shows that between the region where the vortices are formed and the model base a region of fairly steady reversed flow exists. The strength of the vortices entering the vortex street after being formed at the downstream end of the reversed flow region is reduced by bleed.

For a sufficiently high bleed rate a flow pattern as depicted in Fig. 27^c may exist. An almost steady vortex pair is present forming a steady wake bubble. This is followed by a turbulent wake extending to infinity. The regular vortex street has disappeared. It must also be noted that the total mass of bleed fluid is still negligible compared with the entrainment rate in the shearlayers ($C_\mu \ll 1$.)

In comparing Figures 27^a, 27^b and 27^c it is seen that the decreasing vortex strength with bleed results in a gradual reduction of the displacement of the free stream by the near wake flow. This reduced displacement effect would result in higher base pressures and hence in lower drag.

If extreme amounts of bleed fluid are injected the amount of bleed fluid becomes significant, and separates the free stream from a steady vortex pair to form a pattern as proposed in Ref. 4 and shown in Fig. 27^d. This, however, is without confirmation by experimental observations at high Reynolds numbers ($Re \approx 10^5$). At fairly low Reynolds numbers ($Re \approx 250$) it is reported (Ref. 18) that such a flow pattern could be observed for a half body (steady wake flow) for bleed coefficients $C_\mu < 0.15$. It is not expected that much increase in base pressure will take place in going from the situation 27^c to 27^d because in both cases the displacement effect on the mainstream will be approximately the same. For bleed rates higher than $C_\mu \approx 0.20$

and high Reynolds numbers, Abramovich (Ref. 12) reports that the steady wake bubble is absent and that a flow pattern as shown in Fig. 27^e is observed.

The general flow pattern for cases where a base cylinder is introduced is given in Fig. 28. It is basically the same as for the fully open base except for a region close to the cylinder and the fact that the region where vortices are formed is shifted somewhat downstream due to the presence of the cylinders. The effect of the base cylinder on the drag-and-bleed characteristics was discussed in section 2.6. It was found that the main effect of the base cylinder is on the drag at no bleed, the bleed characteristics being hardly affected except for cases of extremely large cylinders. Also the effect of the blunt trailing edge compared to the sharp trailing edge was found to be rather significant. Evidence of the causes of these effects will be given in the detailed discussion of the photographs in section 2.9.

Up to now two length-scales of the near wake region have been used by other authors, namely: the "vortex formation" length (References 3,4,10,11) and the "entrainment" length (Ref. 11). Because of a lack of an adequate physical picture of the formation process, however, somewhat different definitions as to how to determine these length-scales have been used. Also no relation between the entrainment and formation-length could be given. It is thought that the visualization method used in the present investigation yields unique definitions of both and also how they are related. The reason for being able to do this is that in the region where rolling up and shedding takes place, complete periodic reversal of flow direction occurs. The small suspended strips introduced in this region will appear to be "spinning" or "flip-flopping" as may be clearly seen in Fig. 24^b. This region will be called the "spinning" or

"interaction" region. To the left of the "spinning region" (see Fig. 28) a relatively quiet region is seen in which entrainment of the reversed flow into the shearlayers takes place. This is the "entrainment region". To the right of the "spinning region" the vortices shed in the near wake enter the vortex street which, with the visualization method used, will only be visible as a slightly fluctuating wavy flow pattern extending to infinity. The formation region may now simply be defined as the region stretching from the body to the end of the "spinning region". It is noted that each region has two characteristic dimensions, namely the lengths l_{entr} , l_{spin} and l_{form} (See Fig. 28) and a height distribution in Y direction which cannot easily be defined by one single average value. It can be seen that

$$l_{form} = l_{entr} + l_{spin} \quad (10)$$

Since the "spinning region" will disappear when a steady wake bubble is present, it may be concluded that the size of the spinning region relates to the strength of the vortex street. The amount of fluctuation of the entrainment region is also related to the strength of vortex street.

The cases with the spine, the flat base and the hollow base behave quite similarly to the configurations of Fig. 27 and Fig. 28 except for some easily recognized additional peculiarities due to changes in geometry.

2.9. Results from Photographic Observations.

The main purpose of the flow visualization is to provide insight in the behaviour of the base pressure for all the configurations tested. Hence photographs were taken of the flow behaviour of configurations which exhibited sufficiently interesting detail in the base pressure behaviour. Because of the number of configurations tested it was decided to limit the number of pictures for each configuration to three over the range of bleed rates. In some special cases four pictures were taken.

It seemed sufficient to include the cases of wide open base and those for base cylinders with diameters of .460" and over, and also the configurations with the closed-flat base and the closed-hollow base.

The pictures for the study of the effect of bleed were distributed over the bleed rate range such as to yield the maximum amount of information regarding peculiarities in the base-pressure behaviour. At each bleed rate two pictures were taken. One with a slow shutter speed (1/125 sec.) using a floodlight and one using the high speed (1/50,000 sec.) flash unit.

It was expected that in this way the time averaged and the instantaneous behaviour of the flow could be observed. Also, for the cases with the closed base two pictures, one slow and one high speed, were taken. The above procedure yielded a total of 74 pairs of photographs of a sufficient quality to be useful for the analysis of the various flow patterns.

For the confirmation of the flow patterns as suggested in section 2.8, a representative selection of photographs has been made and is presented in Figures 29,35. Regarding the photographs the following should be kept in

mind:

The strips are flow direction indicators and hence are sensitive to $(\frac{U}{U_x})$.

Only the half of the stripgrid closest to the model has been improved as much as possible.

During the process of taking a series of photographs of a configuration some strips would become stuck on the strip spacers. This effect may be readily seen by comparing the slow and the high speed pictures.

The quality of the pictures is very sensitive to the angles between the camera and the light units. Because of small changes in the appropriate angles, a lack of reflected light may result in lost detail especially in the region closest to the body.

Due to the fact that only a limited number of strips is present no extreme detail will be visible in the "spinning region" and the possibly existing vortex street.

In Figures 29^{a,b,c} the configuration with the completely open base and chamfered trailing edges is shown. The bleedrate increases from zero in Fig. 29^a onwards as indicated. Lines of flow direction reversal, the entrainment length and the boundaries of the spinning region are indicated. The lines of flow reversal are found by joining the positions of spinning strips outside the "spinning" region. The spinning of the strips

along this line is caused by the fluctuation of the entrainment region - a strip on the line of flow reversal will alternately be pointing upstream and downstream appearing to be spinning. In the "spinning region" the strips are seen to be spinning or violently fluctuating.

For all bleedrates the shape of the entrainment region appears to be approximately trapezoidal. The flow in the entrainment region is relatively quietly fluctuating with a direction opposite to that of the main flow (reversed flow). Very close to the body, however, the strips are seen to be pointing upwards or downwards indicating transverse flow towards the separation points (trailing edges). Downstream of the entrainment region, the approximately rectangular spinning region is seen. In the "far wake" the strips fluctuate only slightly. As mentioned previously the strips cannot show a vortex street due to the small direction variations in the fully developed vortex street. This is similar to the case of flow visualization in water tunnels using tracers where the camera is stationary with respect to the body.

The effect of bleed on the near wake flow configuration is seen to be twofold. Firstly, the entrainment length increases without the flow pattern inside it being materially changed. Secondly, the spinning region is markedly reduced in size.

The flow pictures shown in Fig. 29^{a, b, c} confirm the suggested flow patterns of Fig. 27^{a, b} except for the detail inside the spinning region shown in Fig. 27^{a, b}. At the highest bleedrate (Fig. 29) it can

be seen that a flow pattern approaching that of Fig. 27^c is obtained although a marked unsteadiness is still present in Fig. 29 .

Flow patterns for cases with blunt trailing edges and two different base cylinder diameters are shown in Figures 30,31 whilst Fig. 32 shows flow patterns for the configuration with chamfered trailing edges and a large base cylinder. Apart from a region close to the rear of the models no significant change of basic flow pattern (as compared with the case of the open base) occurs for any geometry or bleedrate. The effect of the base cylinders can only be expressed in terms of the rear wake characteristics l_e and l_{spin} as will be indicated in the graphical presentation of those parameters. Comparison of the flow close to the rear of the models with the blunt and the chamfered trailing edge (Figures 31 and 32) reveals a marked effect. The floodlight pictures show that in the case of the blunt edge (Fig. 31) rather violent fluctuations are present close to the trailing edges. These fluctuations are not present for the chamfered trailing edges as shown in Fig. 32. This edge effect results in changes in the base pressure as shown before (section 2.6) and consequently also in changes in the lengths l_e and l_{spin} .

Flow pattern changes due to the addition of the spine to the base cylinders can be observed by comparing the previously discussed pictures with Fig. 33 for the blunt ($\phi_b = .460''$) and Fig. 34 for the chamfered trailing edge ($\phi_b = .500''$). For the blunt edge case the effect is mainly to increase the entrainment length and to reduce the size of the spinning region without changing the flow pattern. A more significant effect can be seen in Fig. 34. At zero bleedrate (Fig. 34-) the flow pattern is similar

to the previously discussed configurations except that the reversed flow is highly disturbed. At the maximum bleedrate as shown in Fig. 34, however, it can be seen that the strips close to the trailing edge have become very steady and point in the mainstream direction. The flow in the near wake as a whole is more steady except for a small spinning region. The effect of bleed appears to steady the wake bubble considerably.

To investigate the so called "cavity effect" the closed flat base and the hollow base were examined. The results of the visualization are shown in Fig. 35. The main difference due to the geometry changes is that the hollow bases give a far shorter entrainment length than the flat bases. Also the chamfer (boat-tailing) appears to reduce the fluctuations of the wake. The transverse flow as observed in the case of a fully open cavity (Fig. 29) cannot be seen thus indicating that the flat and hollow configurations behave quite differently from the open base case.

To provide a quantitative basis for a correlation of base flow characteristics the length scales l_e and l_{spin} were measured for all the photographed configurations. The behaviour of those lengths is summarized in Figures 36/46 arranged such as to show the effects of geometry and bleed.

The effect of base cylinder changes on the entrainment length and the spinning length is presented in Figures 36 and 37. The length-scales are rendered non-dimensional by the respective base heights of the

models used. The spacing of the free shear layers at the separation points is taken into account by doing so. As a basis of reference the results for the hollow and the flat bases are also included. Strong changes with base cylinder diameter occur for cylinder diameters greater than 0.460" for both the entrainment and spinning lengths. The blunt and chamfered cases show a similar variation with base cylinder diameter. No special connection between the results for the flat and the hollow bases and those for the variation with base cylinder diameter can be noted. It may be observed that generally speaking the spinning length decreases with increasing entrainment length. The addition of the spine basically alters the behaviour as may be seen by comparing Figures 38 and 39 with Figures 36 and 37. For the blunt edged cases the spine is seen to delay rapid changes in the wake configuration up to a base cylinder diameter of .520". However, minor changes are found for the chamfered cases for diameters greater than .460". It must be noted that the disturbed reversed flow makes determination very difficult. As before, an increase in l_e coincides with a decrease in l_{spin} .

The effect of bleed on the near wake characteristics for the cases without the spine is shown in Figures 40/43. It is found (Figures 40,41) that the entrainment length increases with bleed at roughly a constant rate which is independent of the base cylinder diameter and unaffected by the blunt edge effect. The spinning length (Figures 42/43) generally speaking decreases with bleed. For the blunt edged cases an almost constant rate of

decrease is found for all the base cylinder diameters. For the chamfered cases the spinning length decreases more rapidly with increasing base cylinder diameter. Also the rate of decrease seems to depend on the bleed coefficient C_{μ} .

For the cases with the spine the effect of bleed on l_e and l_{spin} is shown in Fig. 44, 45 and 46. For blunt edged cases the entrainment length (Fig. 44) is found to stay almost constant throughout the bleed range. The behaviour of the entrainment length for the chamfered cases (Fig. 44) depends on the base cylinder diameter and the bleed coefficient in a rather complicated almost random way. The same can be said for both the blunt edged and chamfered cases for the behaviour of the spinning region as shown in Figures 45 and 46. However, the general trend that the spinning length decreases with increasing entrainment length, is maintained for bases with spines.

The detailed analysis of the causes for the behaviour of the length scales l_e and l_{spin} is done in subsequent sections together with the detailed analysis of the pressure distributions over the rear of the models.

3.0. Correlation and Discussion of Results for the Pressure Measurements and Flow Visualization.

3.1. Correlation of Results.

The presentation of the results of the pressure measurements and flow visualization done in the previous sections revealed marked effects

of base geometry changes and bleed. A proper correlation between photographic results and those from pressure measurements should yield the required insight into the behaviour of the base drag. The correlation is treated first to eliminate the dependent variables from the general discussion so that a minimum number of parameters has to be taken into account.

A flat based body with a similar leading edge shape as the present model series was investigated in Ref. 4 with and without a splitter plate and bleed. As mentioned in section 2.1, a linear variation of the average base pressure with h/l_e (The inverse of the non-dimensional entrainment length) was found. A similar result could also be deduced from the results of Ref. 3 for a flat based geometry. The above correlation has been applied to the results of the present investigation with the modified definitions of l_e and l_{spin} . Since for each configuration only three points were obtained for l_e and l_{spin} , no conclusive evidence can be given as to the linearity of curves for configurations comparable to those in References 3 and 4. The correlation is presented in Fig. 47^a. Only those cases which exhibited an approximately linear behaviour have been included being the wide open base configurations. One has to keep in mind that the present bodies have a higher thickness ratio than those of References 3 and 4. Other base geometries did not collapse onto the same curve and also did not exhibit this linear relationship; the correlation C_p vs h/l_e apparently does not apply. Large variations in behaviour exist as may be seen in Figures 47^b and 47^c where is shown base pressure vs l_e/h .

The cause of this discrepancy must be sought in the more complicated effects due to base geometry in the present cases as compared to the simple base geometry used in References 3 and 4. Bearman (Ref. 4) found an almost uniform base pressure distribution over the model height. Some of the present models exhibit extremely large variations in base pressure while some do not, accounting for a more complicated behaviour.

It is thought that no uniformly valid correlation between the average base pressure and the near wake flow characteristics $l_{e/h}$ and $l_{spin/h}$ can be found for the geometries tested. The main reason for not being able to do this is that, as will be explained in more detail later, some effects occur for some base geometries but not for others. Flow conditions at or close to the separation points vary widely due to the geometry changing the behaviour of the free shearlayers, the last effect was absent in the work of References 3 and 4.

It is an understanding of the effects of base geometry on the shearlayer behaviour that may bring about better insight into the drag behaviour of blunt based bodies. A qualitative explanation will be presented of the base pressure results using the interplay of a number of simple effects which are evident from the detailed pressure distributions and wake flow photographs.

In the foregoing no mention is made of any correlation combining the spinning length, the entrainment length and the average base pressure. The reason for this is that within the accuracy of obtaining those lengths a uniformly valid correlation is found to exist between the spinning and

the entrainment length. The correlation is shown in Fig. 48. Data from all the configurations and bleed rates used has been included. Lines indicating the outer limits of the results without the spine have been drawn. It is seen that some, but not all of the results from the spine geometries fall slightly below this line. The more confused wake flow pattern for the models with spines made the assessment of the spinning and the entrainment length more difficult, resulting in a higher uncertainty level. From the above it is concluded that the overall behaviour of the shearlayers is apparently completely determined by the entrainment length only. However, the average base pressure was seen (Figures 47^b, 47^c) to depend very strongly on the base geometry and the entrainment length. Therefore the detailed changes in the flow pattern due to base geometry variations should be taken into account in the analysis of the base pressure and shearlayer behaviour.

It should be noted that since the spinning region is thought to be related to the strength of the vortex street, (see section 2.8) it may due to the dependence of l_{spin}/h on l_e/h , also be expected that the strength of the vortex street is completely determined by the entrainment length.

3.2. The Effect of Base Geometry on Base Pressure and the Entrainment Length in the Absence of Base Bleed.

The average base pressure (base drag) and the entrainment length have been seen to vary in a complicated manner with changes in the base geometry. The following is a qualitative discussion of the relations between base pressure, the base drag and the entrainment length

as influenced by the base geometry changes. For configurations with base cylinders as used in the present investigation the influence is due to four main effects depending on the base configuration. They are treated in the subsequent sections.

3.2.1. The Effect of Champher (boat-tailing) as Compared to the Blunt Trailing Edge.

The result of sharpening the trailing edge is two fold. Firstly, the chamfered edge due to the lower base height (smaller displacement effect) has an inherently higher base pressure (lower base drag) than the blunt-edged configurations. Secondly, the blunt edges show, as discussed in the section on flow visualization, a far more violently turbulent character in the wake close to the trailing edge. It is thought that this is mainly due to the fact that the reversed flow in the entrainment region (see Fig. 49^a, 49^b) to be entrained into the free shearlayers at the separation points, meets the inner edge (adjacent to the bleed slot) of the blunt trailing edge and is deflected due to local separation at this edge. This separation effect corresponds to the observed violent fluctuations. It is anticipated that the effect of local separation will generally speaking delay the formation of the free shearlayer resulting in a greater entrainment length le/h . Since the bleed slot becomes very small for the larger base cylinder diameters, it is to be expected that the above effect may be reduced or even disappear with increasing diameter.

For the chamfered edge cases small step heights -- distance between trailing edge outside and the crest of the cylinder -- result in very pronounced consequences, as will be discussed. Thus, the effect of the trailing edges for not too small a step height is that the chamfered edges give higher base pressures than the blunt-edges. The latter have a greater non-dimensional entrainment length.

3.2.2 The Source Effect

The fairly steady reversed flow pattern present in the entrainment region as discussed in the section on flow visualization is not significantly changed by introducing the base cylinders. However, marked changes in the base pressure and the entrainment length were found. For moderate base cylinder diameters, the effect of the cylinders will be mainly like that of a potential source placed on the centreline at the base radiating fluid against the reversed flow. The effect is -

- (1) to lower the pressure over the main part of the cylinder due to "squeezing" of an almost unaltered amount of reversed fluid to be entrained in the shearlayers, between the cylinder and the shearlayers,
- (2) to displace the "spinning region" downstream due to the cylinder surface at the centre line coming close to the actually forming vortices.

The "squeezing effect" is associated with an acceleration of the reverse flow and consequent low pressure which tends to deflect the shearlayers towards the centreline and give lower l_e/h . The projection of the cylinder into the entrainment region has a tendency to increase the entrainment length which is thought to take place when the diameter is sufficiently large to interfere with the forming vortices. The downstream displacement of the forming vortices in the spinning region being a region of minimum pressure in the wake as was shown in Ref. 4, will tend to increase the base pressure. Evidence of this will be found in the pressure distributions on the cylinder. Since two opposing tendencies are present due to the cylinders, it may be anticipated that depending on the cylinder diameter the effects may either balance or show a dominance of one of the two tendencies.

3.2.3. The Reattachment Effect

When stepheights becomes very small, the shearlayers may become attached to the cylinder. This effect is found to become significant for the chamfered edged cases. When the shearlayer reattaches to the base cylinder a bubble is formed between the shearlayer, the trailing edge and the cylinder. The very low pressures found in the bubble deflect the shearlayer towards the body. The low pressure bubble is followed by a sharp pressure rise going further downstream. The flow remains attached to the cylinder for only a short distance; after which re-separation occurs resulting in a drop in pressure. Together, these effects result in a large variation in base pressure distribution over the cylinder. The attachment of the shearlayer to the cylinder is also associated with shorter entrainment

lengths. When reattachment takes place the boundary layer starts affecting the pressure distribution inside the bubble with variations in the step height. This effect is mentioned in (Ref.17) where it is found that the base pressure for a step is related to the step height s and the boundary layer thickness δ as $C_{p,step} = -0.18 (s/\delta)^{1/3}$. As a first approximation for the present cases it may be assumed that the boundary layer thickness approaching the step is hardly affected by geometry changes. Therefore the base pressure increases with the 1/3 power of the step height. This increase becomes important for small steps.

3.2.4 The Effect of the Spine Attached to Base Cylinders

One effect of the spine is that in the case of separation without local reattachment, the spine works as a splitter plate. J. H. Gerrard (Ref. 10) reports that the cross flow resulting in the shedding of an eddy is less easily set up in the presence of a splitter plate attached to the rear of a cylinder. The splitter plate causes a downstream shift of the formation region. It is also shown that for the ratio of the splitter plate length with respect to the body height increasing towards unity, there is a very pronounced increase in the vortex formation distance whilst for ratios greater than unity, the formation distance decreased again. The spines of the present work are similar to short splitter plates.

A second effect of the spine is that the local reattachment effect may be considerably facilitated by the introduction of the spine. The shape of the spine eases the steep pressure gradient which would be present

at the rear of the cylinder. Some evidence of this has already been given in the discussion of the photographs.

3.2.5. Base Drag, Base Pressure Distribution and the Entrainment Length For Configurations Without the Spine.

For the configurations without the spine the connection between base drag (or average base pressure), the base pressure distribution and the entrainment length is found by comparing the behaviour of those quantities as summarized in Figures 36, 50 & 52. In Fig. 50 the base drag coefficient as given before has been replotted to show the relation with the stepheight because the main features of the drag behaviour are dominated by the effects of the step height on the flow. The extent of the "squeezing effect", the wake displacement and the reattachment effect are also indicated in Fig. 50. Determination of the limits of occurrence of the effects will be discussed. The entrainment length Fig. 36 has not been replotted vs. the stepheight since the main effect is due to the displacement effect by the cylinder on the formation process. Pressure distributions for the blunt and chamfered trailing edge cases are given in Figures 51, 52 respectively.

The "edge effect" discussion in section 3.2.1 causes the drag coefficient (see Fig. 50) for the chamfered cases to be consistently lower for any cylinder diameter than the blunt edged configurations. It is also seen (Fig. 36) that due to this effect the entrainment length l_e is slightly greater for the blunt cases for a fully open configuration

becoming equal to the l_e/h for the chamfered case at $\phi_b = .460''$.

The drag behaviour (Fig. 50) is seen to be similar for the models I and II up to $\phi_{b/h} \approx 0.80$ which is equivalent to $\phi_b = .500''$ for the blunt and $\phi_b = .460''$ for the chamfered trailing edges. The pressure distributions (Fig. 51, 52) also show similar patterns in this range exhibiting gradually lower pressures (increasing drag, Fig. 50) with increasing diameters caused by the "squeezing effect" (section 3.2.2). Due to this effect the entrainment length (Fig. 36) is reduced for cylinders greater than $.460''$ up to $.500''$.

The above decrease in the entrainment length is accompanied by (See Figures 51, 52) a gradual lowering of the pressure on the base cylinder going from the trailing edge towards the centreline ($y=0$) except for a small region close to the trailing edge for larger cylinders. The latter region is thought to be due to small changes in the position of the separation points of the reversed flow on the base cylinders for larger diameters.

The reduced pressure towards the centreline is due to the cylinder surface at the centreline gradually coming closer to the spinning region (minimum pressure region) indicating interference with the forming vortices as discussed in section 3.2.2; the "wake displacement effect" starts to take place as indicated in Fig. 50.

The wake displacement effect as was discussed previously (section 3.2.2) opposes the "squeezing effect" and is seen to sharply increase the entrainment length (Fig. 36) for the blunt trailing edge cases and cylinder diameters greater than $.500''$ up to $.540''$ together with a general increase in pressure as can be seen in Fig. 51 and a related reduction in the drag coefficient (Fig. 50).

The configuration with $\phi_b = .550''$ and the blunt edge shows a slight drop in the entrainment length (Fig. 36). The pressure distribution for this case (Fig. 51) shows that a slight drop in pressure occurs at the trailing edge as compared to the $.540''$ case. However, the step height for the $\phi_b = .550''$ is equal to that for $\phi_b = .500''$ and the chamfer for which as is indicated in Fig. 50 reattachment is observed. The blunt edge case of $.550''$ may therefore be on the verge of reattaching deflecting the shearlayer somewhat resulting in a shorter entrainment length as observed.

Champhering the trailing edge influences the drag for base cylinder diameters greater than $.460''$ under the influence of two effects as noted above. This may be confirmed by examining on Fig. 52 the pressure distribution of a base cylinder diameter of $.460''$ and over. For the case of $.460''$ the low pressure at the centreline indicates the beginning interference with the spinning region. For $\phi_b = .500''$ a significantly lower pressure than for the smaller diameter is found at the trailing edge separation points. Going towards the centreline, a relatively sharp rise in pressure, indicating reattachment as discussed in section 3.2.3, is seen up to approximately 40° on the cylinder measured from the separation points. The reattachment will eliminate the "squeezing effect" the limit being indicated in Fig. 50.

Separation occurs at about 40° resulting in a relatively sharp pressure decrease towards the centreline. The entrainment length tends to be lowered by the reattachment and increased by the wake displacement effect. The result is that only a slight decrease in the entrainment length is

observed as compared to a base cylinder diameter of .460".

The reattachment effect becomes most pronounced for a base cylinder diameter of .520". Extremely low pressures (Fig. 52) occur at the separation point followed by a very sharp pressure rise up to 55° measured from the separation points. This is followed by separation resulting in reduction in pressure going towards the centreline due to the proximity of the spinning region. The extremely low pressure at separation followed by the high pressures after reattachment result in a slight increase in drag (lower average base pressure) for this case as shown in Fig. 50. The wake displacement effect and the reattachment effect oppose each other in the effect on the entrainment length balancing from $\phi_b = .500''$ up to $\phi_b = .520''$ as shown in Fig.36. For increasing base cylinder diameters the chamfered configurations become also influenced by the effect of the boundary layer on the bubble pressure as discussed in section 3.2.3. The pressure at the trailing edge can be seen to increase (Fig. 52) due to this for $\phi_b = .520''$ and also a less sharp pressure rise occurs while the separation points move somewhat closer to the trailing edges ($\theta = 40^\circ$ for $\phi_b = .550''$). The drag coefficient (Fig. 50) is sharply reduced due to the increased bubble pressure. The shift of the separation points towards the trailing edges assists the tendency of the wake displacement effect to increase the entrainment length resulting in the latter to increase (Fig. 36) up to $\phi_b = .540''$. However, it was found that in this case the pressure on the cylinder generally showed larger time wise fluctuations than usual; sudden "jumps" coinciding with a high frequency whistling sound were observed intermittently. Especially certain orientations of the static pressure hole seemed to trigger the instability. It is

thought that the instability is caused by a possible resonance in the very thin trailing edges occurring at proper conditions.

Stable results were obtained for all other base cylinder diameter in the absence of bleed. The peak in the entrainment length as shown in Fig. 36^b is the result of the instability as is the rather undulating behaviour of the pressure distribution (Fig. 52) for this case.

In the discussion of the flow pattern of the flat, hollow and fully open base (section 2.9) it was noted that a very different behaviour was found especially with regards to the conditions at the trailing edges. Due to the form of the visualization grid used, no detail is visible on the centreline at the trailing edge position. The latter information would reveal the complete flow pattern from which better insight in the exact behaviour would be obtained. For the flat, open and hollow base shapes it is thought that particularly the angle between the main stream at separation and the reversed flow towards the separation points determines the development of the free shearlayers downstream (the rate of spread). Also the amount to which the reversed flow in the entrainment region extends into the interior of the body (cavity effect) is thought to determine the inclination of the shearlayer with respect to the main stream. The above conditions will determine the entrainment length and the spread of the shearlayers into the undisturbed stream thus determining the base pressure. There are, however, two opposing trends present. Generally, when the spinning region comes closer to the body lower pressures result. However, for very short entrainment lengths the shearlayers are deflected towards the centreline which tends to increase the base pressure due to a smaller displacement effect on the

mainstream. The above may be used to explain the above configurations. In Fig. 36 the entrainment length for the solid flat base with the blunt edge is seen to be greater than all the other configurations excluding the variation with base cylinder diameter. In this case the mainstream and reversed flow meet each other at right angles. The small boat tail angle is seen to reduce the entrainment length. Presumably this is due to the inclination of the shearlayer towards the axis by the chamfer. The fully open base has been discussed in section 2.9. Transverse flow towards the edges was found to be almost perpendicular to the mainstream. Of course, for this case, the transverse flow is not limited in its direction by the presence of a solid plate allowing a more unrestricted movement of the shearlayer. This results in a reduced $l_{e/h}$. Due to the disturbing effect of the blunt edge (see section 3.2.1) a longer entrainment length is found than for the chamfered case as discussed before. In case of the fully open base the reversed flow hardly seems to extend into the cavity.

For the hollow cases it is thought that at the centreline reversed flow occurs from the hollow base surface to the spinning region as shown in Figures 53^a and 53^b, while away from the centreline the flow is in the direction of the mainstream. Due to this, the angle between the flow in the interior of the entrainment region and the mainstream at the separation points is quite significantly reduced giving an increase in velocity ratio r and hence a reduced rate of spread of the shearlayers (appendix B). Also the hollow may be regarded as a "negative base cylinder" tending to draw in the spinning region instead of displacing it downstream deflecting the shearlayers towards the centreline yielding shorter $l_{e/h}$ as

shown in Fig. 36. However, the hollow shape installed was about 0.010" thick at the trailing edge resulting in a blunt edge even for the chamfered case. It is thought that the effect of the blunt edge will be to have local low pressure regions at the separation points which deflect the shearlayers towards the centreline to give the shorter entrainment lengths for the thicker trailing edge as shown in Fig. 36. It should be noted that the edge effect in the above case is different from the one discussed before in connection with the base cylinders. In the hollow case the outer and inner flows approaching a trailing edge are presumably in the same direction (Fig.53) while for the case with base cylinders (Fig. 49) the flows are almost at right angles with each other. From Fig. 20 it is seen that the base drag for the solid flat base and the open base geometries are fairly close (drags at zero base cylinder diameter are taken to be equal to those for 0.125"). A very significant drag reduction is obtained for the hollow cases. It is thought that the displacement effect of the mainstream becomes significantly less for the hollow based cases as compared to the other two discussed above, due to the reduction in shearlayer spread and the deflection towards the axis yielding higher pressures (lower drags) for the hollow geometries.

3.2.6 The Effect of the Spine on Base Pressure and the Entrainment Length

The results of the drag and the entrainment length behaviour for spine geometries presented previously showed very dissimilar trends for the blunt-and chamfered edge cases. The sensitivity of the near wake flow to the length of the spine with respect to the entrainment length was

pointed out in section 3.2.4. The vastly different behaviour for the cases mentioned above are entirely due to this sensitivity. For the blunt edged cases with the spine the ratio of stream wise distance from cylinder centre to the end of the spine and the base height varied between 0.75 and .82 while for the chamfered cases the range was 0.86 to 0.93. The cases without the spine as discussed in section 3.2.5 generally showed a shorter entrainment length for the chamfered trailing edge cases, therefore relatively speaking, the spine length for the latter configurations is far greater than those for the blunt edged geometries. The result of this was discussed in the section on the flow visualization; the near wake for the chamfered models hardly shows any easily recognized reversed flow region, while a very steady near wake was found for the blunt edged configurations.

The effect of the spine may therefore be summarized as follows. When the downstream tip of the spine is relatively far from the spinning region its function will be to dampen small transverse fluctuations. This will have the effect of increasing the base pressure and therefore "force" the spinning region to form further downstream. Since the spinning region is not close to the body an almost uniform base pressure results as was observed for all the blunt edged models with spine. With the downstream tip of the spine approaching the spinning region as is the case for the chamfered edge configurations the spine interferes directly with the formation of vortices, breaking up the forming vortices into a rather confused highly turbulent near wake. Because of this more confused pattern far less regular, and in the average much smaller fluctuations of the shearlayers

will occur which yielding a smaller displacement effect of the main-stream will result in higher base pressures than in the case of more regular fluctuations.

In Fig. 54 the drag coefficient for spine geometries at zero bleed is shown. The chamfered cases are seen to have considerably lower drag coefficients than the blunt edged configurations. This is caused by the inherently lower drag for the chamfered cases as discussed in section 3.2.1 and also by the far less regular fluctuations in the wake as discussed above. The pressure distribution over the base for the blunt edged cases is not given since the pressure is found to be almost uniform over the base for all cylinder diameters the drag coefficient behaviour given in Fig. 54 being representative. The drag coefficient is seen to be reduced from $\phi_b = .250''$ onwards due to the damping effect of the spine discussed above.

Rather sharp changes occur in the drag coefficient (Fig. 54) and also the entrainment length (Fig. 38) for the blunt cases for larger cylinder diameters. It is thought that this is caused partly by the "squeezing effect" which tends to lower the entrainment length and increase the drag (see section 3.2.2) and partly by the splitter plate action of the spine which tends to counteract any reduction in the entrainment length. The interplay of the above effects yields the behaviour shown from which it may be concluded that for the largest cylinders ($\phi_b = .550''$) and spine combinations the spine action is dominant yielding the very long

entrainment length (Fig. 38) and the low drag coefficient (Fig. 54). The chamfered cases exhibit an almost uniform pressure up to $\phi_b = .500''$ as is shown in Fig. 55. For larger cylinders a gradually more well established reattachment occurs as may be judged from the sharp pressure rise (Fig. 55) starting close to the trailing edges or at the trailing edge itself. After the flow separates from the cylinder the pressure is seen to be uniform due to the irregular confused near wake flow discussed above. The drag behaviour for smaller diameters (Fig. 54) up to $.460''$ is similar to that for blunt edge cases discussed before. For larger diameters the more confused wake makes that any increase in diameter has almost no effect on the entrainment length as can be seen in Fig. 38. Therefore the drag coefficient behaviour is dominated by the reattachment effect mentioned and is seen (Fig. 54) first to reduce the drag when reattachment starts, showing an almost constant drag coefficient when the low pressure peak in the reattachment bubble becomes more significant.

3.3 Bleed, Base Pressure and the Entrainment Length

Previously published work on base bleed considered fluid injection from a central bleed slot. In all cases a downstream shift of the formation of a fully developed wake was found. In the authors opinion no satisfactory explanation of this displacement has been given. Wood (Ref. 11) concludes in the case of unsteady base flow that "the increased length of the base flow region with bleed and the associated increase in length of the shearlayers is necessary in order to entrain the additional bleed fluid." Similarly Leal and Acrivos (Ref. 18) in the case of steady base flows con-

clude: "if the bleed coefficient C_μ is small, the amount of fluid being supplied into the near wake is not sufficient to satisfy the entrainment needs of the shearlayers hence a closed vortex region should form downstream." An explanation of the "stretching" of the near wake region was not given.

Both statements have in common that no account is taken of the possibility that the bleed might reduce the "entrainment" need. The "need" for additional entrainment in case of bleed is not adequately linked to the "stretching" of the shearlayers. A more satisfactory explanation of base bleed induced vortex formation displacement can be given by taking the detailed shearlayer behaviour into account. It was found (appendix B) that the rate of spread decreases almost linearly with increasing velocity ratio $r = \frac{U_{bl}}{U_{sep}}$ to $r \approx 0.35$ after which it was virtually constant for normally found windtunnel free stream turbulence levels. The reduction in the rate of spread from $r=0$ to $r=0.35$ amounts to approximately 50%. The reduction in spread with increasing velocity ratio is thought to account for the increasing entrainment length with bleed. In Fig. 56 simplified flow patterns are given. In the case of a central bleed slot occupying the complete base height the flow pattern at zero bleed rate is shown in Fig. 56^a.

The shearlayers spread fairly rapidly and a short entrainment length results due to the velocity ratio at separation being zero. When bleed fluid is injected (Fig. 56^b) the opposing reversed flow deflects the bleed flow in the direction of the separation points so that in fact two narrow bleed jets are formed adjacent to the mainstream. Since the velocity ratio

at separation is increased by the bleed flow (being close to $r \approx C \frac{h}{\mu \text{ slotheight}}$) a reduced spread of the shearlayers from the separation points onwards results as shown (Fig. 56^b) for some distance. This is the distance over which the bleed fluid is entrained by the main stream. Going further downstream the shearlayers also start to entrain fluid from the reversed flow region. It is expected that the rate of spread in this region is dominated by the velocity ratio between the reversed flow and the mainstream and will therefore be the same as that for $r=0.0$ (see appendix B for $r<0.0$). The described shearlayer development results in a longer entrainment length than in the case of zero bleed. Since this means that the spinning region is formed further downstream, a higher base pressure results due to the expectedly smaller influence at the body of the forming vortices in the spinning region.

When a cylinder is present at the base a similar situation results. At zero bleed the flow pattern (Fig. 56^c) is deformed by the cylinder as indicated. The spread of the shearlayer is virtually the same as for the wide open base. When bleed fluid is allowed to enter the wake, again two narrow jets are formed due to the deflection by the reversed flow (Fig. 56^d). Also, the shearlayer spread is reduced over a considerable distance downstream followed by a more rapid spread when reversed flow starts to be entrained. As before a longer entrainment length than without bleed is obtained and hence higher base pressures.

It can be seen that the downstream displacement of the spinning region is mainly due to the reduced spread and therefore depends on the velocity ratio at separation and also on the width of the bleed jet. To a first

approximation the above dependence is proportional to the amount of fluid injected ($U_{bl} \times$ slot height) divided by mainstream velocity U_{sep} .

Although the mainstream velocity depends on the pressure at separation according to

$$U_{sep} = U_{\infty} \sqrt{1 - C_p},$$

the above displacement may be taken to be proportional to

$$C_{\mu} = \frac{U_{bl} \times w_{sl}}{U_{\infty} \times \text{model thickness}}.$$

In the case of significant base pressure changes, variations of the above approximate proportionality to C_{μ} are to be anticipated for geometries as shown in Fig. 56. Also, when the bleed slot becomes very small the bleed velocities become large (order of U_{sep}) and increased base pressures are found together with longer displacements.

For the cases with the spine the above result is not expected to hold, due to the generally more confused flow pattern. Also, for cases where reattachment takes place the above does not apply. In the case of reattachment the bleed interferes with the relatively small closed bubble at the trailing edges. Similar to the bleed effect on the reversed flow in the wake, Fig. 56^a, 56^b, the bleed will reduce entrainment in the bubble gradually stretching the bubble stream wise. The reduced entrainment will result in a higher bubble pressure. Since the bubble is small, very little bleed fluid will be needed to cause the changes.

3.3.1 Bleed Effect on Geometries Without the Spine

It was previously found that generally speaking the entrainment length increased approximately linearly with bleed coefficient at a rate which is virtually independent of cylinder diameter. As was noted in section 3.3, the velocity ratio and therefore the base pressure and the slot height at the separation points will have some effect on the linearity. However, no major effects are anticipated as long as no reattachment occurs or the spine is not introduced. The behaviour of the pressure distributions in the absence of reattachment can be easily summarized by referring to Figures 51 and 52. No reattachment takes place at zero bleed for all the blunt edged cases and the champhered configurations up to 0.460". For those models the pressure is seen to be not too far from uniform. The small variations being due to the effects discussed in section 3.2.5. When bleed is increased it is found that the distributions become gradually more uniform except for a small effect due to the bleed jet staying attached up to $\approx 20^\circ$, close to the separation points, an example of which is given in Fig. 57.

The average pressure behaviour and therefore the drag behaviour for those configurations is representative of the influence of bleed. The drag gain defined as $\frac{\Delta C_d}{\Delta C_\mu}$ was found to stay roughly the same for the configurations under consideration except for larger diameters, as was shown in Fig. 24 and 25. The constant drag gain may be explained as follows. The bleed rate change ΔC_μ is found to be proportional to $\Delta l_{e/h}$ (see section 3.3). The downstream shift of the spinning region $\Delta l_{e/h}$ (low pressure region) will also to a first approximation, result in a proportional increase

in pressure at the base (lower C_d) almost independent of the geometry. Therefore the almost constant rate of drag reduction with bleed as found is due to almost linear changes in both C_d and C_μ with the l_e/h . For larger diameters (for the blunt cases) bleed velocities become relatively high resulting in longer displacement of the spinning region for a given bleed rate than for larger bleed slots as noted before. This increased displacement results in an increased pressure rise which in turn yields more reduction of the drag for the larger cylinders. Therefore the gradually increasing drag gain with diameter for ϕ_b greater than .500" for the blunt configurations as was found in Fig. 24 is due to this effect; smaller slots result in higher drag gain.

The generally higher base pressures for the chamfered cases reduce U_{sep} so that for a given C_μ the velocity ratio at separation is increased. Therefore the chamfered cases up to .460" have slightly higher drag gains than blunt models as can be seen by comparing Figures 24 and 25.

For the chamfered cases at zero bleed rate it was found that reattachment starts for $\phi_b = 0.500"$. An example where the different effects of bleed for cases with reattachment are most clearly exhibited is given in Fig. 58. At zero bleed rate the low pressure in the bubble and the consequent pressure rise due to reattachment are seen. This is followed by separation from the cylinder at 40° which yields a pressure drop going further towards the centreline. When extremely small amounts of bleed are allowed to enter, such that it is negligible with respect to the entrainment in the reattached boundary layer on the cylinder, the following effects happen at the same time; the bubble pressure rises due to the bleed, the separation

point on the cylinder moves back towards the bubble causing as can be seen from Fig. 41 the entrainment length to increase so that the spinning region moves rapidly away from the body.

The result is that the whole pressure level increases sharply resulting in a rapid drag reduction for very small amounts of bleed. This trend continues until the amount of bleed fluid injected completely eliminates the bubble ($C_{\mu} = .0059$). Reattachment does not take place; the bleed fluid separates from the cylinder almost directly at the bleed slot as may be judged from the constant pressure over 20° from the separation points in the case of $C_{\mu} = .0059$ shown in Fig. 58. The case of $C_{\mu} = .002$ coincides with the drag minimum as shown in Fig. 20. An increase in bleed rate causes the flow which is at the point of reattaching at $C_{\mu} = .0059$ (expectingly curving towards the body) to become more fully separated by displacing the mainstream outwards, lowering the pressure. The increase in drag as shown in Fig. 20 results up to a point where, as may be calculated from C_{μ} and the slot width, the velocity ratio at separation comes close to $r=1$. The increase in drag starts to level off and reaches a local maximum. Bleed rates beyond the value at this maximum begin to show signs of reattachment as a wall-jet as can be seen in Fig. 58. From the trailing edge onwards at $C_{\mu} = 0.014$ ($r \approx 1$) a slight increase in pressure is seen up to 30° . At higher bleed rates the bleed forms a well defined wall-jet with the bleed fluid at higher velocity than mainstream. The wall-jet accelerates fluid from the mainstream by entrainment so that a pressure drop occurs over a distance from the trailing edge down stream ending at 10° from the edge (Fig. 58). Judging from the pressure distribution at the highest bleed rates, the jet appears to stay attached up to $\approx 30^{\circ}$, followed by separation.

This delay of separation causes an increase in pressure (decrease in drag) as is shown in Fig. 20 for bleed rates in excess of $C_{\mu} = 0.014$.

The above mechanisms connected with reattachment also occur for smaller base diameters than the one discussed but not in the same distinct fashion. This is exhibited by the drag behaviour with bleed (Fig. 20) of configurations with diameters decreasing from $\phi_b = .550''$ to $.500''$ but to an increasingly smaller degree. Finally a behaviour as discussed prior to the reattachment effect is present at $\phi_b = .460''$ for smaller diameters.

3.3.2 The Effect of Bleed on Spine Geometries

At zero bleed rate it was found that the spine interfered with the reversed flow. For the smaller ratio of spine and base cylinder to body height the spinning region was displaced down stream, for the larger ratios however, the reversed flow pattern was almost broken up into large scale turbulence. It may be concluded that the near wake flow pattern and especially the position of the spinning region is not solely determined by the shearlayers as is the case when the spine is not present. Hence, interfering with the shearlayers by bleed will not show as marked an effect on the flow pattern as when the spine is absent as is indicated below. When the bleed rate is increased we may expect as for the cases without the spine that the meeting point of the shearlayers on the centreline shifts downstream tending to displace the spinning region. This displacement of the region where the vortices are being formed, tends to reduce sharply the effect of the spine on the vortex formation process due to the sensitivity mention-

ed before. These two opposing tendencies account for the reduced overall effectiveness of bleed as was shown in Fig. 21 and Fig. 22. The more confused results shown in Fig. 22 being due to the highly turbulent character of the reversed flow and the reattachment and wall-jet effects discussed before. It can be observed (Fig. 22) that the larger cylinders tend to show an increased drag reduction with bleed at higher bleed rates. In those cases the bleed velocity is close to the free stream velocity at separation. The wall-jet effect discussed before turns out to be present as may be deduced from Fig. 59.

The reattachment as observed for the chamfered cases without the spine for diameters greater than $\phi_b = .500''$ is not present until $\phi_b = .540''$ when the spine is introduced. Again, the reattachment is destroyed by very small amounts of bleed and the inversion in the drag (see Fig. 22) followed by the wall jet effect is found as may be seen in Fig. 59. For this spine geometry the jet stays attached until 50° from the separation points at the highest bleed rate. The rate of reduction in drag with bleed when the wall jet appears is almost equal to the one observed for cases without the spine (Fig. 20). Similar effects occur for the largest base cylinder diameter ($\phi_b = .550''$) but the wall jet is formed immediately after the reattachment is destroyed. However, the jet stays attached up to approximately 25° for the lowest bleed rate at which it can be detected moving to approximately 40° for the highest bleed rate used. It is thought that even higher bleed rates may result in significantly longer attachment distances for the wall jet, than those observed at the very small bleed rates.

3.4. Concluding Summary of Factors Affecting the Near Wake Structure and its Relation to the Base Pressure.

For a body geometry such that flow separation occurs at fixed symmetrical points the shape of the body inside the region of separation produces very distinct changes in the flow pattern. The effects of the base geometry are to change the conditions at the separation points, along the shearlayers springing from the separation points and also to interfere with the vortex formation process in the spinning region. The resulting changes of the characteristic lengths in the near wake and the base pressure distributions can be qualitatively related.

Base bleed was generally found to delay the meeting of the shearlayers springing from the separation points by reducing the rate of spread of these layers. The effect on the entrainment length was found to be approximately linear in the bleed coefficient C_{μ} and also to be somewhat affected by the pressure at separation and the size of the bleed slot.

Reattachment was found to take place for some of the chamfered models tested when a sufficiently small slot size was used and no or small bleed was present. Injection of very small amounts of bleed fluid upset this reattachment resulting in very rapid changes in drag. When for the above models the velocity of the bleed jet approached that of the main stream a wall jet was formed which stayed attached for up to 50° measured from the separation points along the base cylinders used.

It is apparent that the structure of the shearlayers before they meet was considerably altered by applying all the different conditions outlined above and also that the distance to the meeting points changed widely.

It was found that, within the limited accuracy of the measurements and independently of changes in the shearlayer development, the length of the non-dimensional spinning region l_{spin}/h was solely dependent on the non-dimensional entrainment length le/h ; the former decreasing when the latter increases. It is thought that the spinning length is directly connected with the strength of vortices in a regular vortex street, the strength being reduced with decreasing spinning length and being dependent on the entrainment length only.

4. General Conclusions and Recommendations

The variations of drag with bleed $|\Delta C_d/\Delta C_\mu|$ found for the models tested by Bearman and Woods (Ref. 4 and 3) had values of approximately 3.0 which was considered to be too low to be practical for use in the wind tunnel speed control system. Therefore the present investigation was aimed at seeking more efficient bleed modes by changing the base and bleed slot geometry. For a model with parallel thick trailing edges (blunt edged models) used in the present investigations the drag gain G_d , was found to increase when a circular cylinder was placed in the base cavity at the trailing edge. At a cylinder diameter of 1/8" (0.194 of base height) the gain was $G_d=3.0$ while a maximum value of $G_d=6.5$ was found for a diameter of .550" (0.854 of base height). This represents an improvement of 120% over the result found in References 3 and 4.

After the trailing edges of the above model were chamfered a similar result was obtained up to a cylinder diameter of $\phi_b=.530$ " (0.934

of base height). For larger diameters the drag gain was found to rise very sharply reaching a value of $G_d=74$ for $\phi_b=.550$ " (0.969 of base height). Although for the application to the speed stabilization system the very high drag gain looks attractive at first glance, it may turn out to result in a rather sensitive or even unstable control system. It is thought, however, that the present investigation yields adequate insight to arrive at a configuration with some intermediate drag gain such as to match the response requirements of the final control system.

The general information on blunt body flows gathered in the present work is not only useful for application to fluidic control systems, the results can be directly applied to the reduction of drag of blunt based airfoils in connection with the renewed interest in blunt based bodies for transonic and supersonic speeds. In that respect the geometries investigated look more promising than the ones used in References 3 and 4.

For relatively small bleed rates ($C_\mu \approx 0.04$) significantly lower drags are obtained than thought possible with the use of high bleed rates ($C_\mu \approx 0.15$) and/or splitter plates as used by Bearman and Woods. This is found to be due to the effects of attached wall jets when a large enough a base cylinder is installed at the rear of the models and a spine is used. The configurations with the base cylinder only, and also the ones with the spine attached to the cylinders are thought to be very easily adaptable to create lift by means of blowing unequal amounts of fluid from the two bleed slots.

Of direct practical use are configurations for which the base is made concave instead of being a solid flat plate. Such a base, using a semi-circle with radius roughly equal to half the base height was found to give a 20% reduction in drag as compared with a solid flat base.

Due to geometry changes and the use of bleed, a wide variation in the drag coefficient was found; the maximum was $C_d = .640$ the lowest $C_d = .270$. All the drag changes could be related to changes in the flow patterns in the near wake region through the use of a newly developed streamer method. This visualization method revealed that the symmetrical near wake flow patterns generally showed an isolated, violently fluctuating region approximately rectangular in shape - the spinning region which was separated from the body by a relatively quietly fluctuating reversed flow region - the entrainment region. The boundaries of this entrainment region were almost straight lines connecting the separation points with the forward "corners" of the rectangular spinning region. Downstream of the spinning region a relatively quietly fluctuating wake extended far downstream.

A uniformly valid correlation between the length of the spinning region (the spinning length) and the length of the entrainment region (the entrainment length) was found. The entrainment length can be used as a measure for the meeting point and the length of the shearlayers. The spinning region length is thought to be a measure of the strength of discrete vortices which, after being formed due to the shearlayer instability, enter a regular vortex street.

Drag changes were usually associated with detectable changes in the entrainment length but no uniformly valid correlation could be found. The relation between base drag and the entrainment length depended rather strongly on the shape of the base configuration. Although mostly qualitatively, the resulting trends could be related to the effects of the phenomena occurring.

The most significant drag changes due to bleed and/or geometry were found to obtain when the interference with the near wake flow was almost exclusively with the shearlayers and / or the forming vortices in the spinning region. Changes in geometry generally change the inclination of the shearlayer with respect to the axis without significantly changing the rate of spread or affecting the spinning region displacement. Bleed injection was shown to reduce the rate of spread of the shearlayers over a considerable length delaying the meeting point and thus the start of instability downstream.

Reattachment was found to occur for small slot heights and a sharpened trailing edge. In those cases large pressure changes and thus drag changes could be obtained with very small bleed rates. This reattachment was destroyed by the injection of larger amounts of bleed fluid which then gradually resulted in a wall-jet effect which became more significant as the bleed rates steadily increased within the injection limits investigated.

The above shows that the geometries investigated may be used as a vehicle to perform more extensive research into the fundamental aspects of flow mechanisms connected with: turbulent free shearlayers, reattachments,

turbulent wall-jets in adverse pressure gradients, separation and the formation of vortex streets at high Reynolds numbers. It is thought that the application of all these phenomena will become increasingly important if their behaviour can be better predicted. In particular, it is the author's opinion that "controlled separation" is not sufficiently used in connection with airfoil design and internal flows as in: air conditioning, air breathing engines and heat exchangers. Application of fluidic techniques to those fields are thought to have been much too conservative.

APPENDIX A

A Fluidic Windtunnel Speed Stabilization System

The accuracy of model measurements in closed circuit subsonic wind tunnels is directly affected by the time wise drift of the nominal air speed in the test section. This is caused by the proportionality of forces and pressures to the square of the airspeed and also by the extreme sensitivity of the behaviour of certain phenomena at critical conditions to small speed variations.

Excluding the effects of high frequency variations due to the turbulence level, the causes of low frequency speed variations are:

- unsteady drive unit
- speed drift due to heating of the air and/or the drive unit
- changed loading on the tunnel due to varying model incidence, jaw or pitch.

The speed control around any set point is usually manual; the air speed is monitored and corrected by manually changing the setting on the drive unit. Because of the large inertias of the rotating parts and the circulating air such a control mode necessarily results in a relatively slow response. Also, skill is required to maintain a constant speed within narrow limits.

Automatic control is possible by means of electro-mechanical, fluidic-mechanical or purely fluidic systems. A fluidic system would use air to interfere with the tunnel speed and therefore eliminate the large inertias of the drive unit and other mechanical components. Such a system would be attractive because of possible short response times and the depend-

ability due to the absence of moving parts. For these reasons a fluidic system is being investigated.

The causes of the tunnel speed drift may be considered to be a disturbance resistance superimposed upon a basic tunnel resistance. The function of a fluidic control system would be to sense the speed and counteract variations from the nominal setting by means of a variable control resistance, in the tunnel circuit thus keeping the tunnel speed constant. Such a system has been proposed by Dr. J. Tinkler of the mechanical engineering department and is depicted in Fig. A1.

The operation would be as follows. A fluidic speed sensor placed at a convenient location in the tunnel is connected to a fluidic comparator which detects any change with respect to a set speed and gives a pressure output as a function of the speed error. The output causes a proportional variation of the control resistance such as to maintain a constant tunnel speed. However, the flow rate output of the comparator is small so that a fluidic power-amplifier is needed to produce relatively large flow input to the variable resistance.

The complete static no-load performance of the speed sensor incorporating the comparator was investigated in Ref. 1. Its principle of operation is that of a fluidic beam amplifier and is based on the fluidic anemometer developed in Ref. 19. Two total head tubes at some distance apart are symmetrically placed in the fully developed part of a high velocity jet issuing from a supply nozzle. When the arrangement is placed perpendicular to a low velocity cross flow the jet is deflected in the down-

A3.

stream direction. The total head tubes - one placed downstream of the other - experience different stagnation pressures due to the deflection of the jet, the difference being a measure for the cross flow velocity. The pressure difference has good linearity for velocities up to 10ft/sec. and a high pressure gain $|\Delta\text{pressure}/ \Delta\text{velocity}|$. The linear range can be moved to a higher velocity (up to 40ft/sec.) by tilting the supply nozzle axis against the cross flow keeping the total head tubes fixed. The inclination of the supply nozzle can be set such as to find a zero stagnation pressure difference at any cross flow velocity up to 40ft/sec. This capability serves as the comparator function needed for the control system. Due to the velocity range a convenient location for the speed sensor would be in the tunnel settling chamber. The airspeed in the test section is directly proportional to the settling chamber air speed.

The high pressure gain at zero flow through the total head tubes (receiver nozzles) is anticipated to drop when the speed sensor is connected to the amplifier so that air flows from the sensor into the amplifier. Several stages of amplification may therefore be used such that first the small pressure difference occurring in the speed sensor is sufficiently amplified to be able to control the flow amplifier needed to drive the variable resistances. Both the pressure and the flow amplifier are under investigation. A high pressure source is to be used for the speed sensor and the pressure amplifier. In order not to change the air mass circulating in the tunnel, the supply for the flow amplifier is to be taken from the settling chamber. However, this coupling makes it necessary to maintain a constant flow rate in the flow amplifier to avoid undesirable feed-back effects.

To be able to vary the control resistances with this constant mass flow, two separate devices are to be used, one which increases its resistance to the tunnel with flow rate through it and the other lowering its resistance with flow rate. By dividing the total available flow rate through the amplifier between these two resistances as a function of the input from the comparator, the resulting change in resistance to the tunnel flow is additive.

The proposed variable resistance may be achieved by means of:

- (1) variation of the drag of blunt based bodies by means of base bleed,
- (2) control of the efficiency of the diffuser section in the tunnel circuit by induced local separation through blowing.

General characteristics of base bleed investigated in the present thesis shows that the drag decreases with bleed rate. It is anticipated that the resistance to flow of the diffuser section of the wind tunnel will increase with increasing amount of blowing. Together these yield the desired additive effect. Convenient locations for the two control resistances are indicated in Fig. A1. They are so far from the test section that local high turbulence levels as might be caused by the control resistances will be sufficiently dissipated before reaching the test section and only the average speed will be affected.

The fluidic system will show the feasibility of such a system for stabilizing low frequency variations in the tunnel speed. More generally, however, it will show if the present trend to miniaturization of fluidic systems is the only road to a more competitive position of fluidic systems compared to electronic systems.

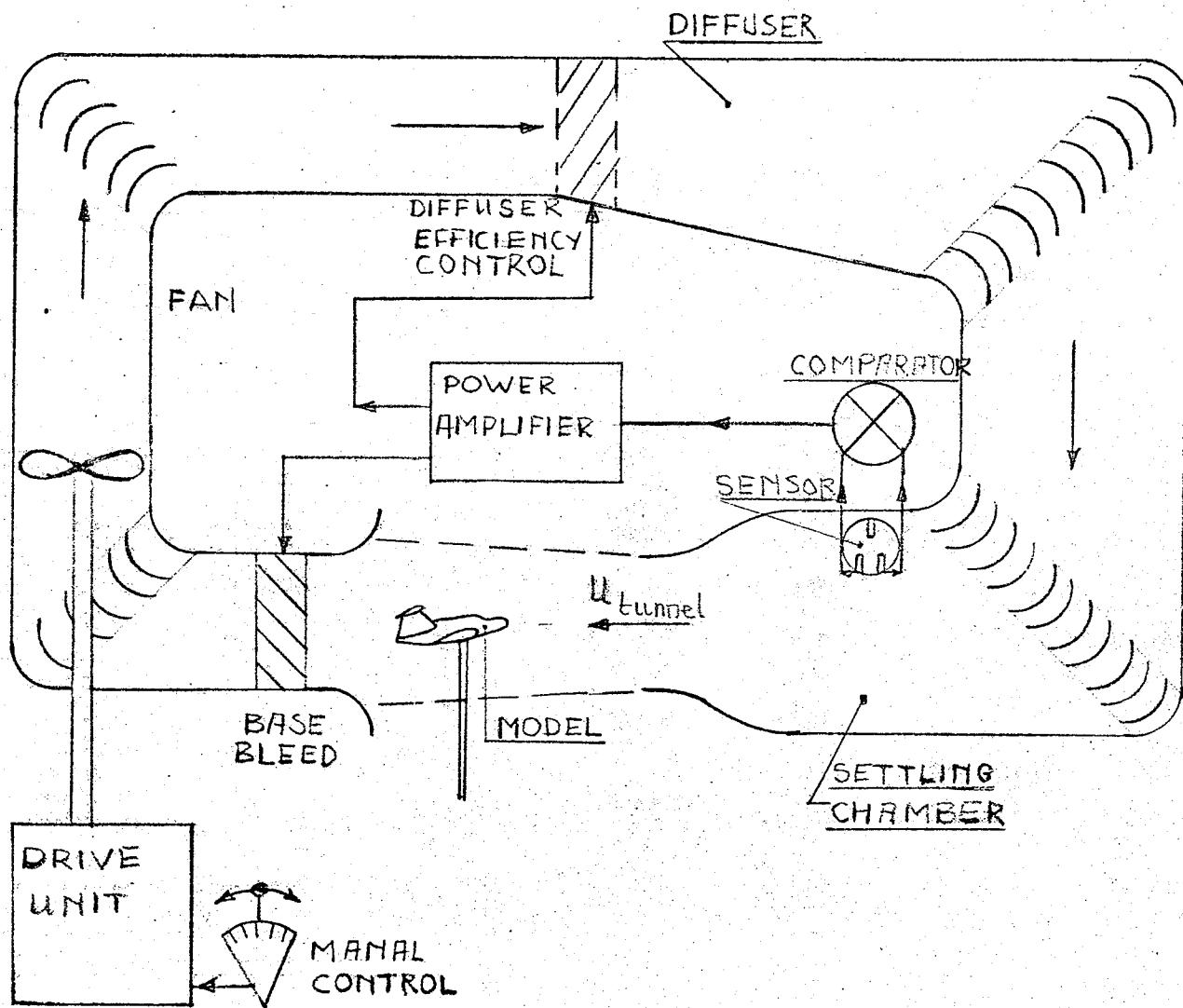


FIG. A1 FLUIDIC WINDTUNNEL STABILIZATION SYSTEM.

-78-

APPENDIX B

Turbulent Free Shearlayers

Consider the two-dimensional incompressible mixing of two plane parallel stream at the same temperature but at different velocities U_1 and U_2 . Mixing starts at a point $(x=0, y=0)$ as depicted in Fig. B1. The mixing region spreads going downstream and a velocity profile as indicated is found.

As for wall boundary layers it may be assumed that the pressure across the layer is uniform. Also, for the case of parallel mixing between two semi-infinite velocity fields the pressure may be assumed to be independent of x and the usual boundary layer approximations may be applied.

Laminar free shearlayers are found to be unstable and break up into turbulent layers even for very small disturbances. Therefore, the only practical case to consider is the turbulent free shearlayer.

For all theoretical work on turbulent boundary layers assumptions have to be made regarding the effective viscosity (eddy viscosity) to replace the viscosity as applicable to laminar flow appearing in the Navier-Stokes equation. For free turbulent flow Prandtl's eddy viscosity hypothesis is used which states:

$$\epsilon = \chi b (U_1 - U_2) \quad (B1)$$

where:

ϵ = eddy-or effective turbulent viscosity

χ = experimental constant

b = width of the mixing zone

U_1, U_2 = velocities at the boundary of the shearlayer.

The boundaries are defined similar to the usual boundary layer thickness definition. Due to the velocities outside the layers to be constant it is easy to show (See Ref. 6,12,20) that the velocity profiles at different x positions in the shearlayer should be similar and that the rate at which the mixing region growth downstream is constant or

$$\frac{db}{dx} = \text{constant.} \quad (\text{B2})$$

The similarity variable is

$$\eta = y/x \quad (\text{B3})$$

and the velocity u in the layer is constant along rays through ($x=0$, $y=0$). The transverse perturbation velocity v can be found to be

$$v = u \frac{db}{dx}. \quad (\text{B4})$$

With the above assumptions and using the eddy viscosity the equation of motion governing the flow in the mixing region is (Ref. 6,12,20)

$$u \frac{\partial u}{\partial x} + v \frac{\partial u}{\partial y} = \epsilon \frac{\partial^2 u}{\partial y^2}. \quad (\text{B5})$$

Substitution for ϵ yields

$$u \frac{\partial u}{\partial x} + v \frac{\partial u}{\partial y} = \chi c x (U_1 - U_2) \frac{\partial^2 u}{\partial y^2}. \quad (\text{B6})$$

where:

$$b = cx \quad (\text{B7})$$

c = proportionality factor.

Because of the similarity the non-dimensional velocity in the shearlayer is of the form

$$\frac{U_1 - u}{U_1 - U_2} = f(\eta). \quad (\text{B8})$$

B3.

Since $\eta = y/x = \frac{cy}{y_1 - y_2} = \frac{cy}{b}$ (B9)

$$\frac{U_1 - u}{U_1 - U_2} = f\left(\frac{cy}{b}\right) \quad (\text{B10})$$

The boundary conditions on equation (B6) are:

$$u = U_1 \text{ at } \eta = +\infty \quad (\text{B11}^a)$$

$$u = U_2 \text{ at } \eta = -\infty \quad (\text{B11}^b)$$

and also due to von Kármán, that the net transverse force on the shear-layer should be zero or

$$U_1 v_1 + U_2 v_2 = 0. \quad (\text{B11}^c)$$

The equation (B6) subject to the boundary condition (B11^{a,b,c}) may now be solved in either of the following ways. Assume a closed form behaviour of $f(\eta)$ which satisfies (B11^{a,b,c}) and fits the velocity profile as is done by Abramovich (Ref. 12) or solve for $f(\eta)$ numerically as is demonstrated in Ref. 21.

Close approximation of experimental data is found by Ref. 12 using the simple relation

$$\frac{U_1 - u}{U_1 - U_2} = f(\eta) = (1 - \eta^{3/2})^2 \quad (\text{B12})$$

which is shown in Fig. B1.

The rate of spread $\left(\frac{db}{dx}\right)$ has to be determined from experiments for each velocity ratio

$$r = \frac{U_2}{U_1}. \quad (\text{B13})$$

B4.

An approximate relation between the rate of spread at a given velocity ratio ($r \neq 0$) to that at ($r=0$) is given by Ref. 12 and shown in Fig. B2 where is plotted

$$\frac{\left(\frac{db}{dx}\right)_r}{\left(\frac{db}{dx}\right)_{r=0}} = \frac{1-r}{1+r} \quad \text{for } r > 0, \quad (\text{B14})$$

and

$$\frac{\left(\frac{db}{dx}\right)_r}{\left(\frac{db}{dx}\right)_{r=0}} = 1 \quad \text{for } r < 0. \quad (\text{B15})$$

Experimental results have been included which, depending on the inherent turbulence level in the free stream, follow the approximate behaviour according to (B14). Recent results by Mills (Ref. 21) also follow the curve.

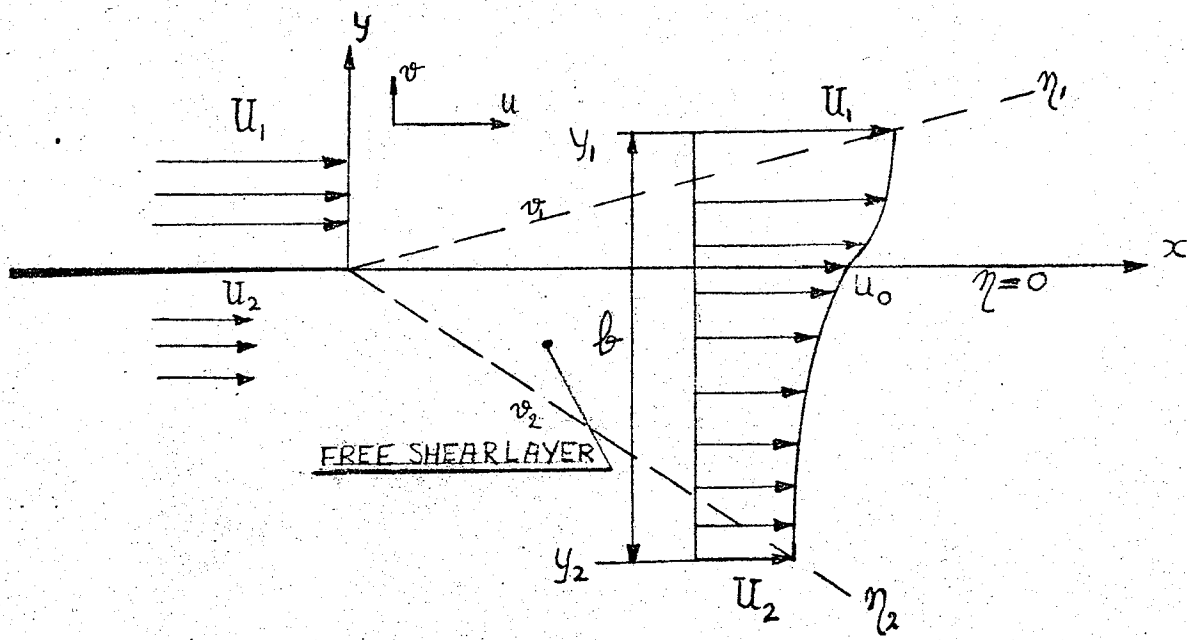


FIG. B1 TURBULENT FREE SHEAR LAYER.

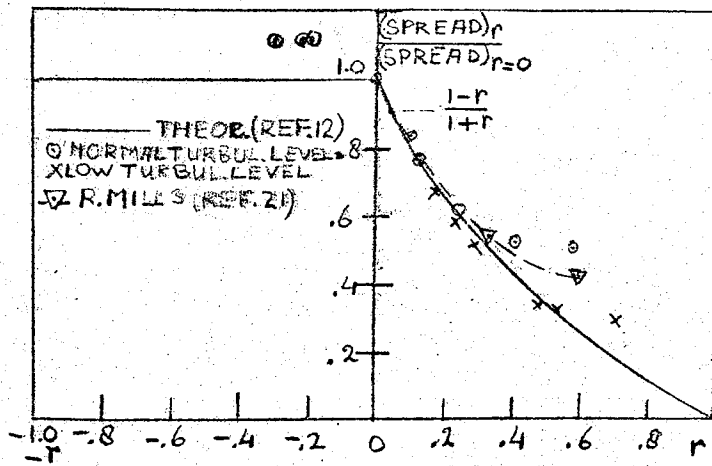


FIG. B2 THE RATE OF SPREAD OF TURBULENT FREE SHEAR LAYERS AS INFLUENCED BY THE VELOCITY RATIO.

REFERENCES

1. A. Pottin An Experimental Fluidic Anemometer. B.Sc. Thesis, Department of Mechanical Engineering University of Manitoba. (1969).
2. J. F. Nash A Review of Research on Two-Dimensional Base Flow. Rep. Mem. No. 3323 (1962).
3. C. J. Wood The Effect of Basebleed on a Periodic Wake. Journal of the R.Ae.S. (1964).
4. P. W. Bearman The Effect of Basebleed on the Flow Behind a Two-dimensional Model with a Blunt Trailing Edge. The Aeronautical Quarterly Vol. XVIII (1967).
5. L. Prandtl and O. G. Tietjens Applied Hydro-and Aeromechanics (1934).
6. S. Goldstein Modern Developments in Fluid-dynamics Chapter IX.
7. A. Roshko On the Drag and Shedding Frequency of Two-dimensional Bluff Bodies. N.A.C.A. Techn. Note 3169, (1955).
8. A. Fage and F. C. Johansen On the Flow of Air Behind an Inclined Flat Plate of Infinite Span. A.R.C. R&M No. 1104 (1927).
9. F. H. Abernathy and R. E. Kronauer The Formation of Vortex Streets. Journal of Fluid Mech. Vol. 13, Part I, (1962).
10. J. H. Gerrard The Mechanics of the Formation Region of Vortices Behind Bluff Bodies. Journal of Fluid Mech., Vol. 25, part 2, (1966).
11. C. J. Wood Visualization of an Incompressible Wake with Base Bleed. Journal of Fluid Mech., Vol. 29, part 2, (1967).
12. G. N. Abramovich The Theory of Turbulent Jets. Massachusetts Institute of Technology. (1963).

13. M. M. Zdravkovich Smoke Observations of the Formation of a von Kármán Vortex Street. Journal of Fluid Mech., Vol. 37, part 3, (1969).
14. P. Freymuth On Transition in a Separated Laminar Boundary Layer. Journal of Fluid Mech., Vol. 25, part 4, (1966).
15. A. Michalke and
 A. Timme On the Inviscid Instability of Certain Two-dimensional Vortex-type Flows. Journal of Fluid Mech., Vol. 29, part 4, (1967).
16. I. Tani Experimental Investigation of Flow Separation Over a Step. Utham Symposium, Freiburg, (1957).
17. S. F. Hoerner Fluid Dynamic Drag. Published by the author. (1958).
18. L. Leal and
 A. Acrivos The Effect of Basebleed on the Steady Separated Flow Past Bluff Objects. Journal of Fluid Mech., Vol. 39, part 4, (1969).
19. J. W. Tanney A Fluidic Anemometer for Low Velocities. N.A.E. Report LR-472, (1962).
20. S. Uchida and
 T. Suzuki On a Similar Solution for a Turbulent Half-jet Along a Curved Streamline. Journal of Fluid Mech., Vol. 33, part 2, (1968).
21. R. D. Mills Numerical and Experimental Investigations of the Shearlayer Between Two Parallel Streams. Journal of Fluid Mech., Vol. 33, part 3, (1968).
22. B. W. Wilton The Effect of Basebleed on Base Drag. B.Sc. Thesis, University of Manitoba (1969).

81.

FIGURES

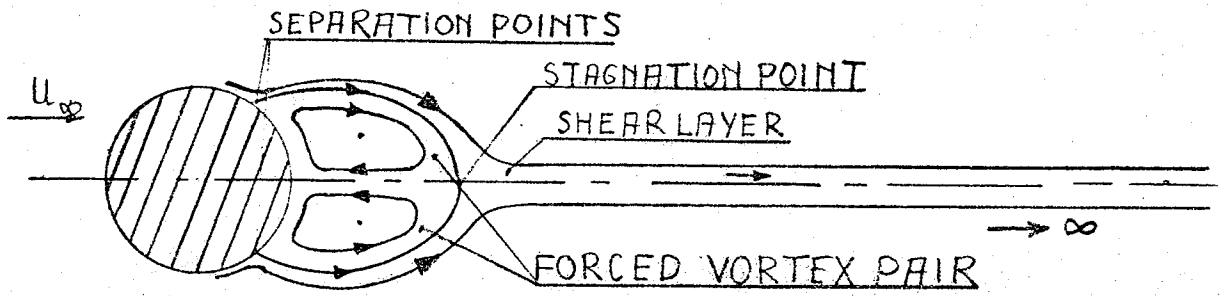


FIG. 1^A. $Re < 50$

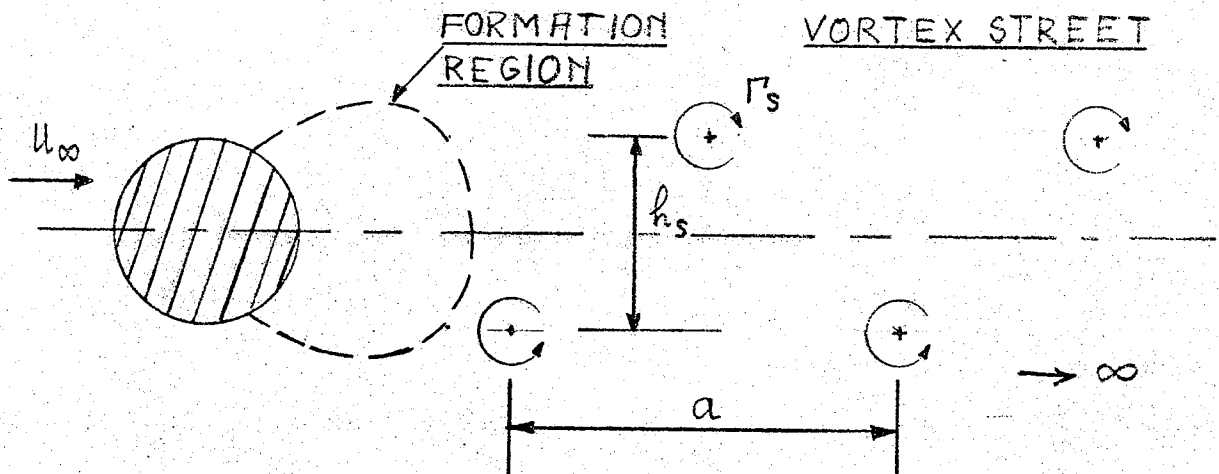


FIG. 1^B . $50 < Re < 10^5$

FIG. 1 FLOW PATTERN AROUND A CYLINDER

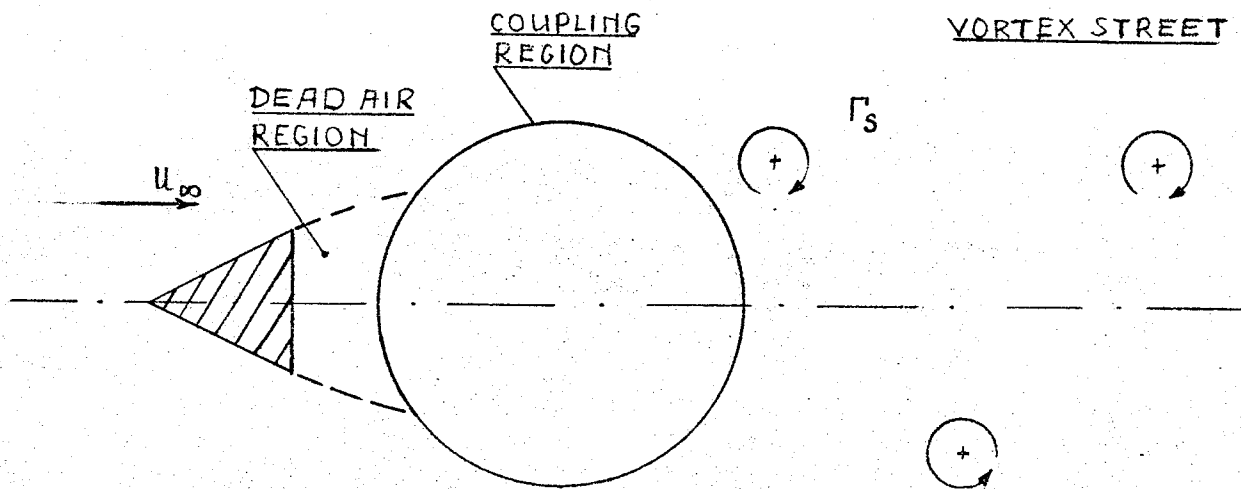


FIG.2 ROSHKO'S SUBSONIC BASE FLOW MODEL.

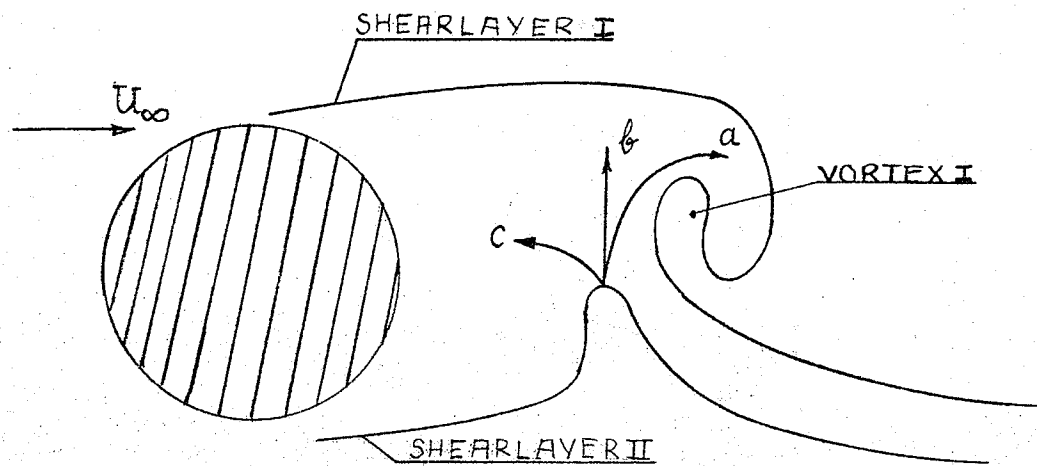


FIG.3 SCHEMATIC OF VORTEX FORMATION PROCESS ACCORDING TO GERRARD.

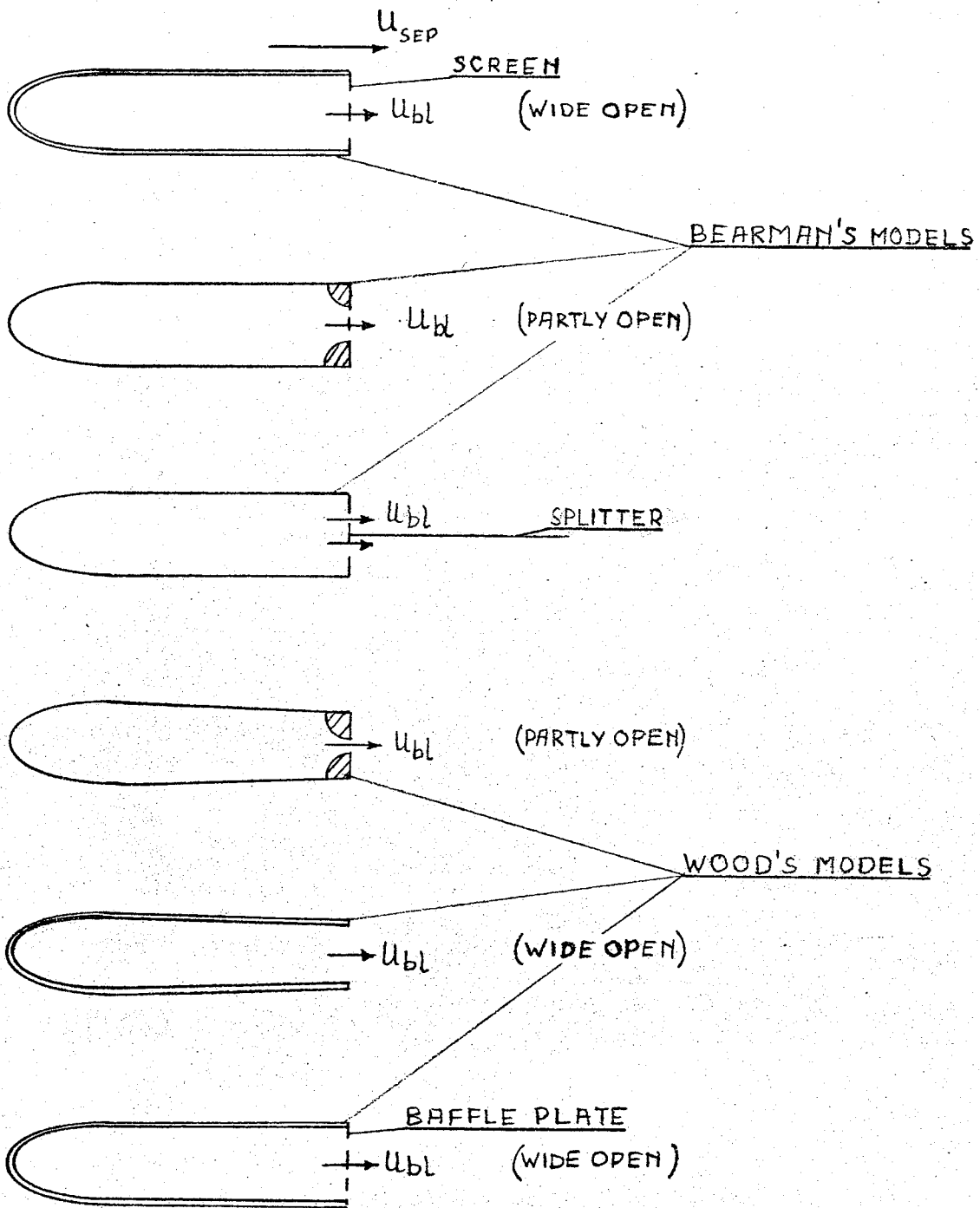


FIG.4 BEARMAN'S AND WOOD'S MODELS.

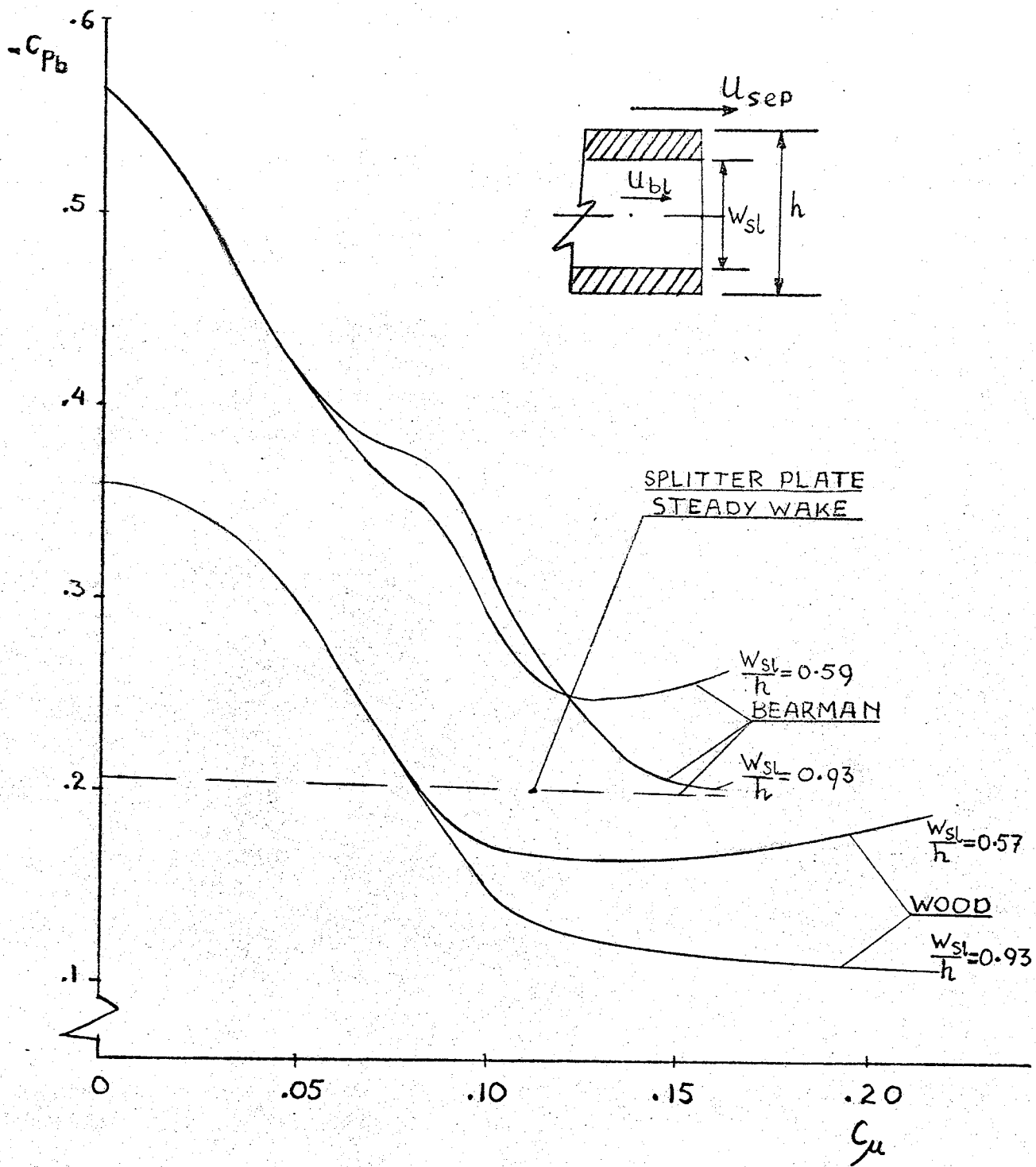


FIG.5^a COMPARISON OF BASE PRESSURE BEHAVIOUR

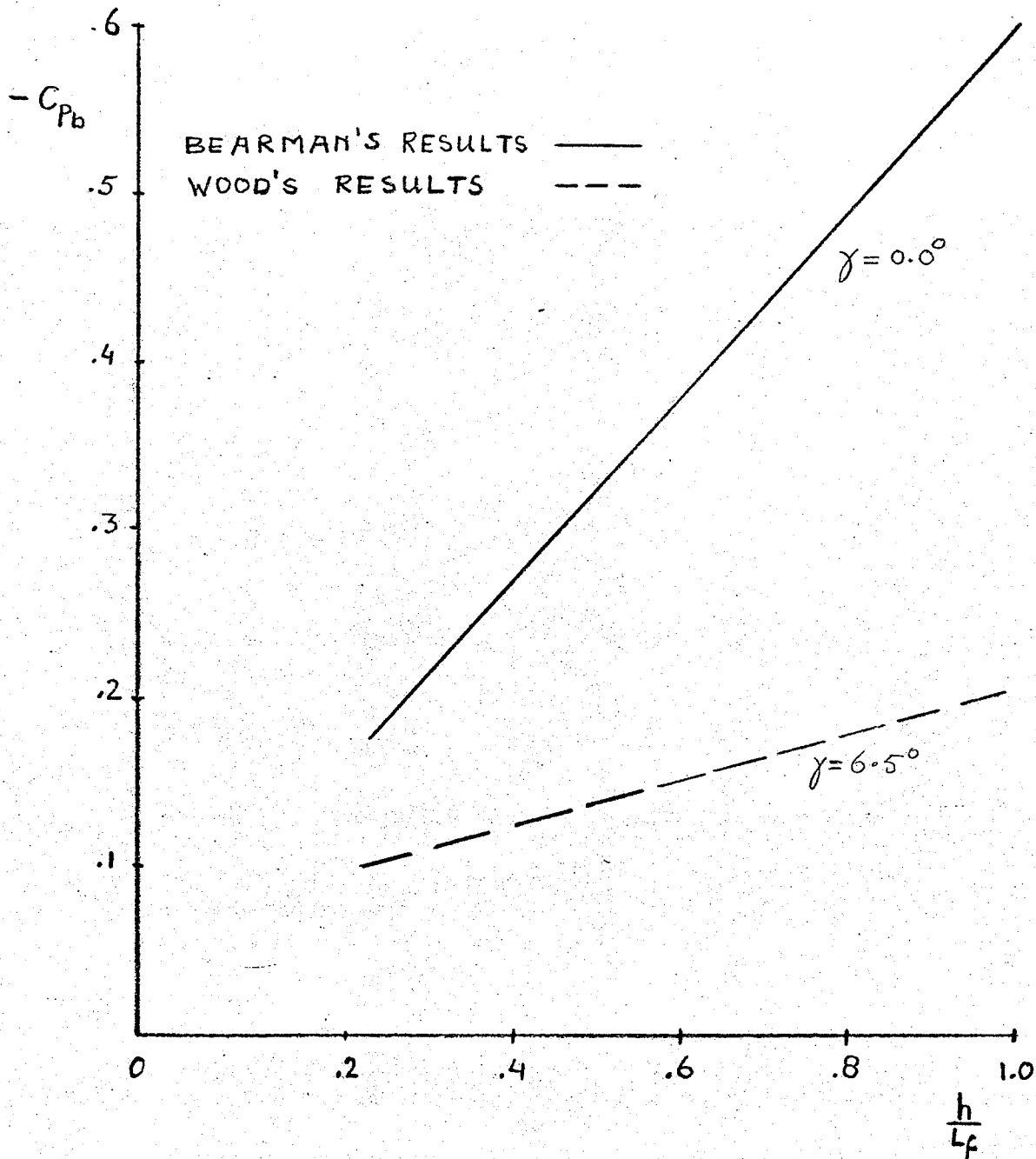
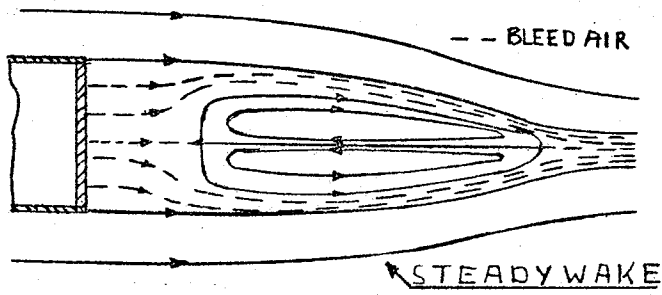
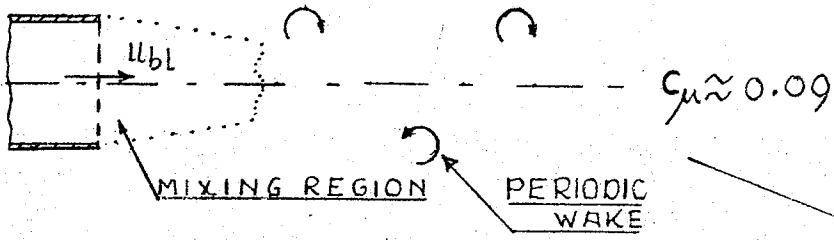


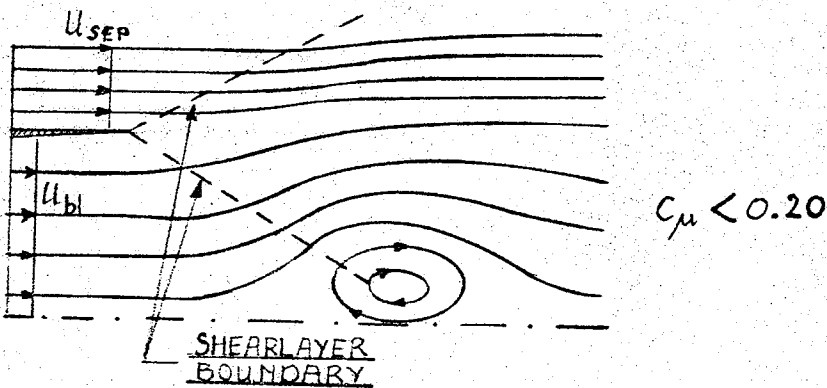
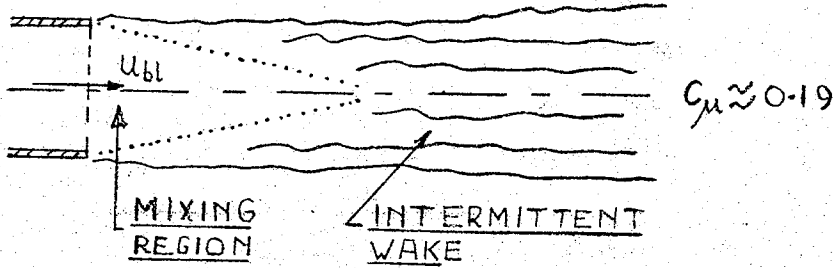
FIG.5^b CORRELATION OF BASE PRESSURE AND VORTEX FORMATION LENGTH.



BEARMAN



WOOD



ABRAMOVICH

FIG.6 SUGGESTED WAKE CONFIGURATIONS.

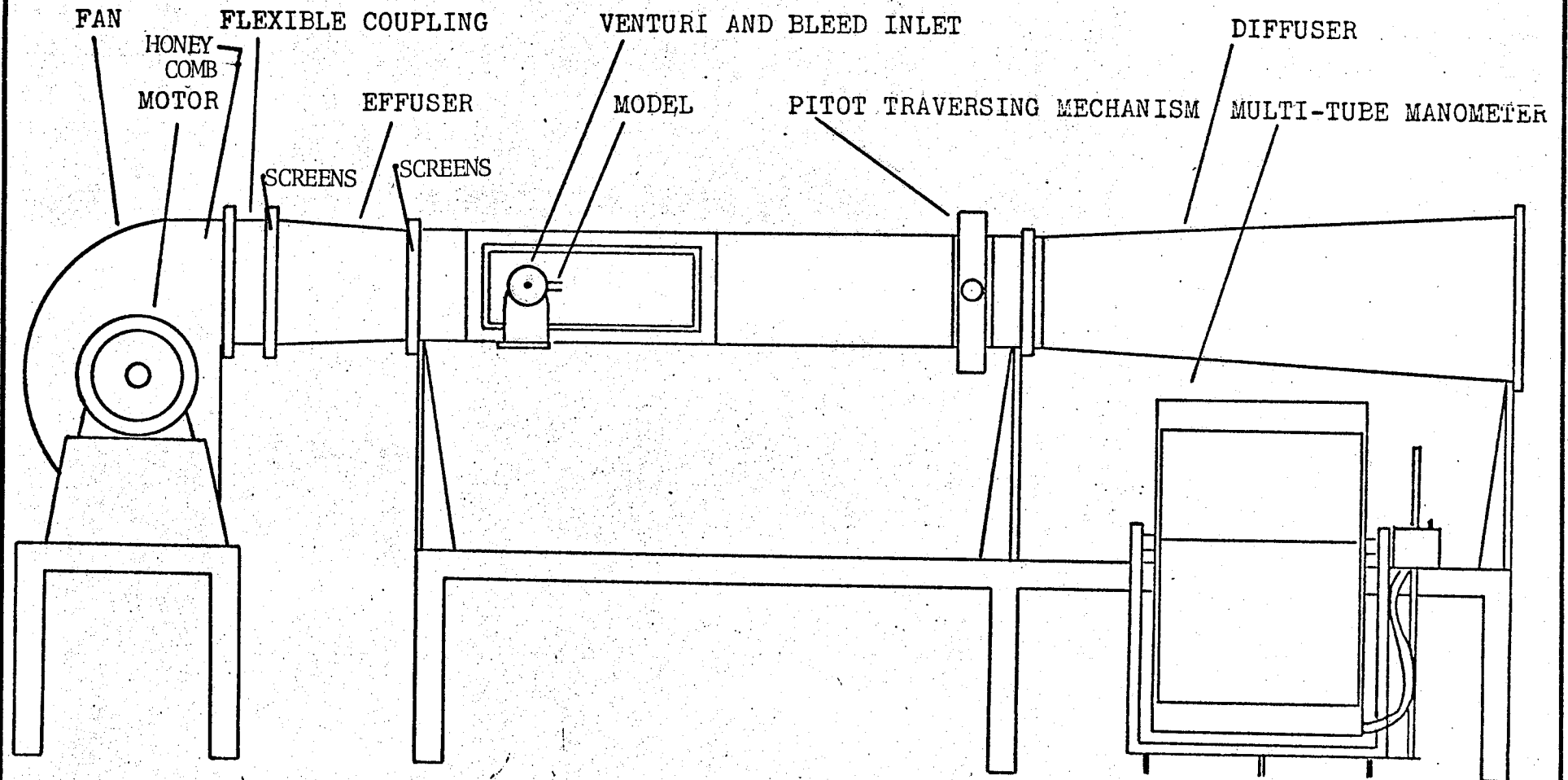


FIGURE 7 SCHEMATIC DIAGRAM OF APPARATUS

FIG. 7

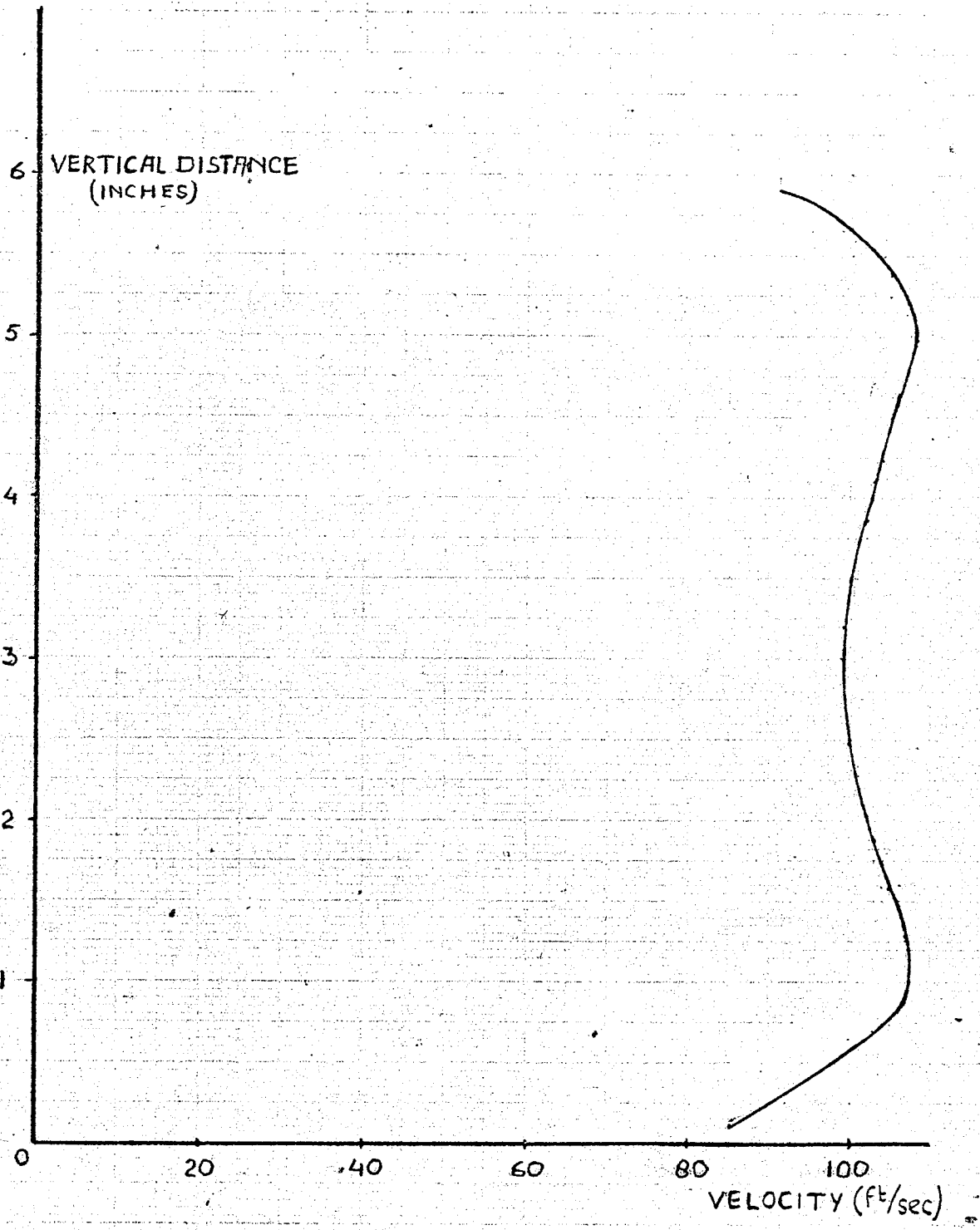


FIG. 8 VELOCITY DISTRIBUTION IN WINDTUNNEL.

FIGURE 9 CONTOUR PLOT OF FLOW AFTER STRAIGHTENING

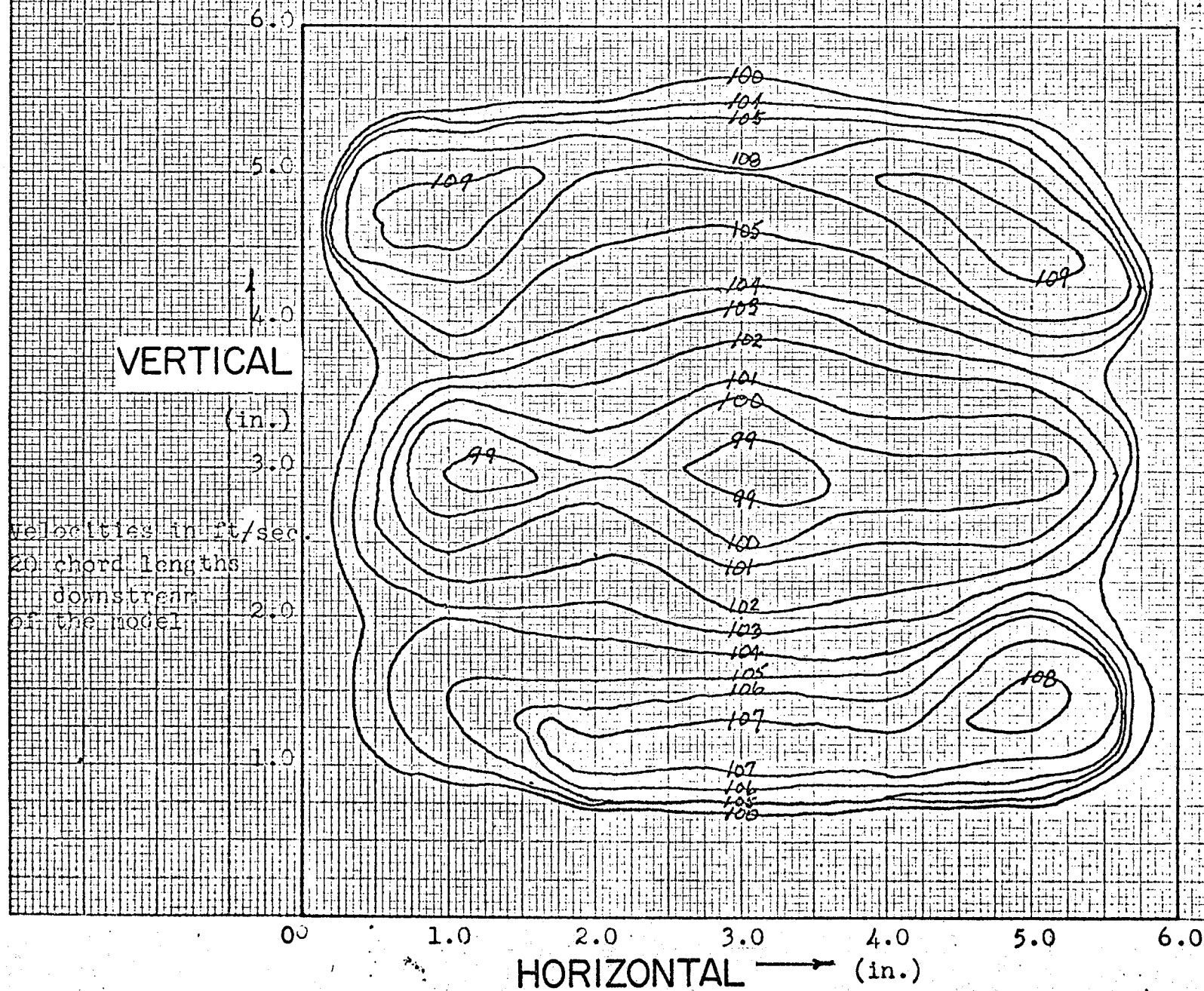


FIG. 9

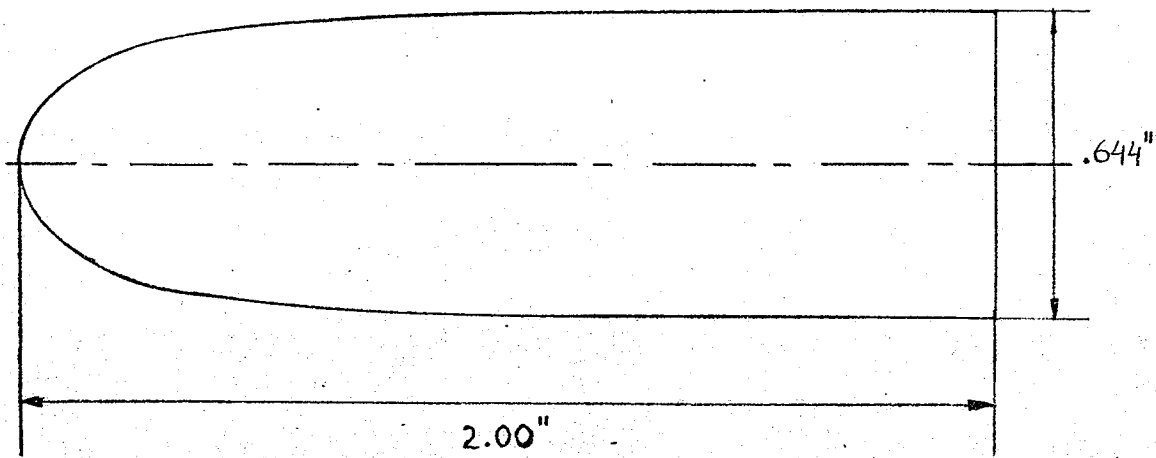


FIG.10^a PROFILE OF MODEL I

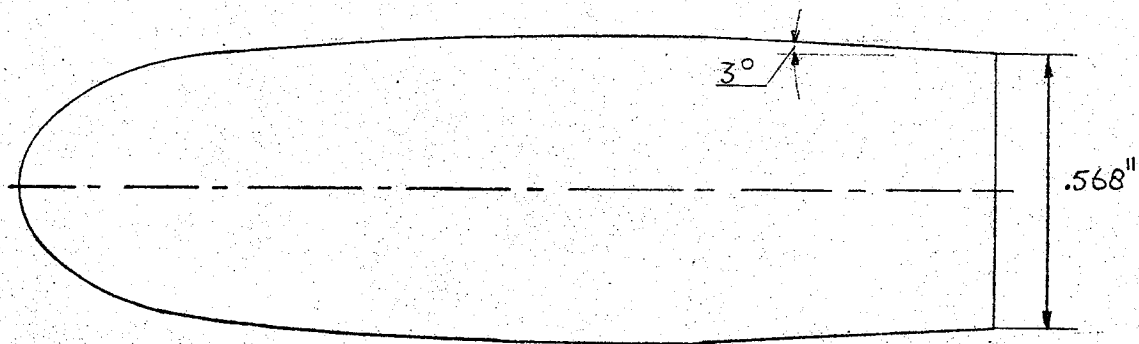


FIG.10^b PROFILE OF MODEL II

FIG.10 BASIC MODELS.

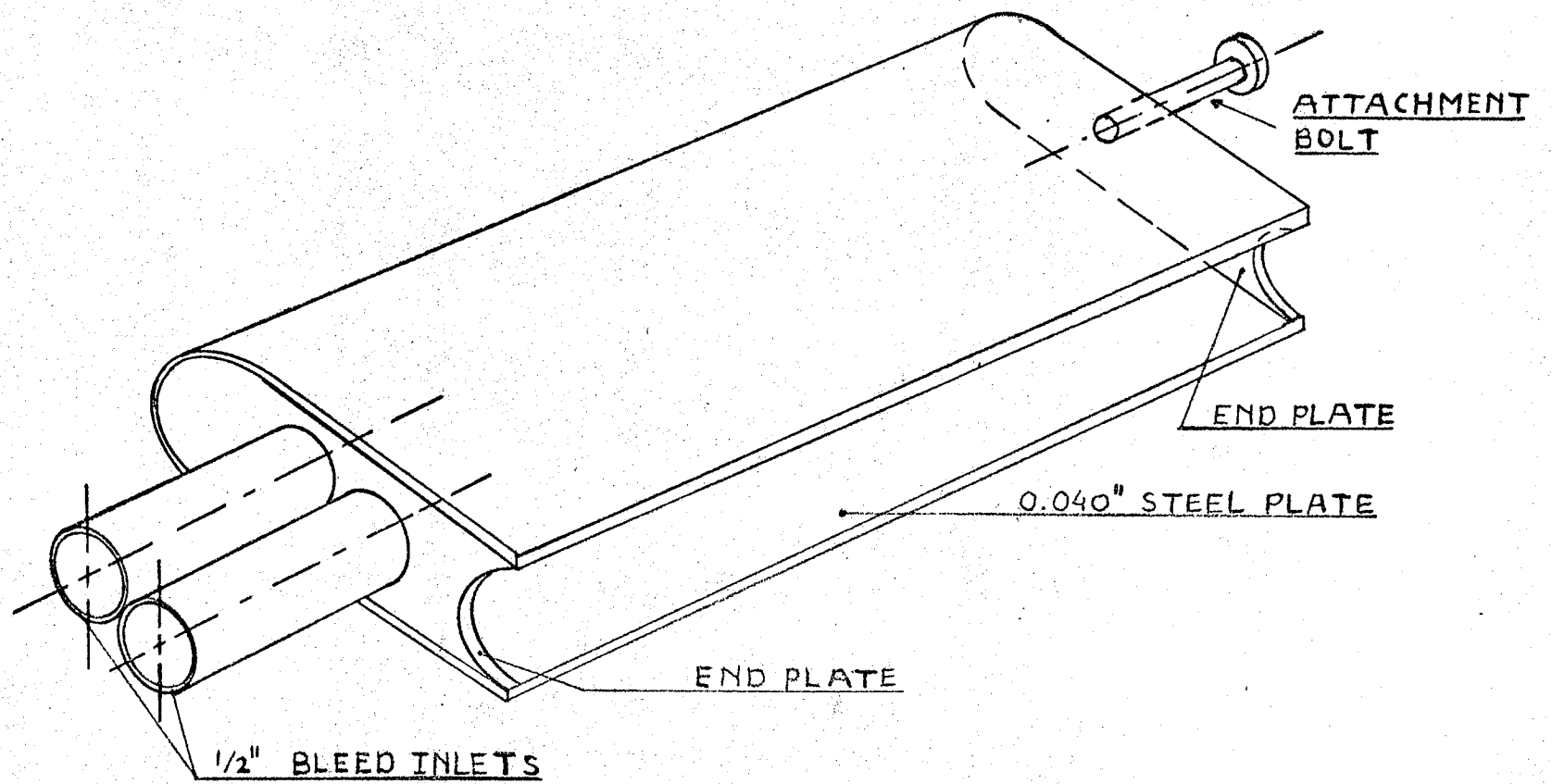


FIG. II MODEL I.

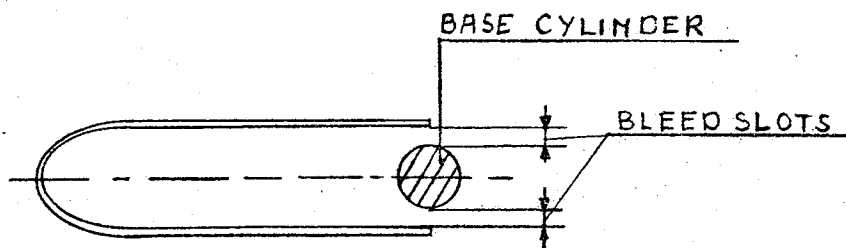


FIG. 12^a MODEL I WITH BASE CYLINDER

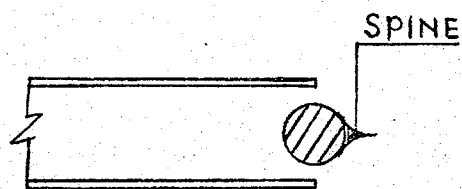


FIG. 12^b MODEL I WITH BASE CYLINDER AND SPINE

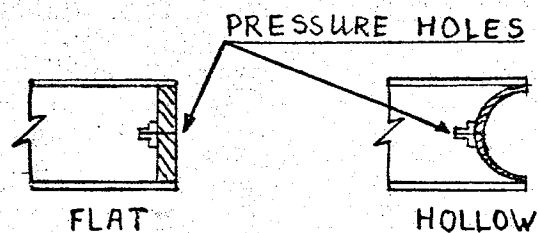


FIG. 12^c FLAT AND HOLLOW BASE CONFIGURATIONS

FIG. 12 BASE CONFIGURATIONS FOR MODEL I.

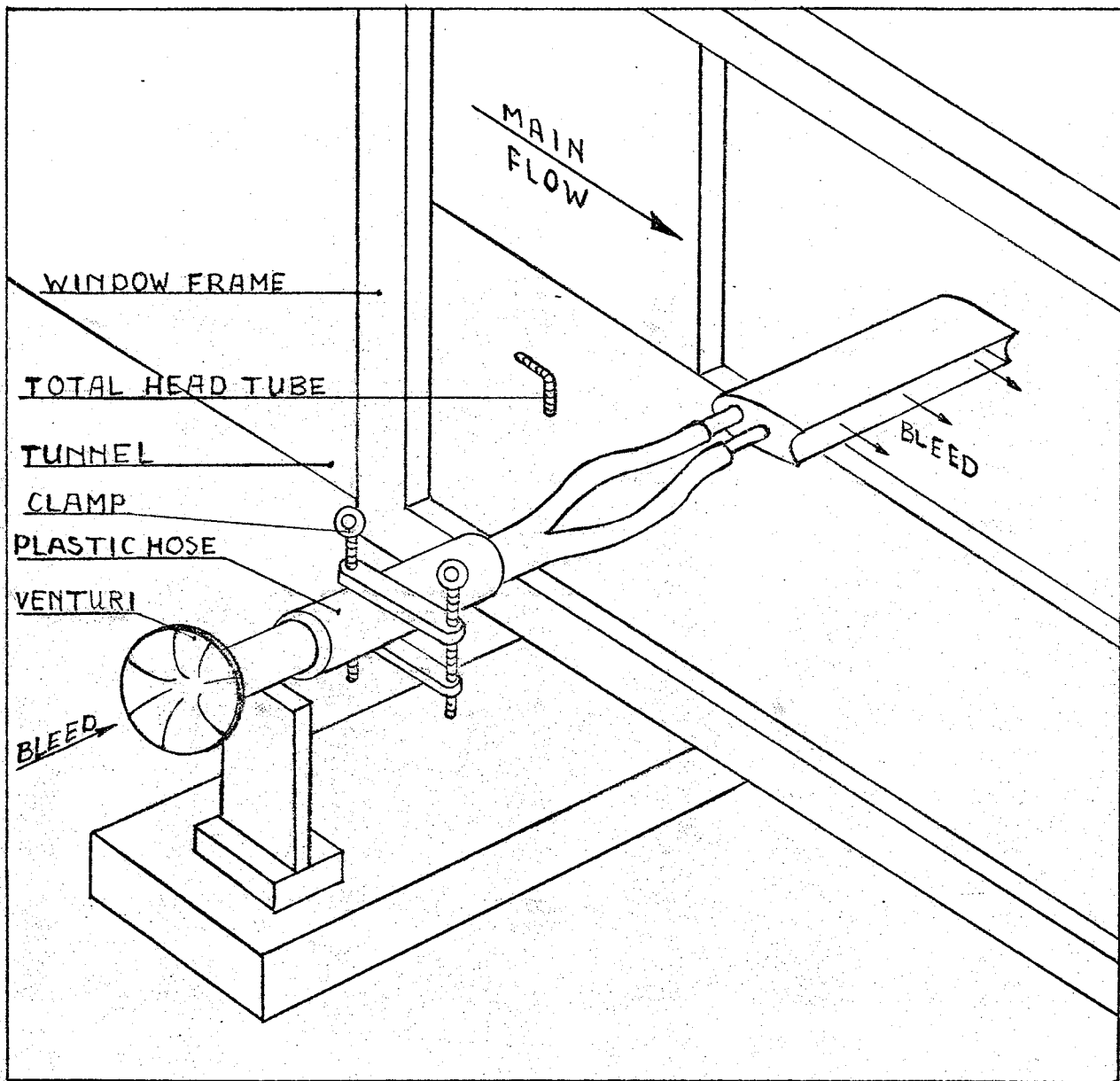


FIG.13 BLEED ARRANGEMENT.

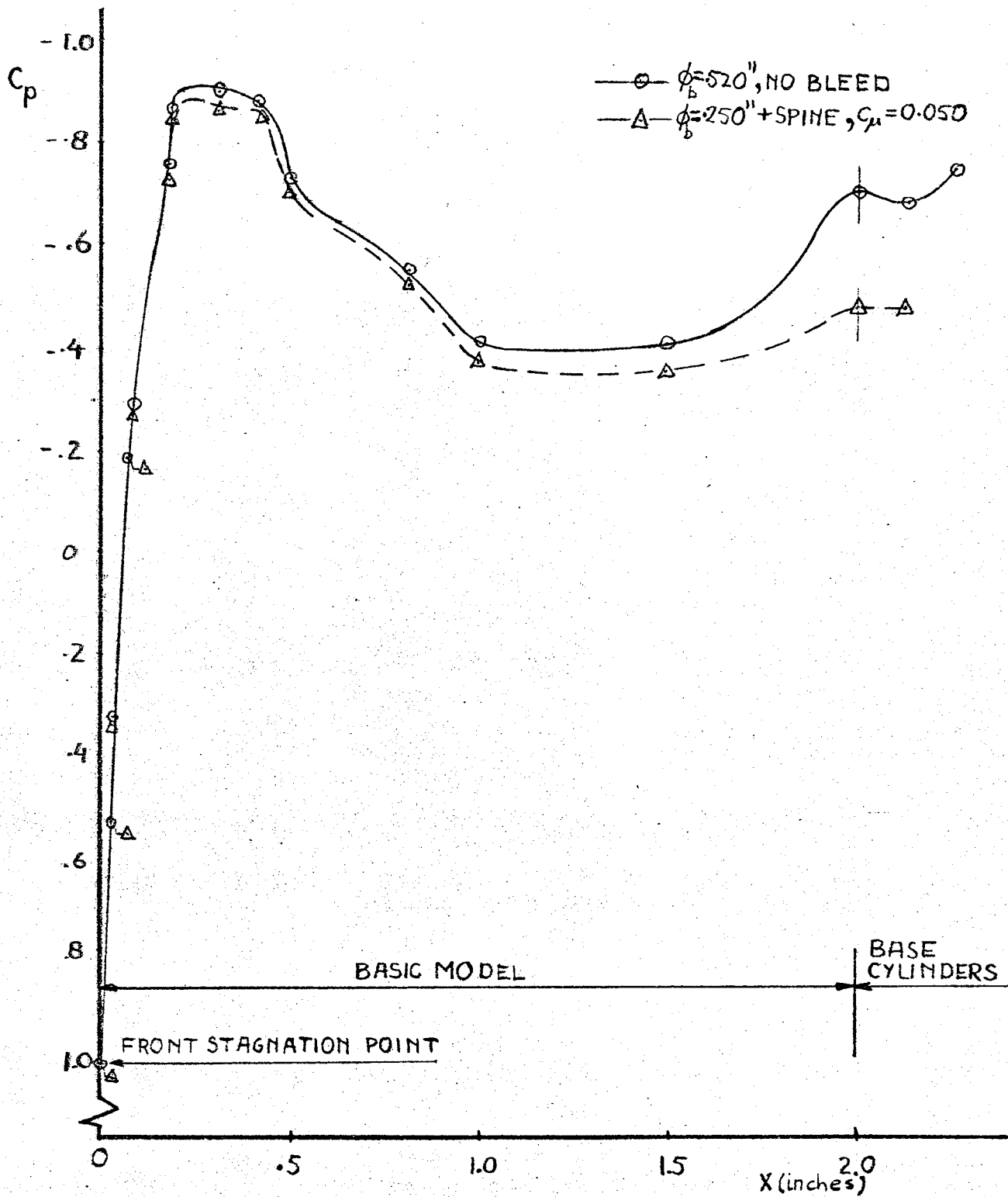


FIG.14^a PRESSURE DISTRIBUTIONS FOR MODEL I

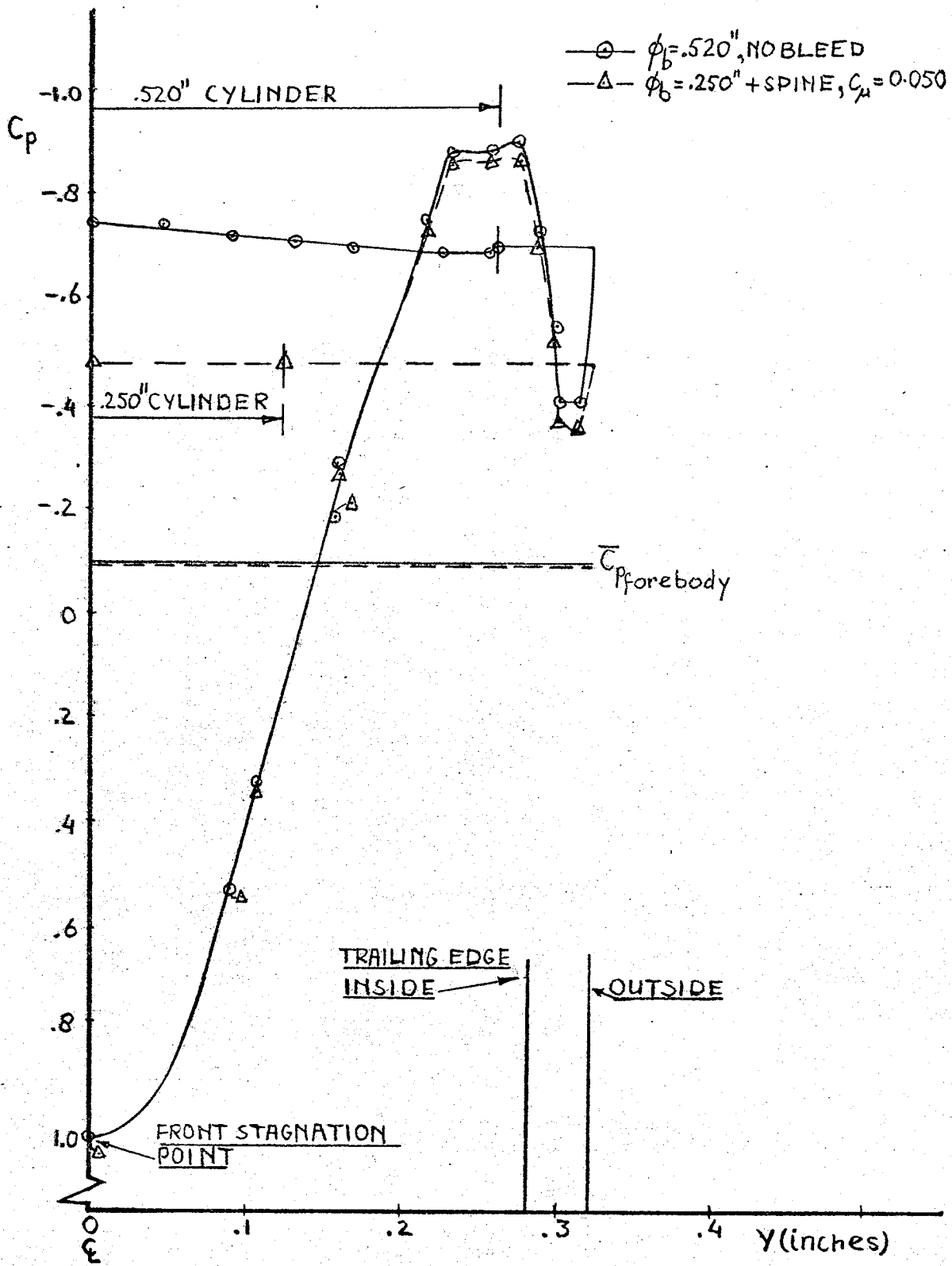


FIG.14^b PRESSURE DISTRIBUTIONS FOR MODEL I.

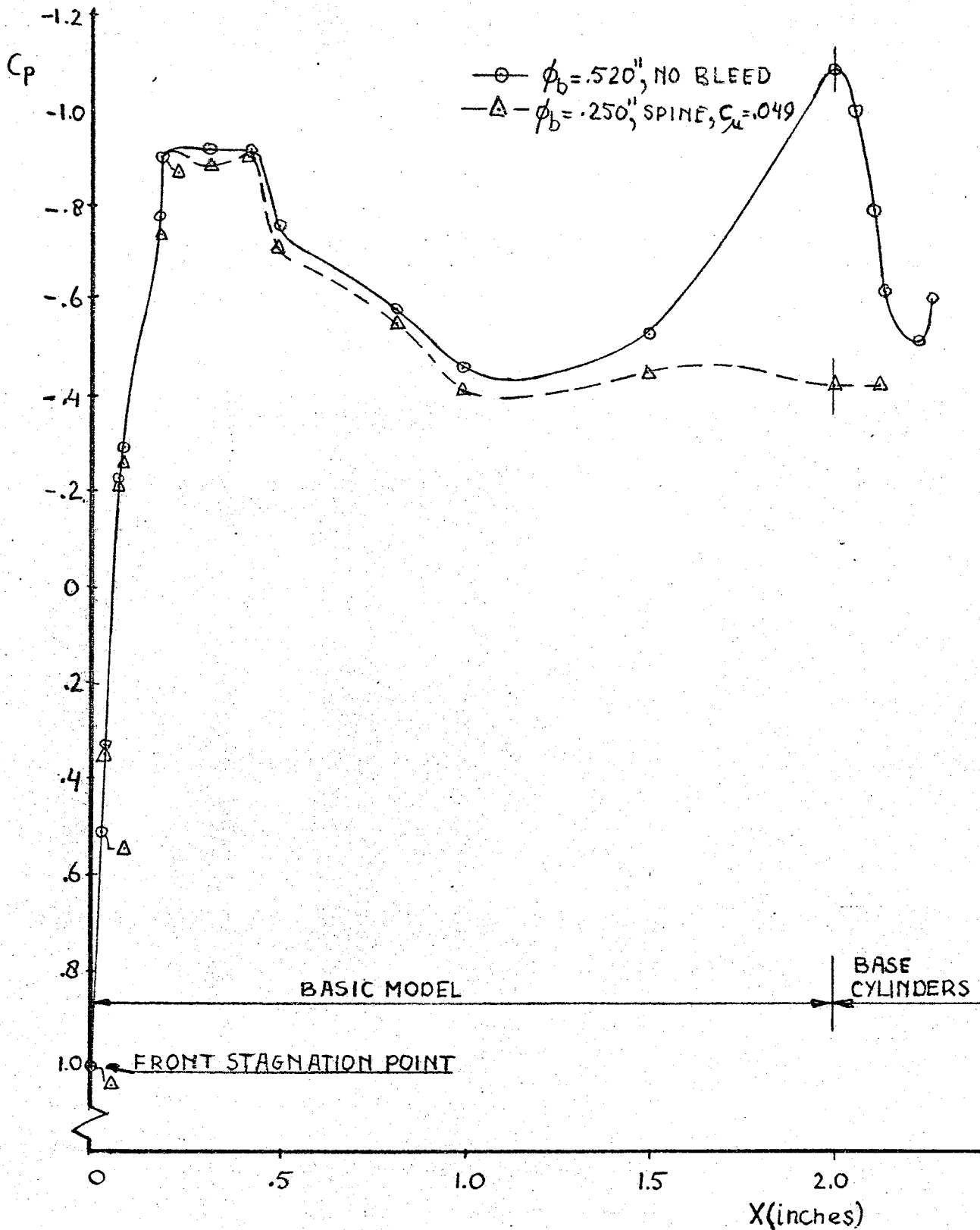


FIG.15^a PRESSURE DISTRIBUTIONS FOR MODEL II.

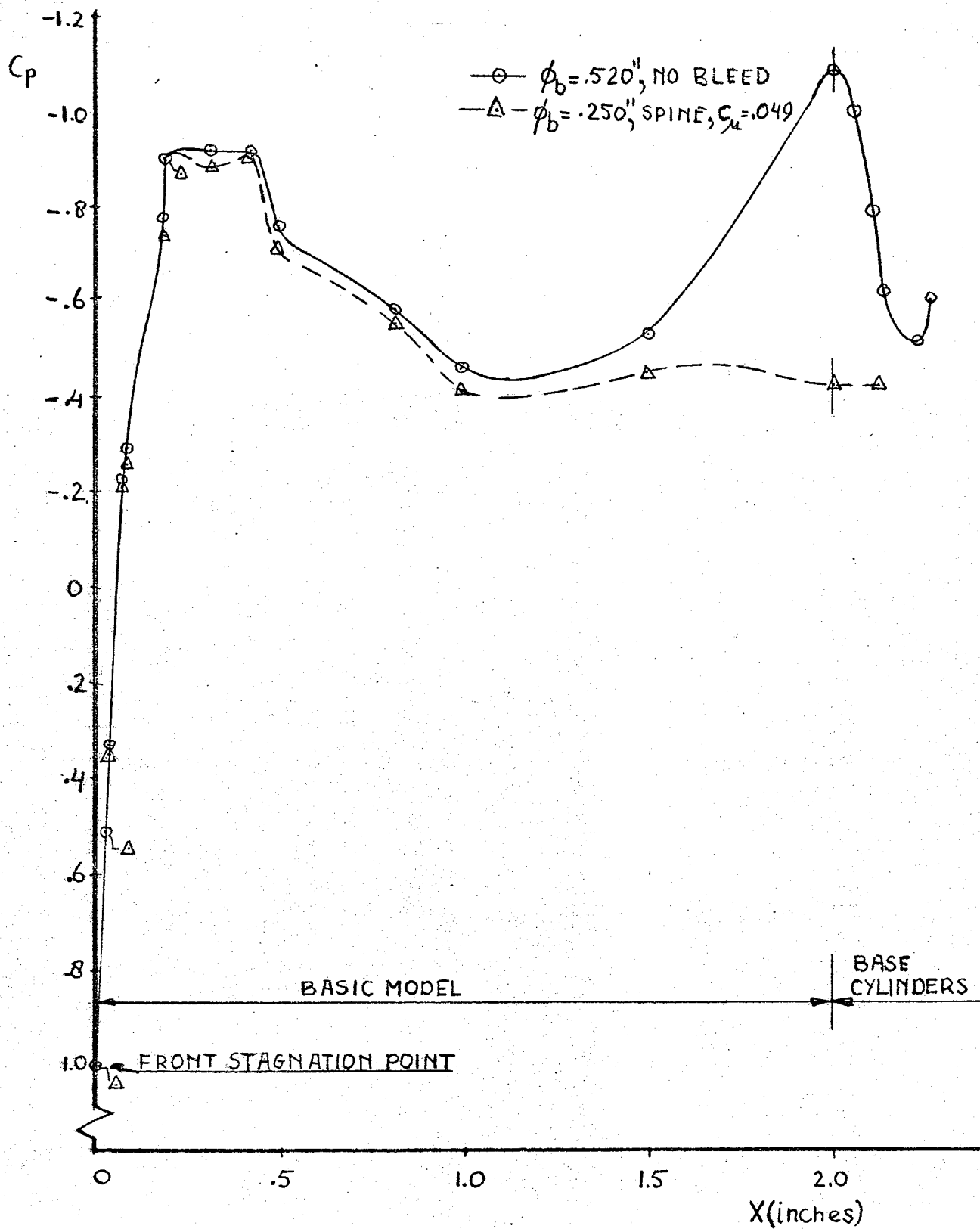


FIG. 15^a PRESSURE DISTRIBUTIONS FOR MODEL II.

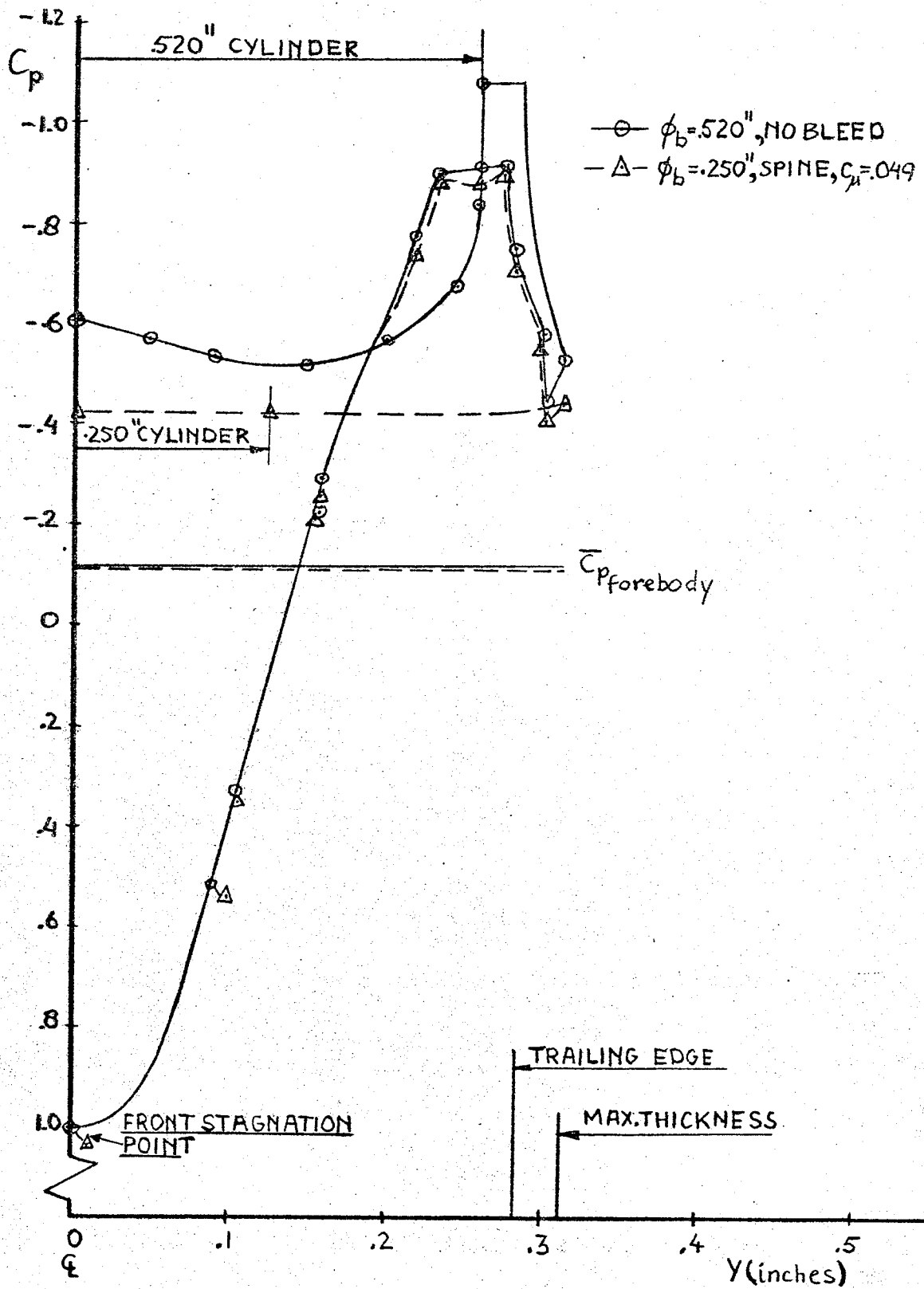


FIG. 15^b PRESSURE DISTRIBUTIONS FOR MODEL II.

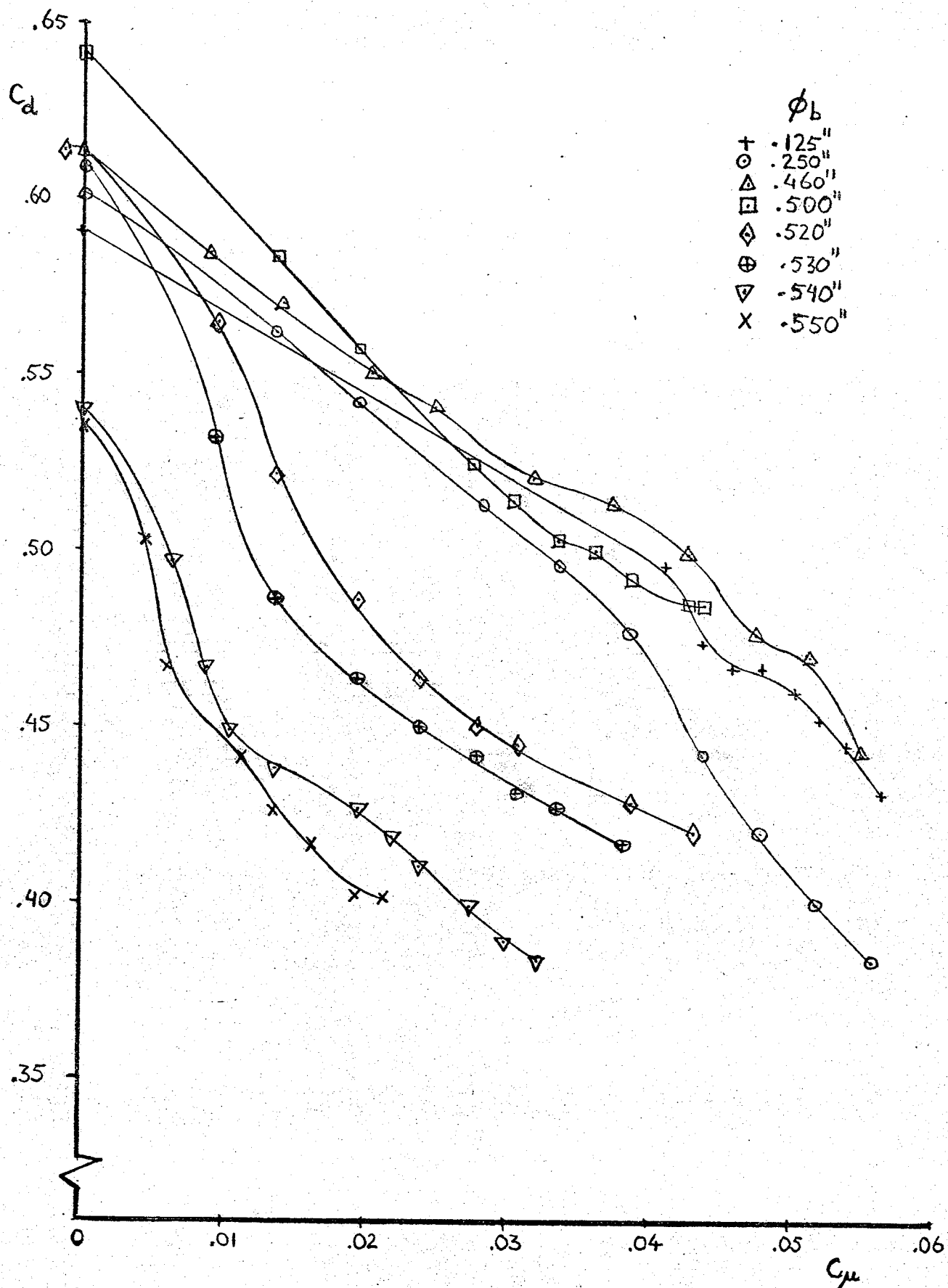


FIG.16 VARIATION OF DRAG WITH BLEED FOR MODEL I WITH BASE CYLINDERS,

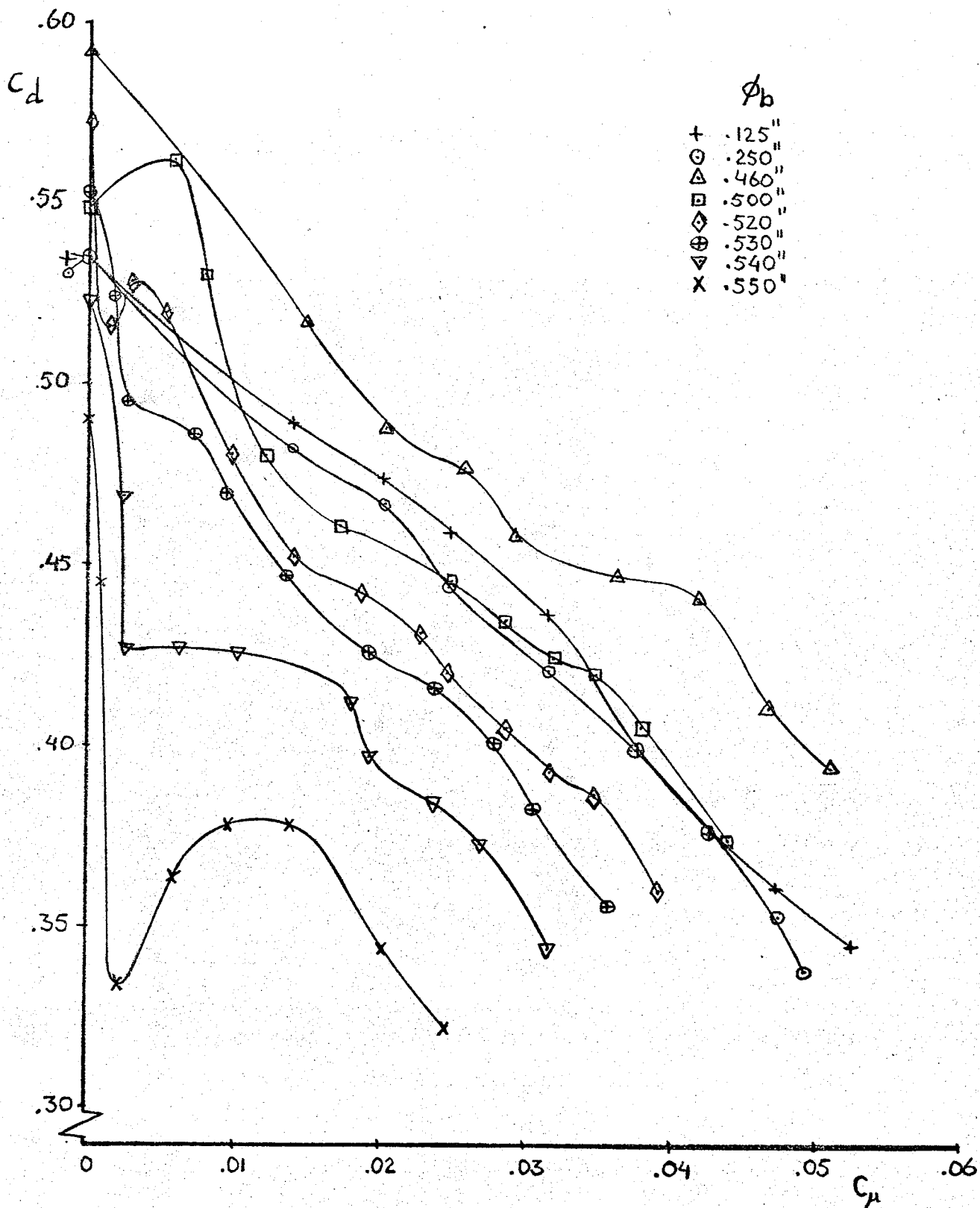


FIG.17 VARIATION OF DRAG WITH BLEED FOR MODEL II WITH BASE CYLINDERS.

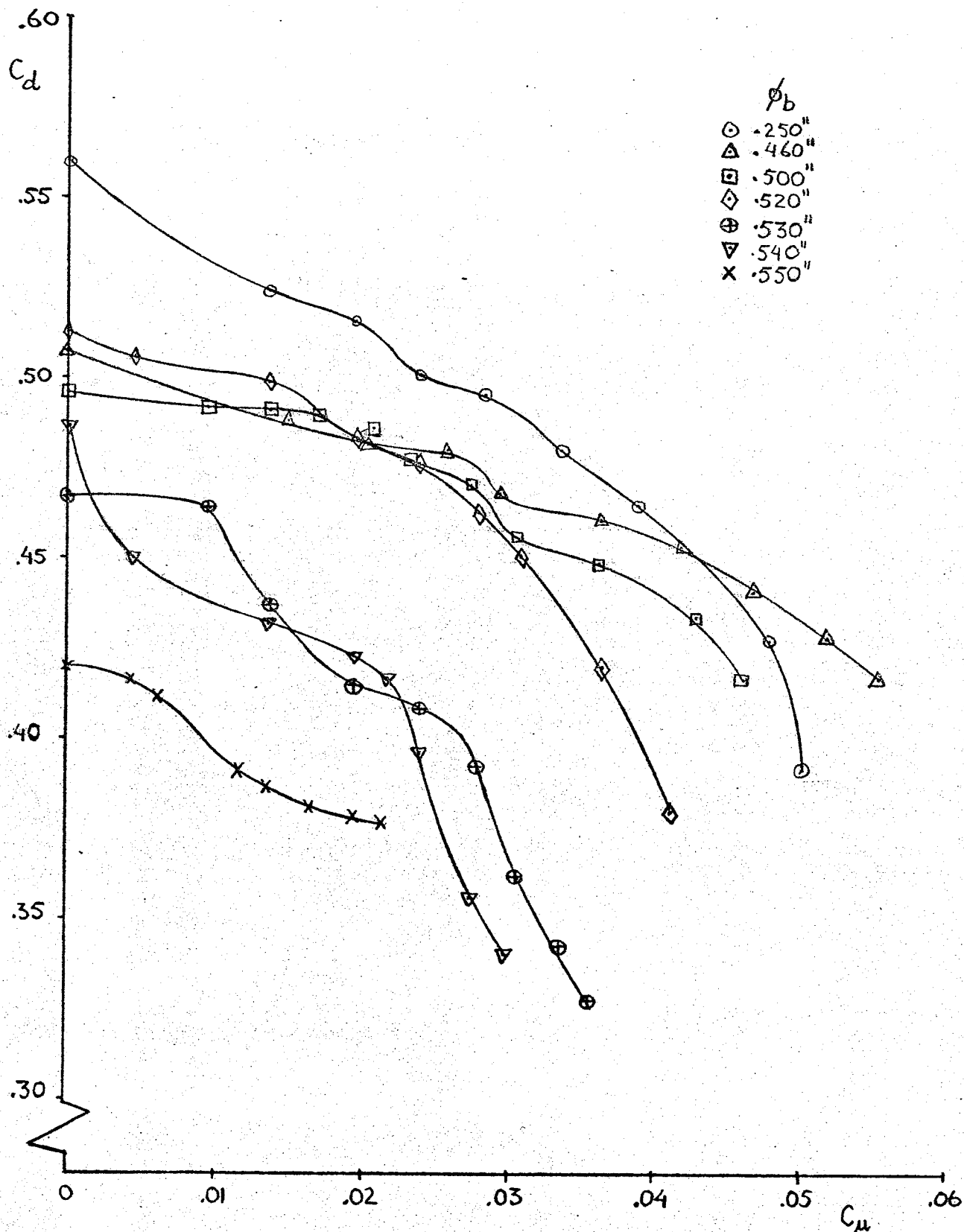


FIG.18 VARIATION OF DRAG WITH BLEED FOR MODEL I WITH BASE CYLINDERS AND SPINE.

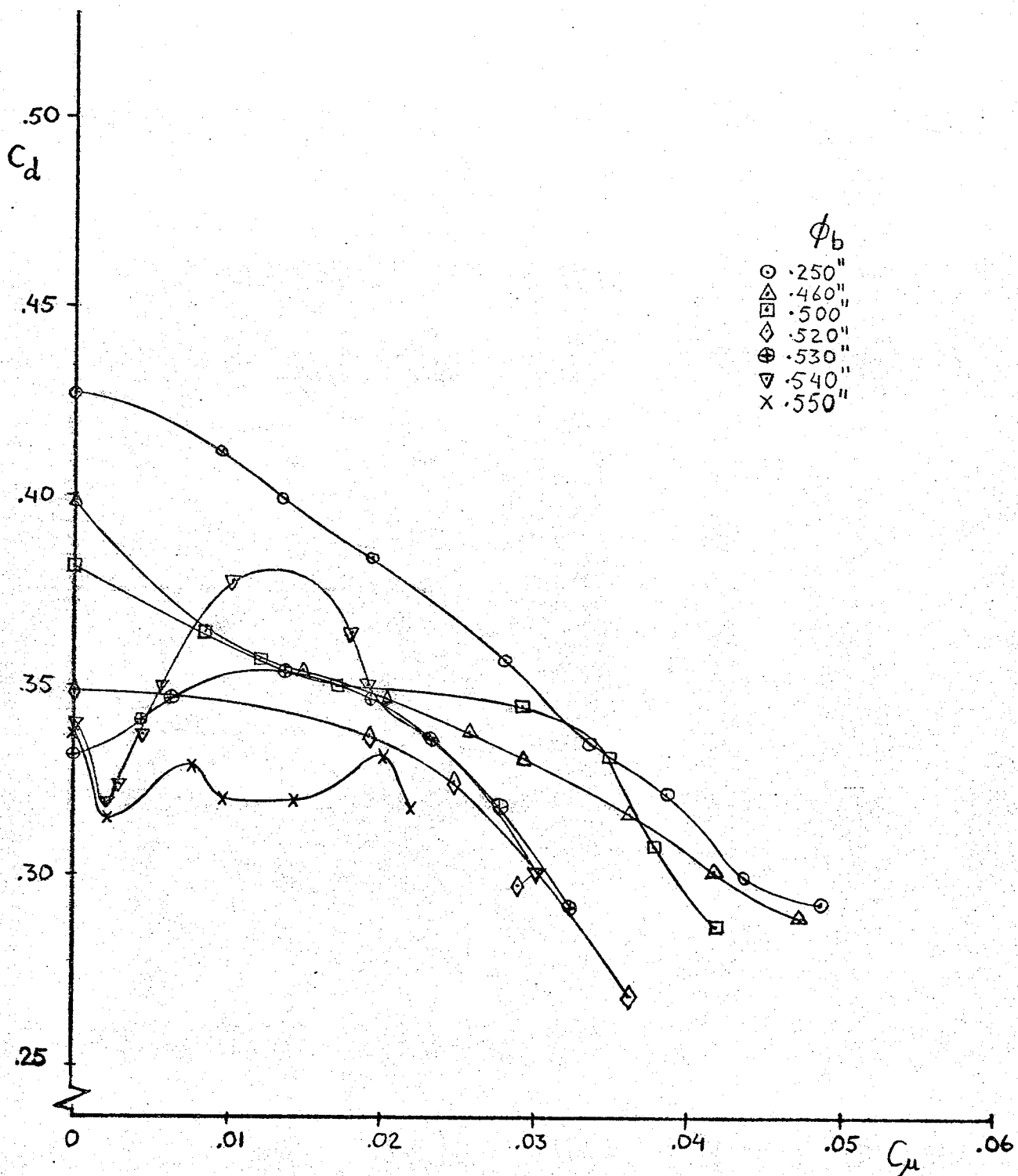


FIG.19 VARIATION OF DRAG WITH BLEED FOR MODEL II WITH BASE CYLINDERS AND SPINE.

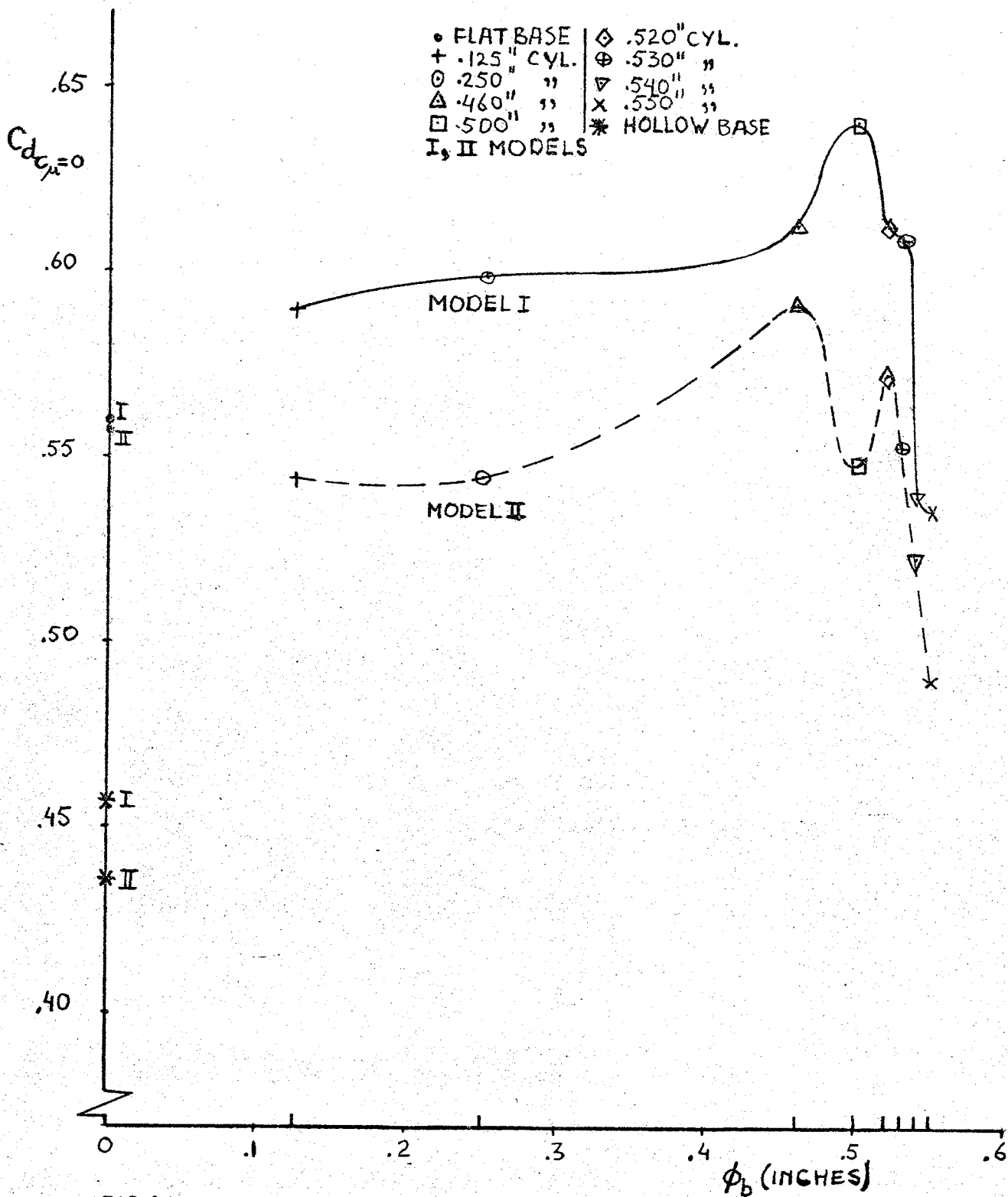


FIG.20 VARIATION OF DRAG AT ZERO BLEED WITH BASE CYLINDER DIAMETER.

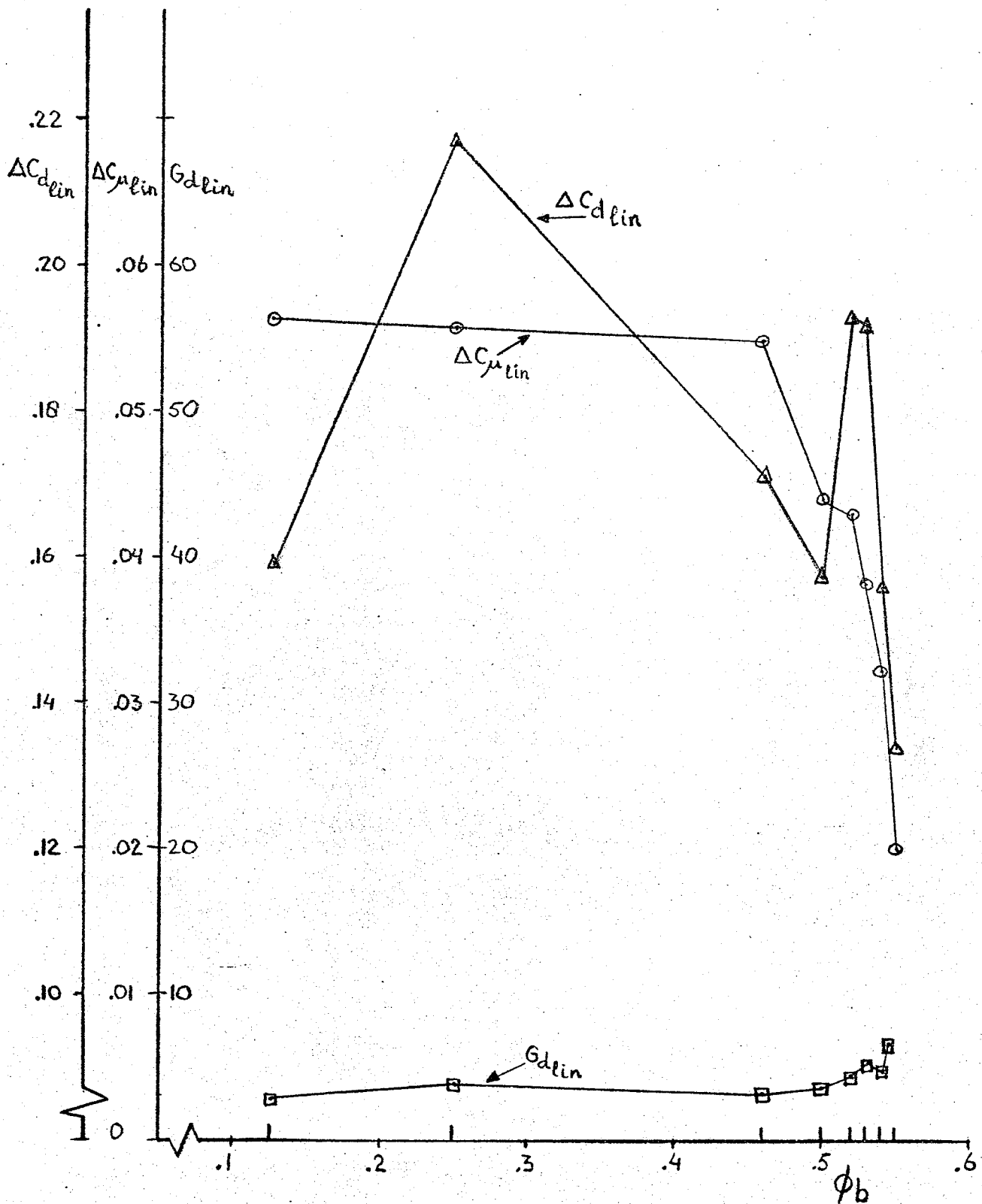


FIG.21 VARIATION OF BLEED CHARACTERISTICS WITH BASE CYLINDER DIAMETER FOR MODEL I.

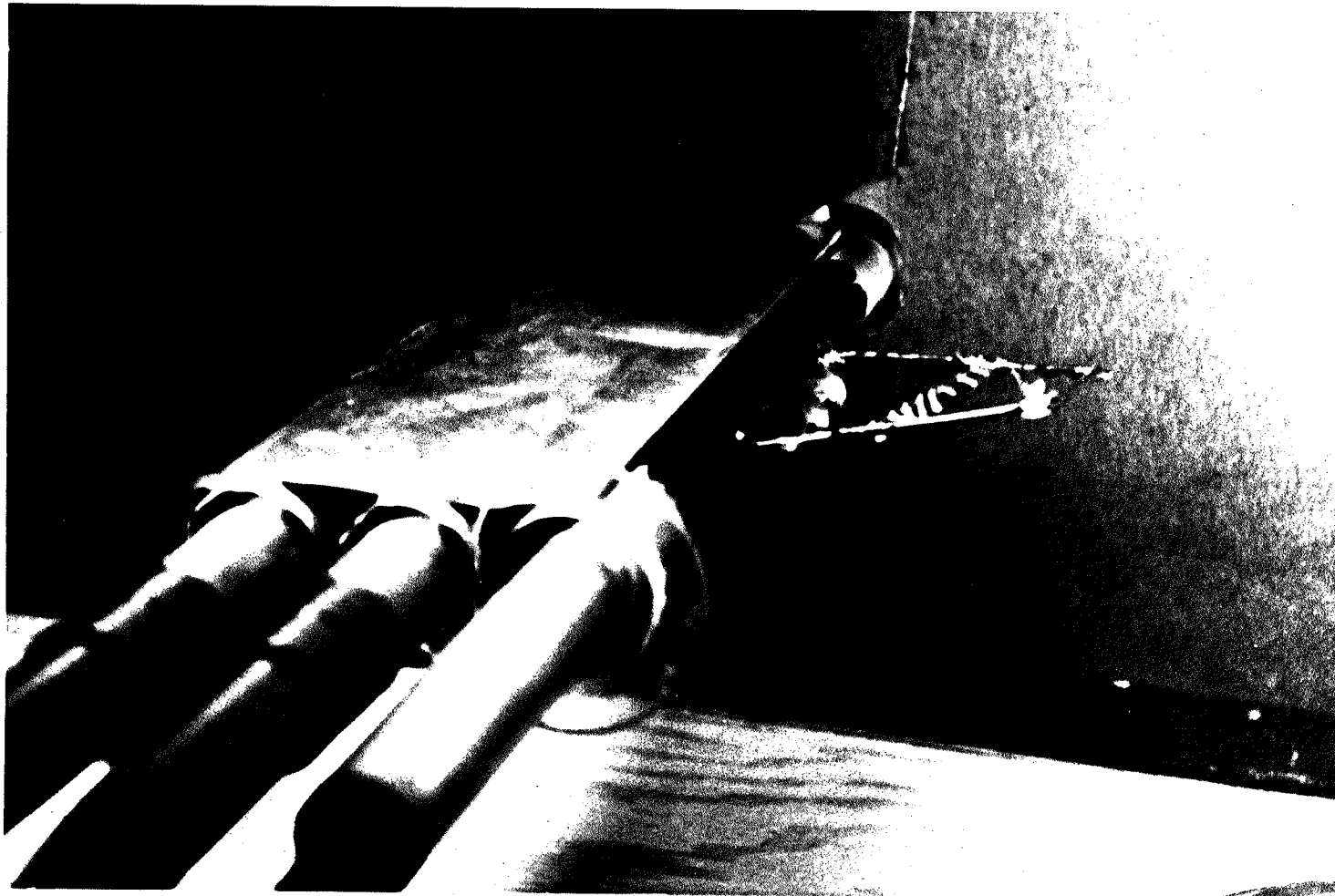


FIG. 23 MODEL AND WAKE RAKE ARRANGEMENT

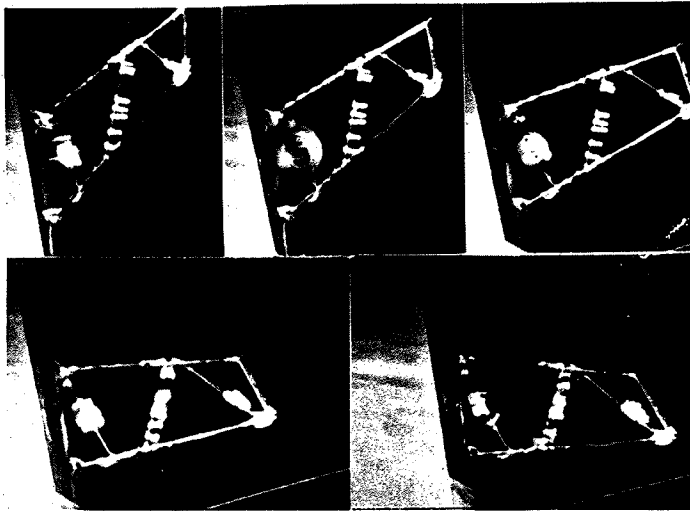


FIG. 24 a ZERO BLEED RATE $C_{\mu} = 0$



FIG. 24 b MAXIMUM BLEED RATE $C_{\mu} = \text{MAX.}$

FIG. 24 WAKE RAKE AT DIFFERENT ANGLES AND BLEEDRATES

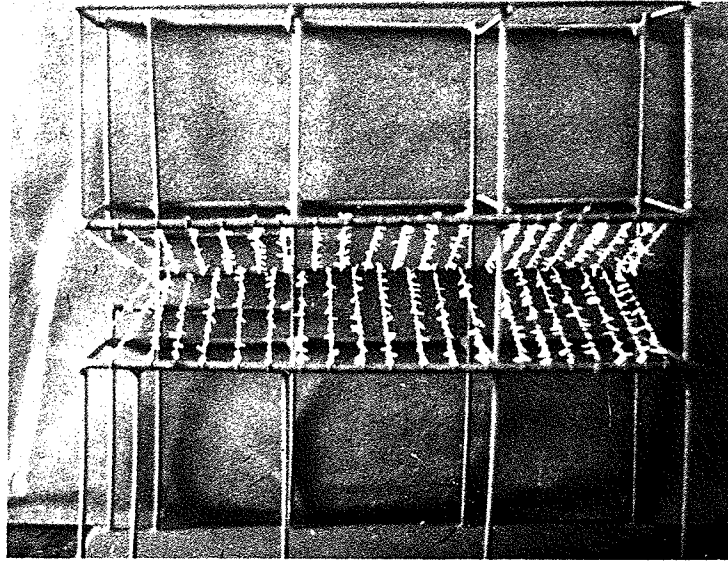
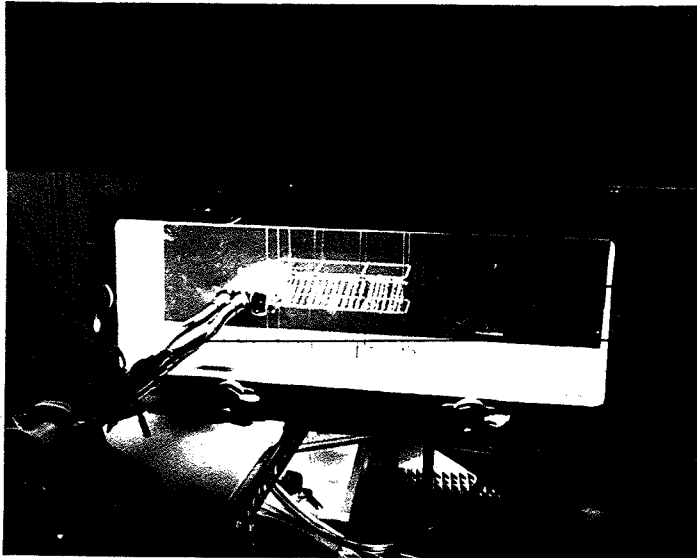


FIG. 25 STRIP-GRID FOR FLOW VISUALIZATION



- TUNNEL
- STRIP-GRID
- BLEED-ARRANGMENT

FIG. 26 a MODEL AND STRIP-GRID ARRANGEMENT



- REFLECTION COVER
- FLOODLIGHT
- FLASH UNIT
- TRI-POD FOR LIGHT SOURCES
- CAMERA POSITION
- TRI-POD FOR CAMERA

FIG. 26 b ARRANGEMENT OF CAMERA AND LIGHTSOURCES
 FIG. 26 STRIP-GRID AND CAMERA ARRANGEMENT FOR FLOW VISUALIZATION

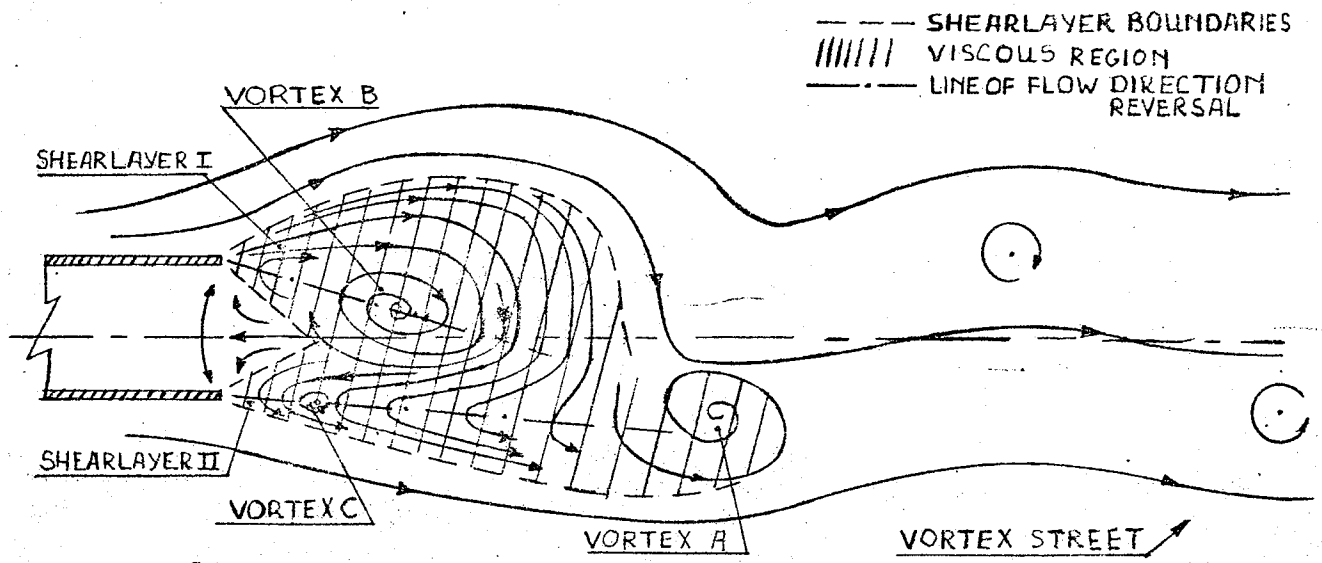


FIG. 27^a NO BLEED

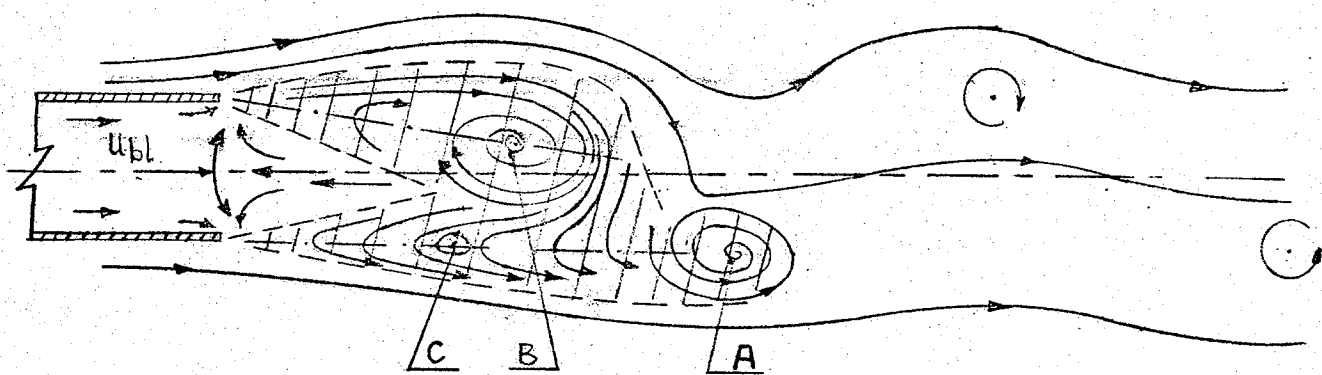


FIG. 27^b LOW BLEED RATE



FIG. 27^c MODERATE BLEEDRATE

FIG. 27 FLOW MODELS FOR WIDE OPEN BASES.

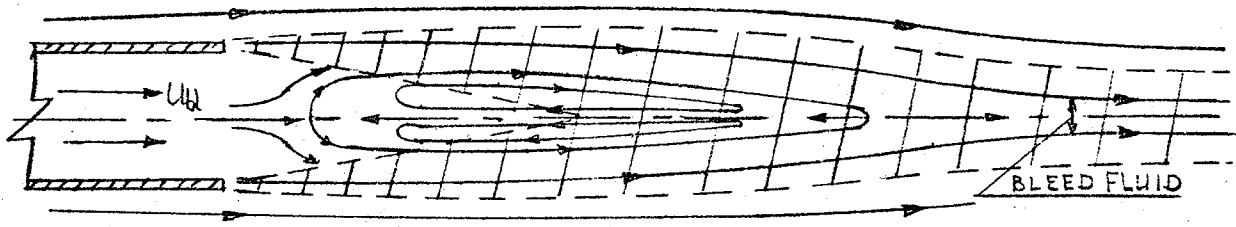


FIG. 27^d HIGH BLEEDRATE .

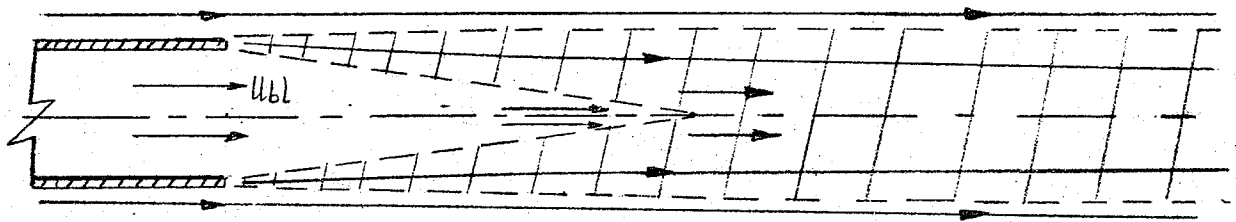


FIG. 27^e VERY HIGH BLEEDRATE

FIG. 27 FLOW MODELS FOR WIDE OPEN BASES.

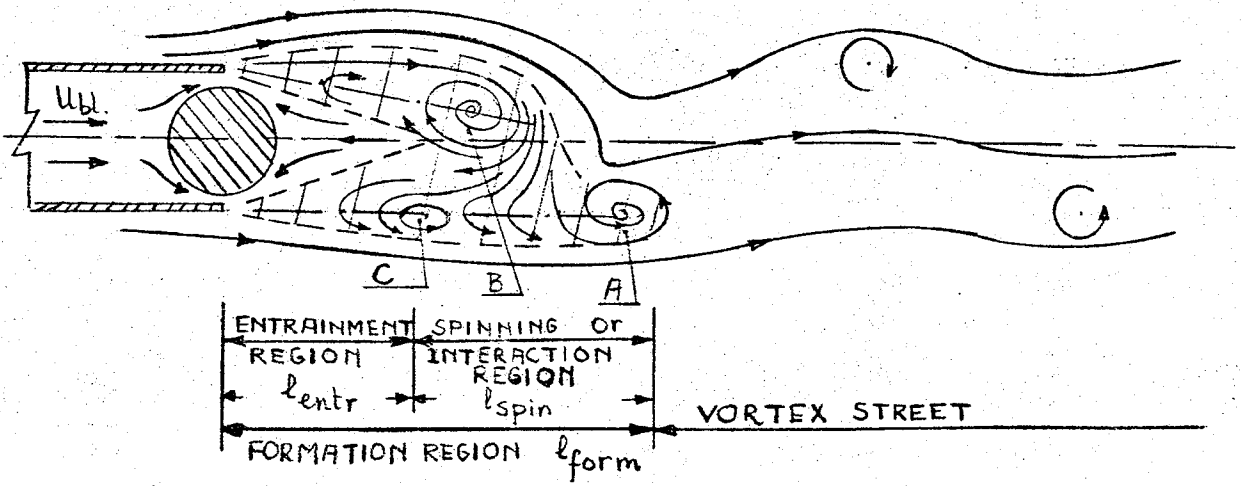


FIG. 28 FLOW MODEL FOR CONFIGURATIONS WITH BASE CYLINDERS.

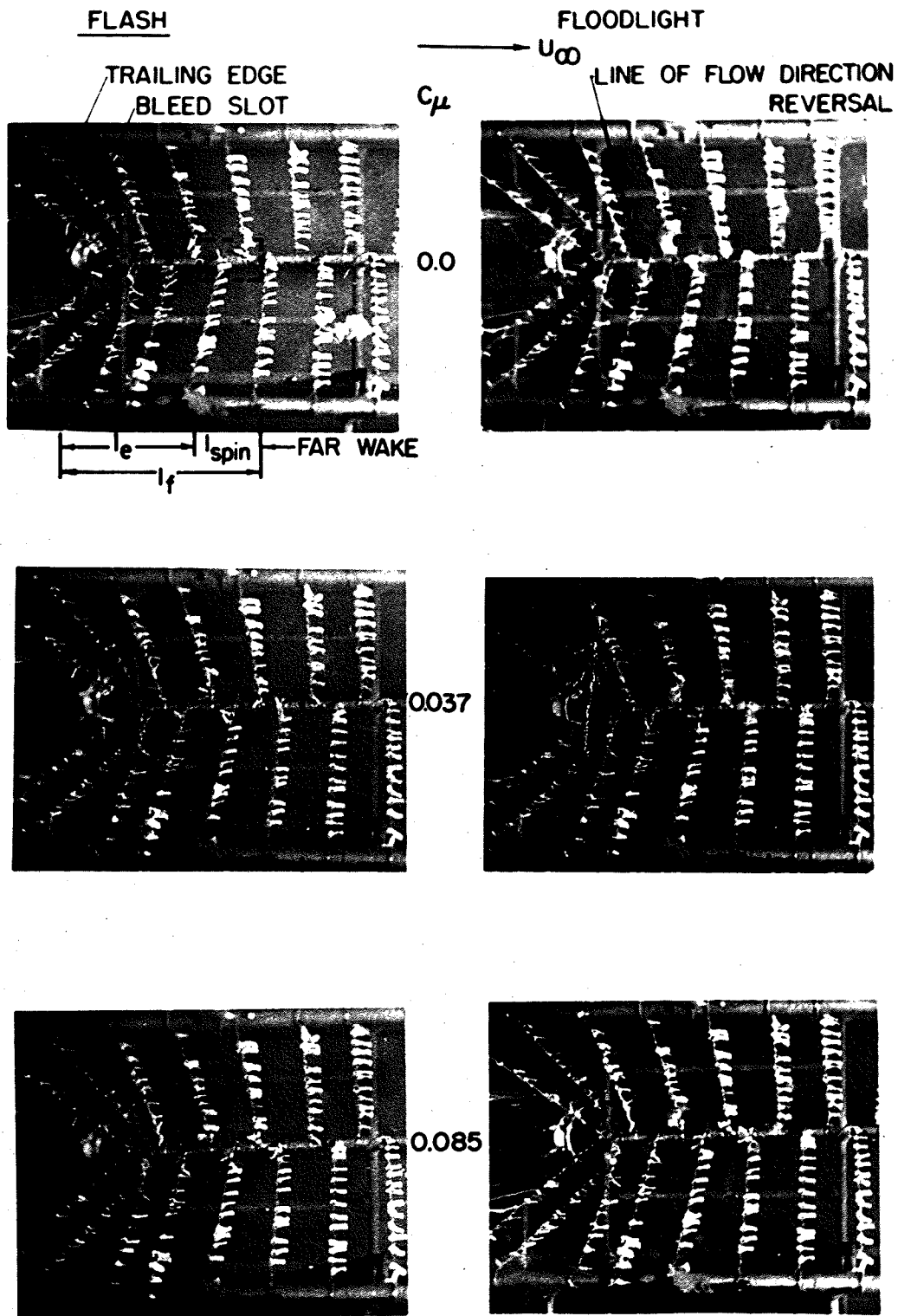


FIG. 29 FLOW PATTERN FOR CHAMFERED TRAILING EDGES AND WIDE OPEN BASE

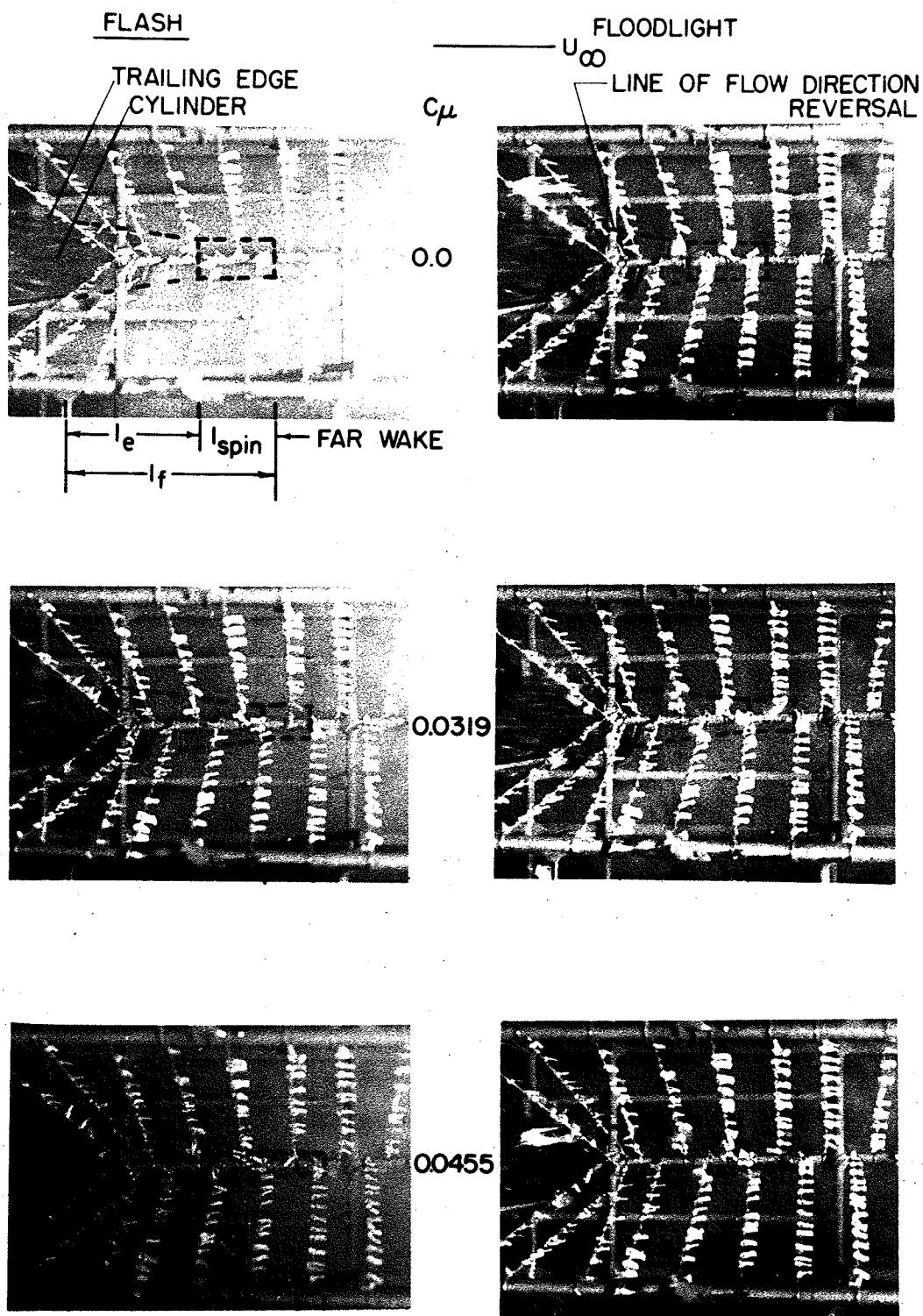


FIG. 30 FLOW PATTERN FOR BLUNT TRAILING EDGES AND $\phi_b = 0.500''$

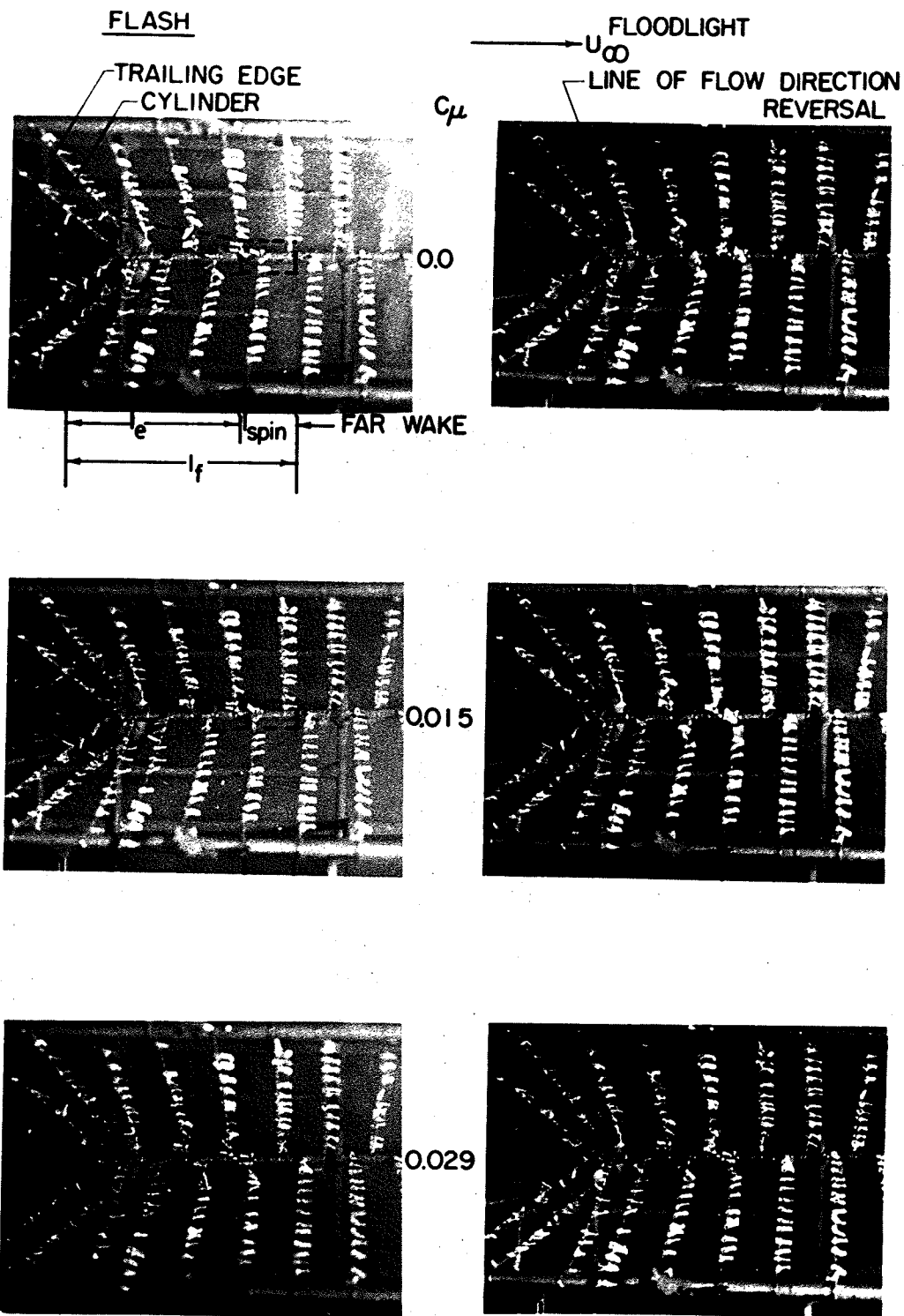


FIG. 31 FLOW PATTERN FOR BLUNT TRAILING EDGES AND $\phi = 0.550''$

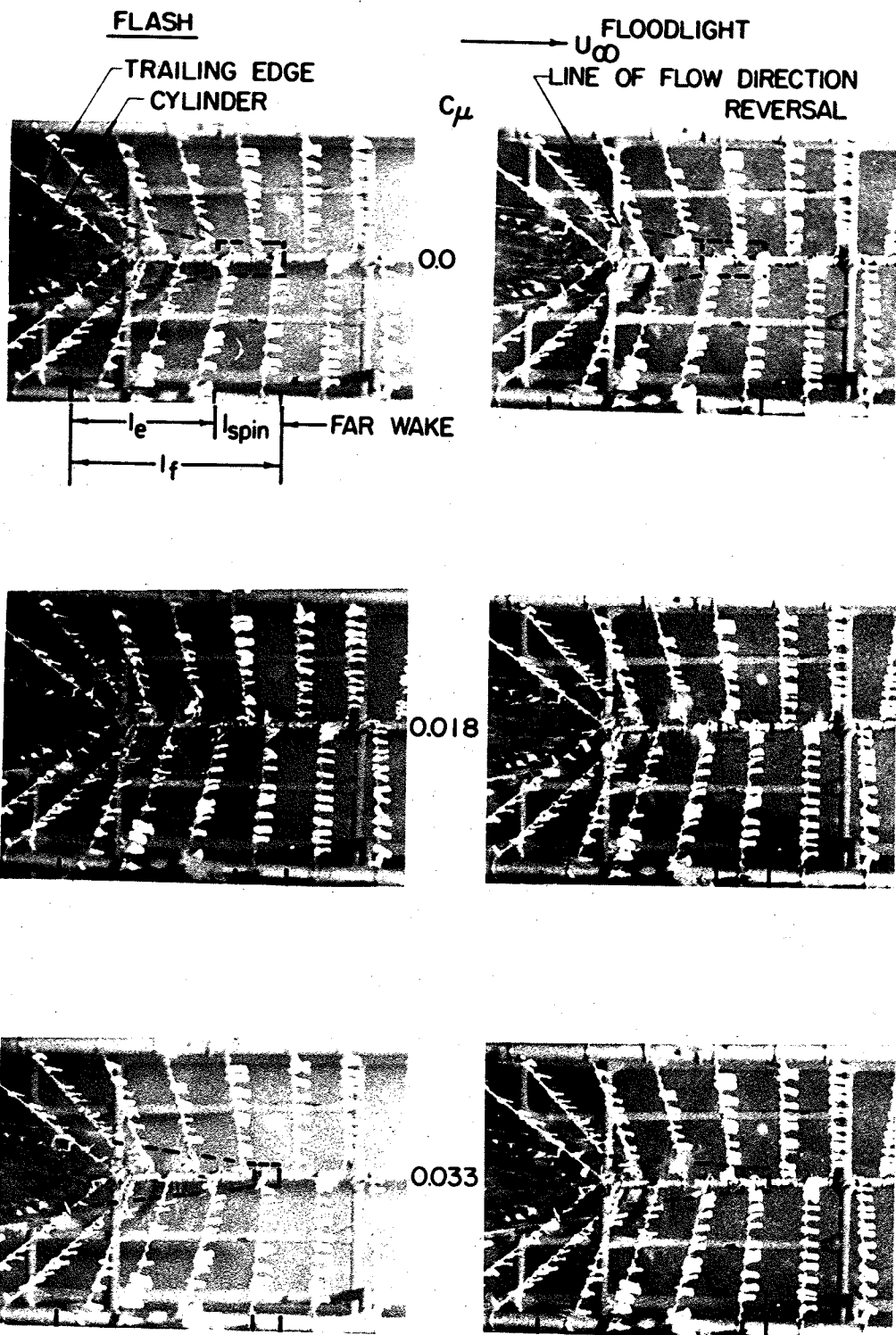
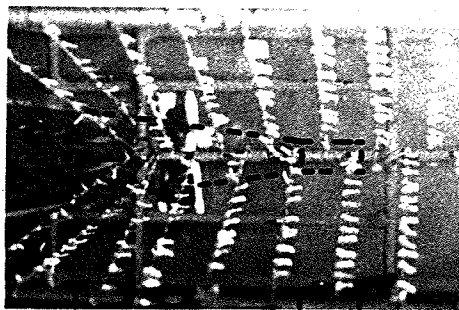
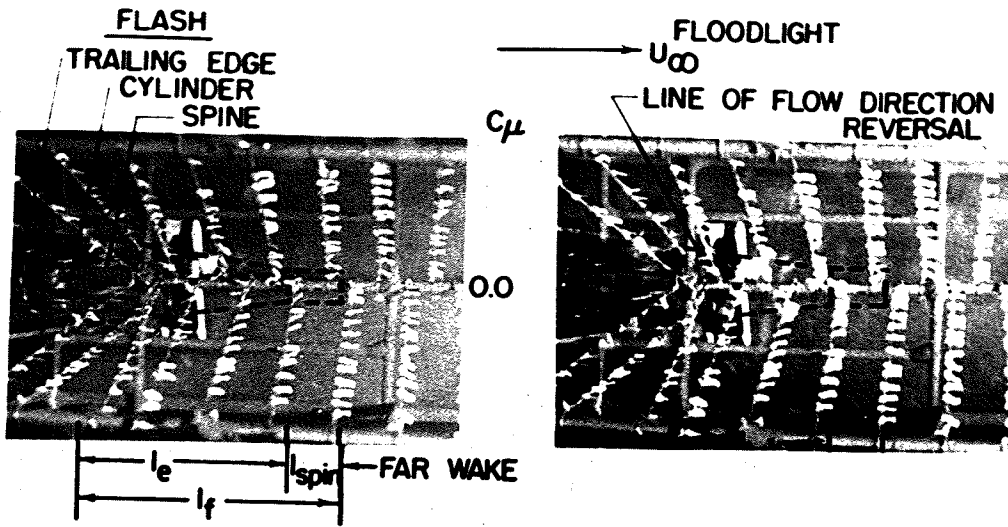
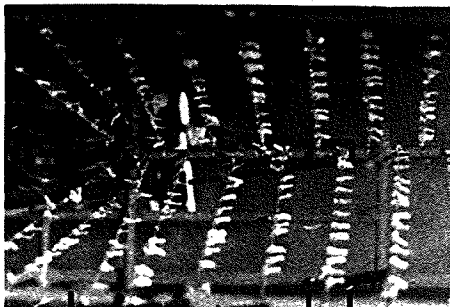


FIG. 32 FLOW PATTERN FOR CHAMFERED TRAILING EDGES AND $\phi_b = 0.550''$



00343



0076



FIG. 33 FLOW PATTERN FOR BLUNT TRAILING EDGES AND $\phi_b = 0.460^\circ$ WITH SPINE

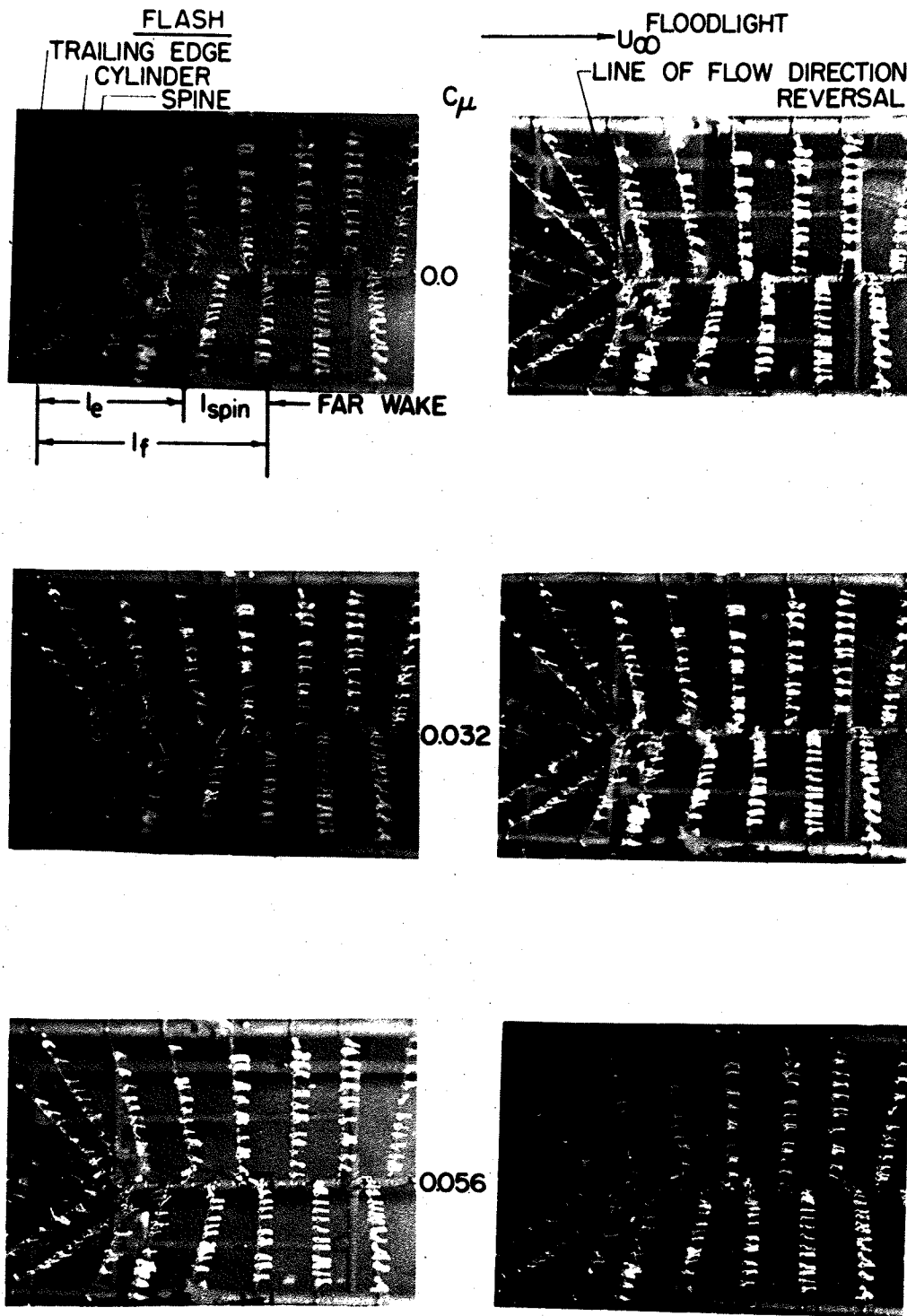
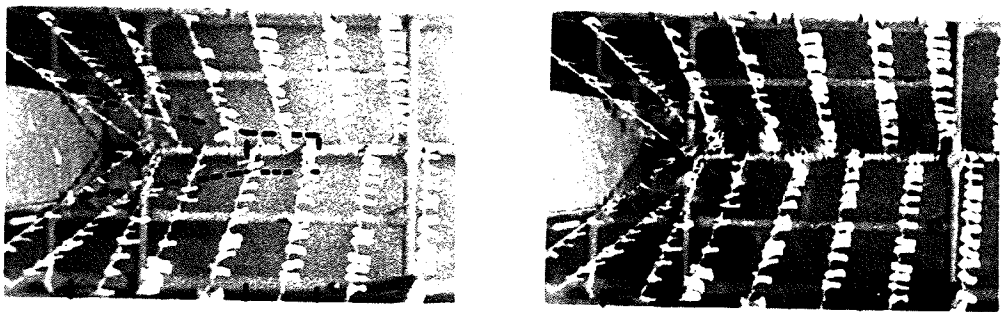
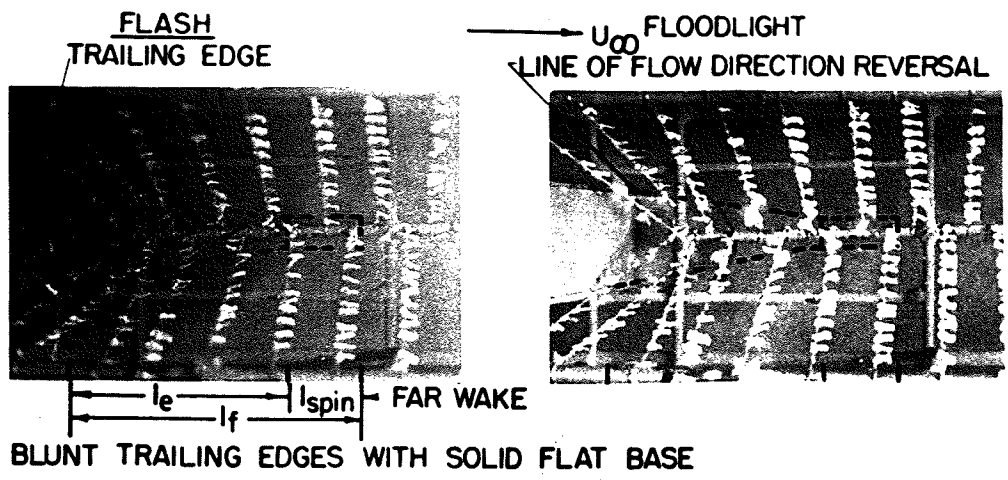
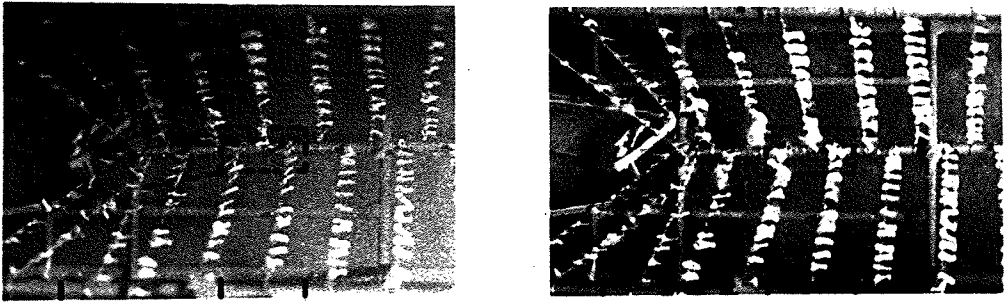


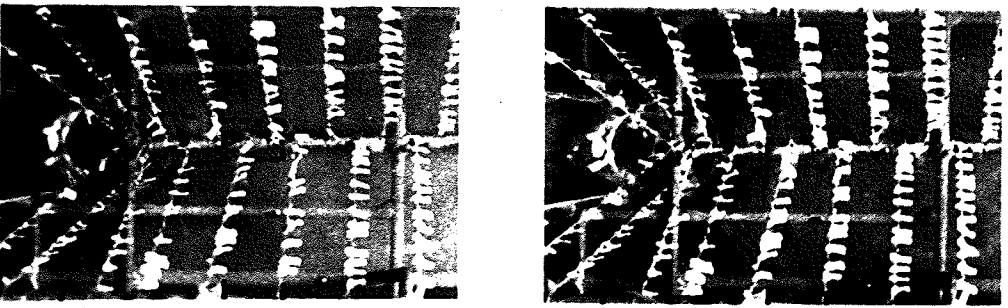
FIG. 34 FLOW PATTERN FOR CHAMFERED TRAILING EDGES AND
 $\phi_b = 0.460''$ WITH SPINE



CHAMFERED TRAILING EDGES WITH SOLID FLAT BASE



BLUNT TRAILING EDGES WITH CONCAVE BASE



CHAMFERED TRAILING EDGES WITH CONCAVE BASE
 FIG. 35 FLOW PATTERN FOR FLAT AND CONCAVE BASES

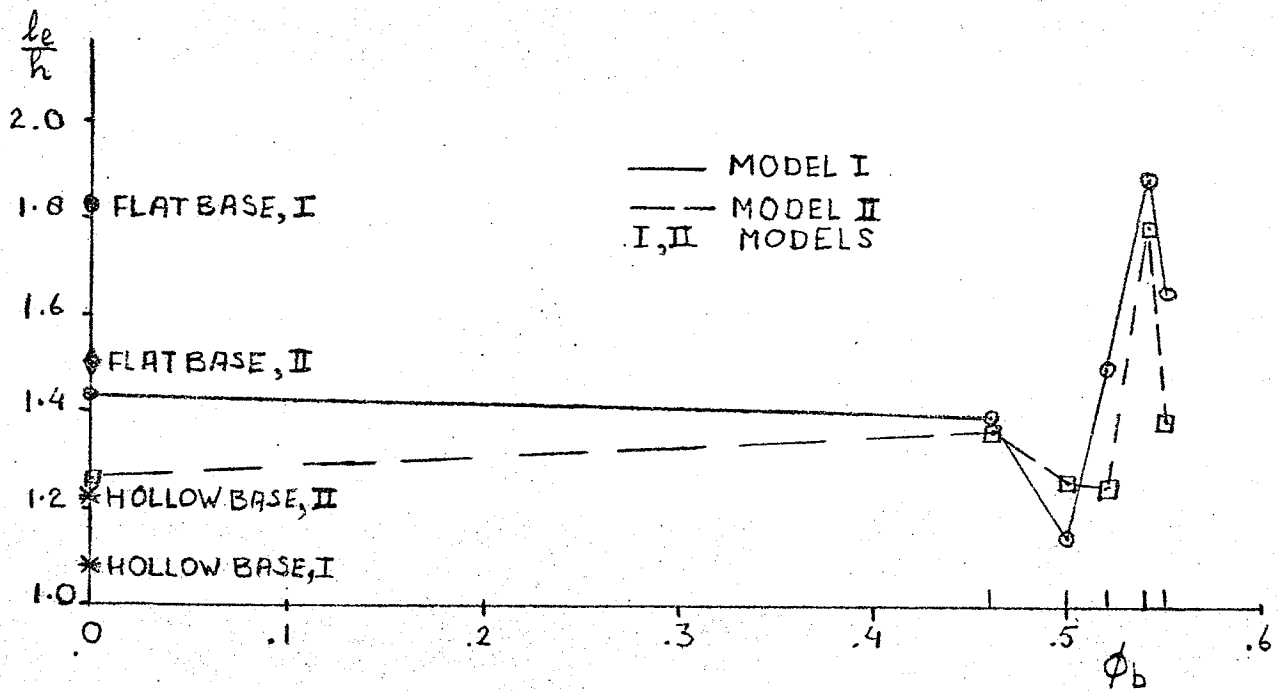


FIG. 36 EFFECT OF BASE CYLINDER DIAMETER ON THE ENTRAINMENT LENGTH AT ZERO BLEED RATE.

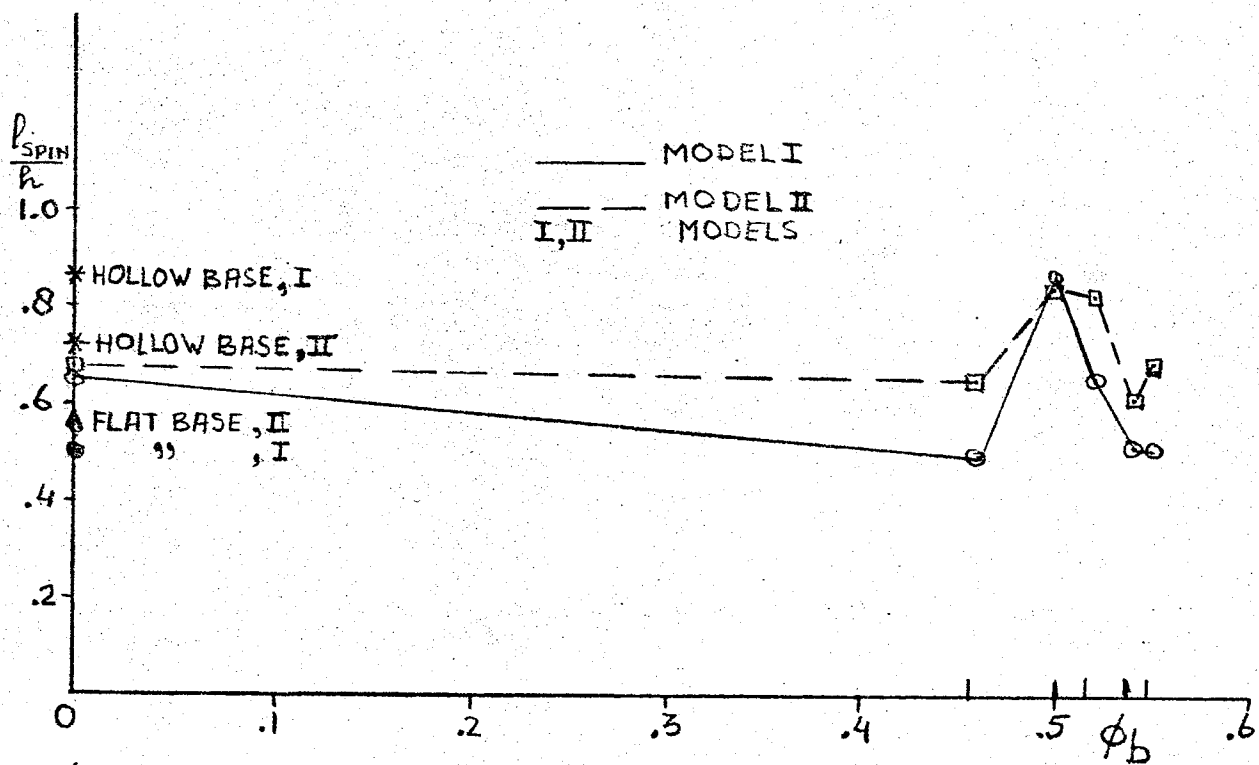


FIG. 37 EFFECT OF BASE CYLINDER DIAMETER ON THE SPINNING LENGTH AT ZERO BLEED RATE.

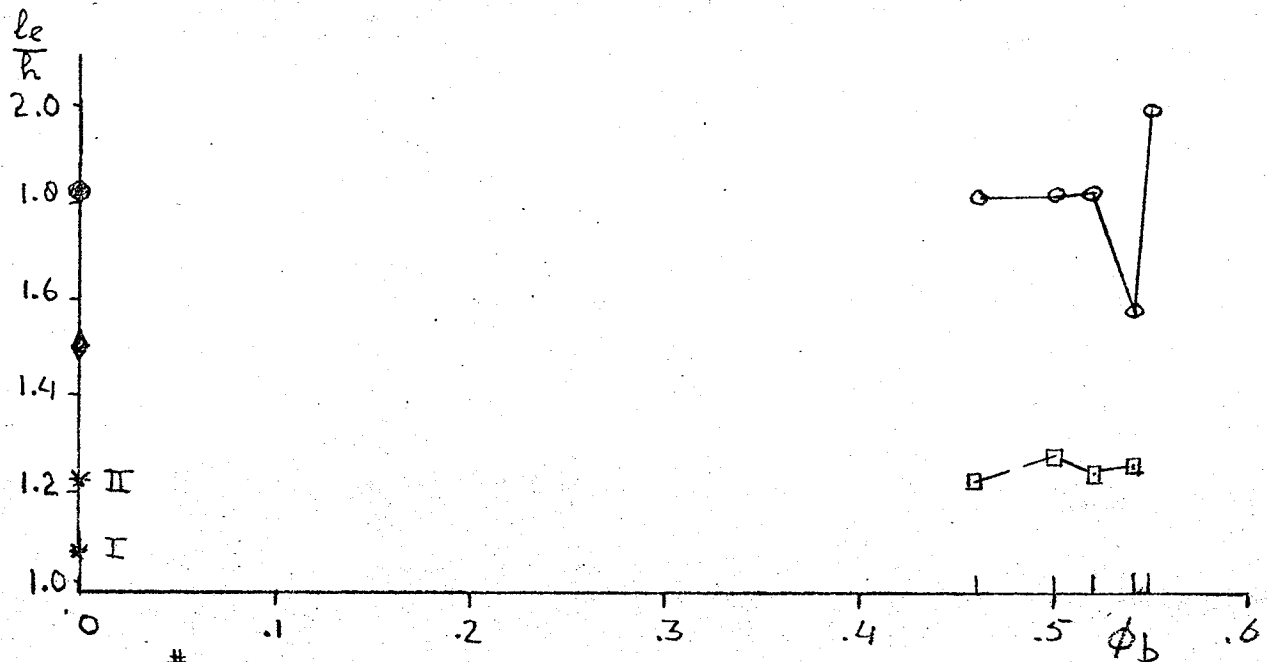


FIG. 38# EFFECT OF CYLINDERS AND SPINE ON THE ENTRAINMENT LENGTH AT ZERO BLEEDRATE.

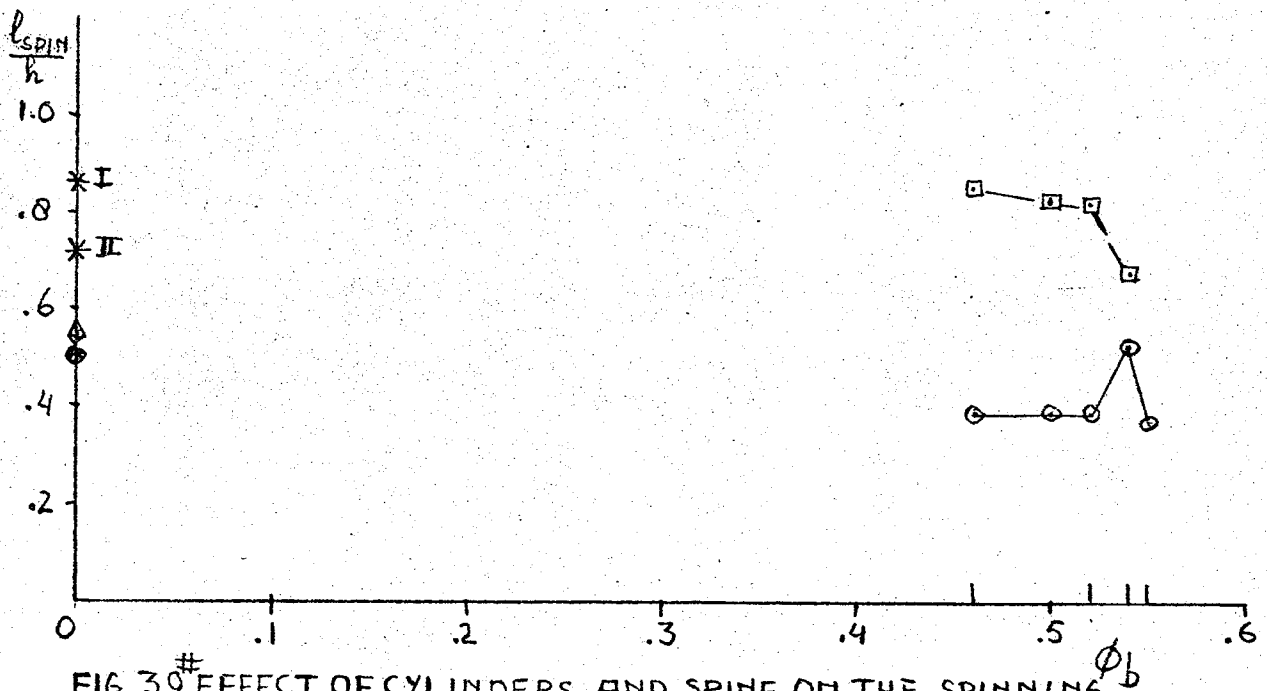


FIG. 39# EFFECT OF CYLINDERS AND SPINE ON THE SPINNING LENGTH AT ZERO BLEEDRATE.

FOR NOMENCLATURE SEE FIG. 36, 37.

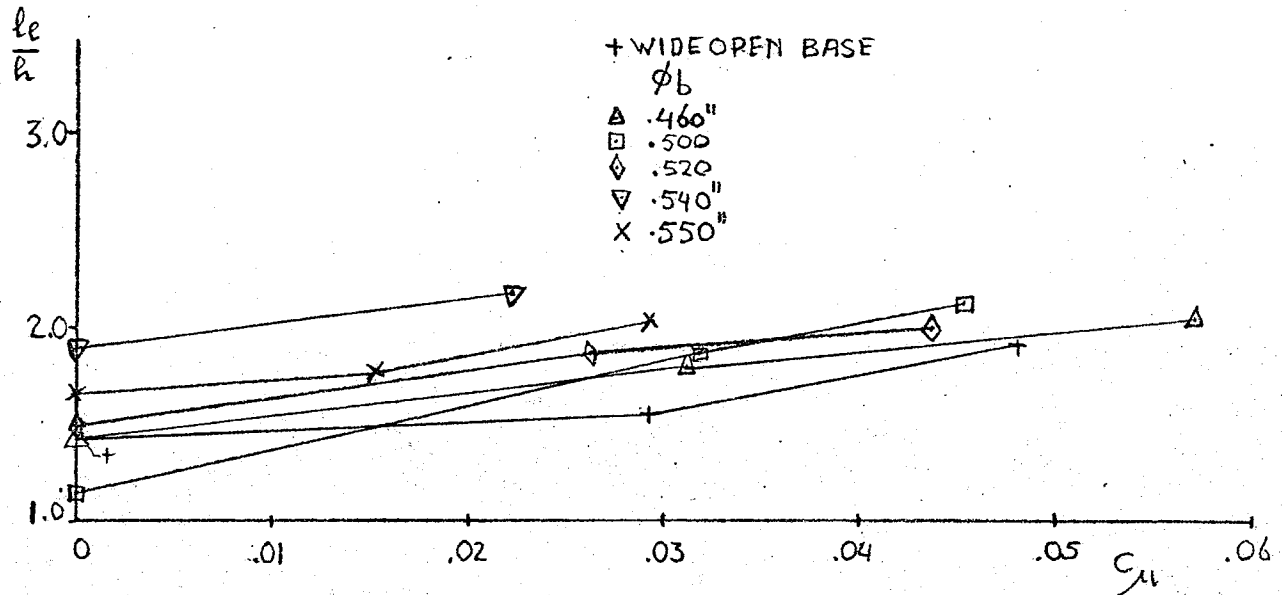


FIG.40 VARIATION OF THE ENTRAINMENT LENGTH WITH BLEED AND CYLINDER DIAMETER FOR MODEL I.

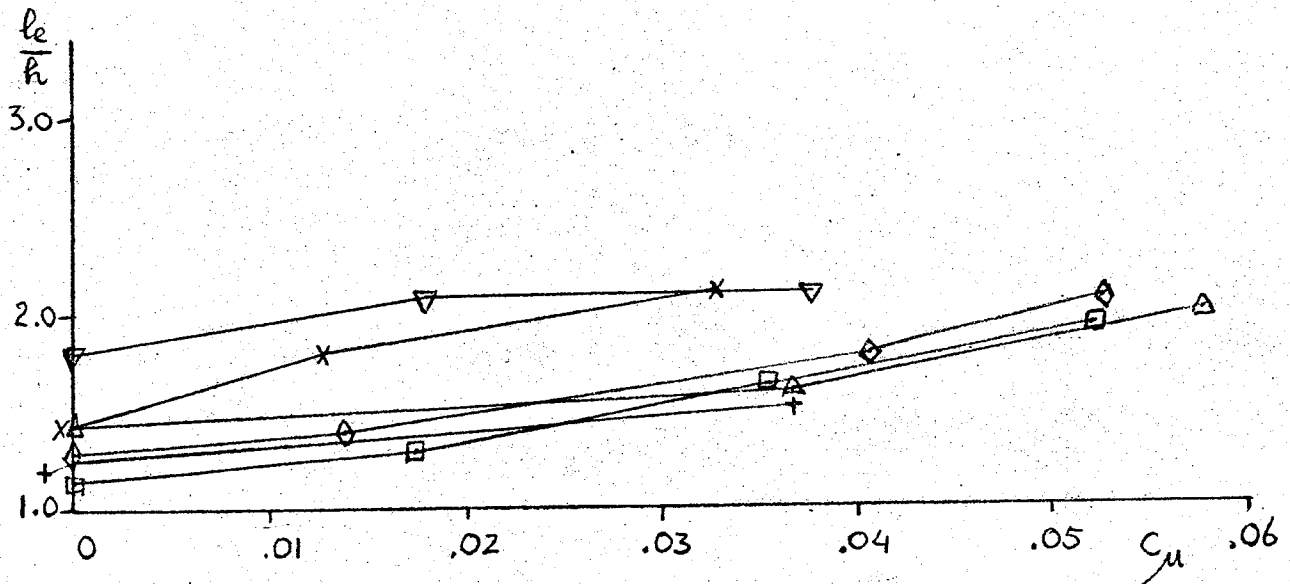
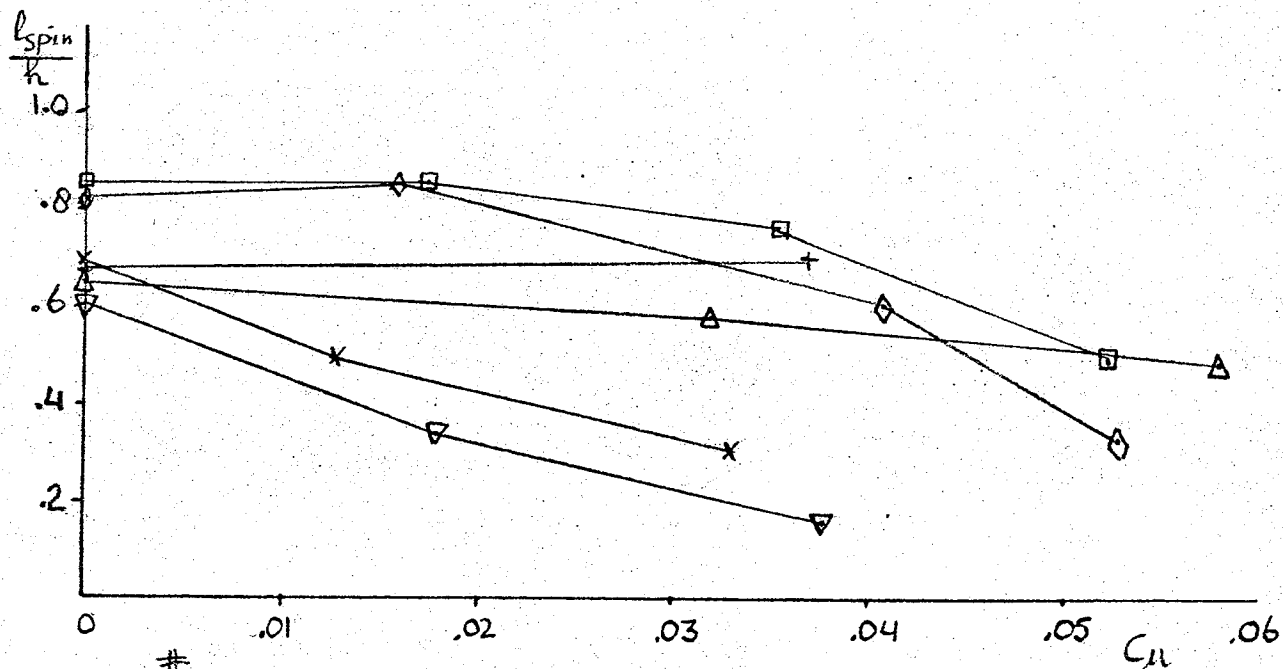
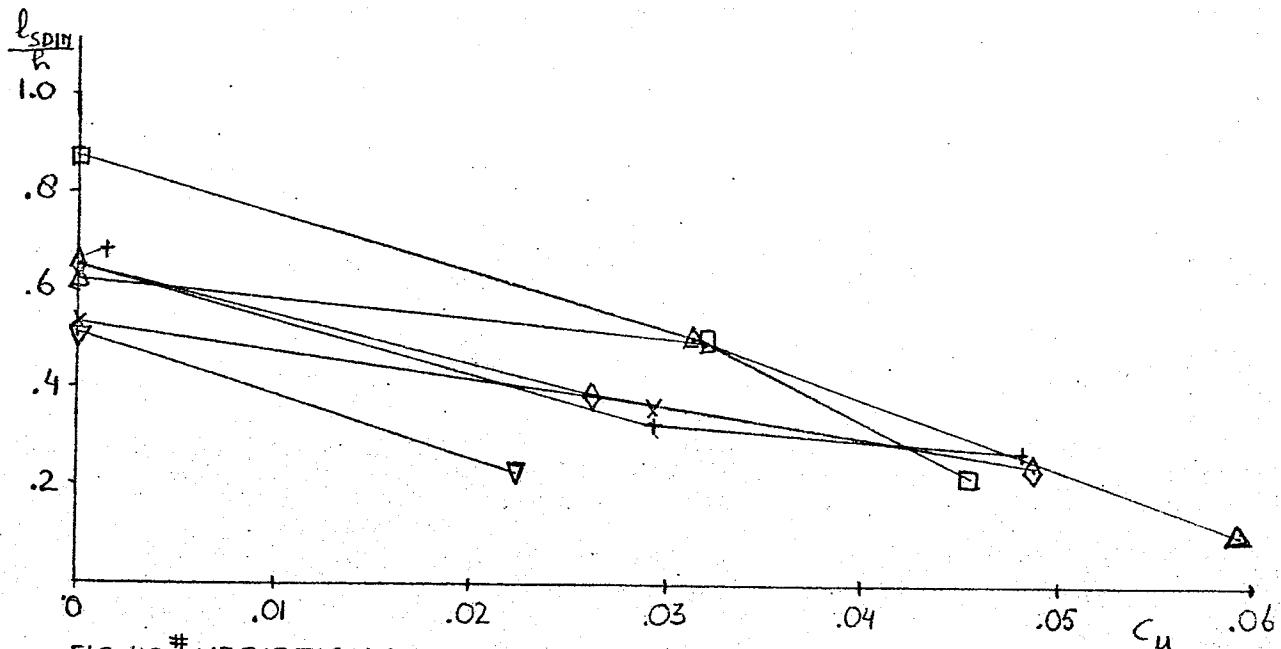


FIG.41 # VARIATION OF THE ENTRAINMENT LENGTH WITH BLEED AND CYLINDER DIAMETER FOR MODEL II.

FOR NOMENCLATURE SEE FIG.40.



#FOR NOMENCLATURE SEE FIG. 40.

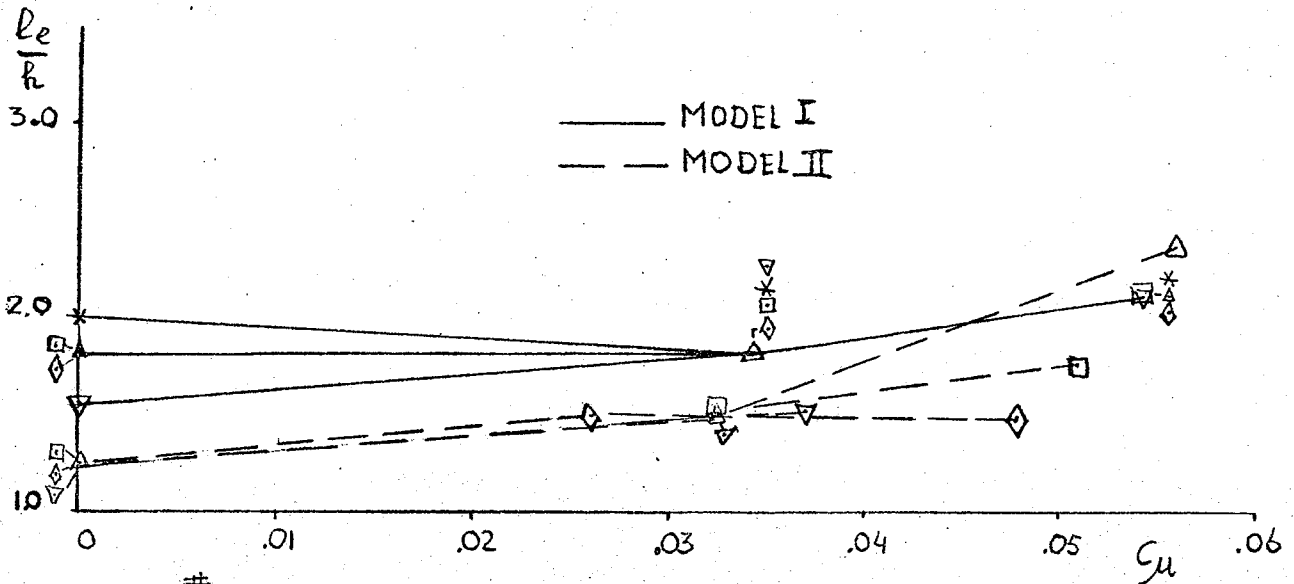


FIG.44# VARIATION OF THE ENTRAINMENT LENGTH WITH BLEED FOR CYLINDERS WITH SPINES.

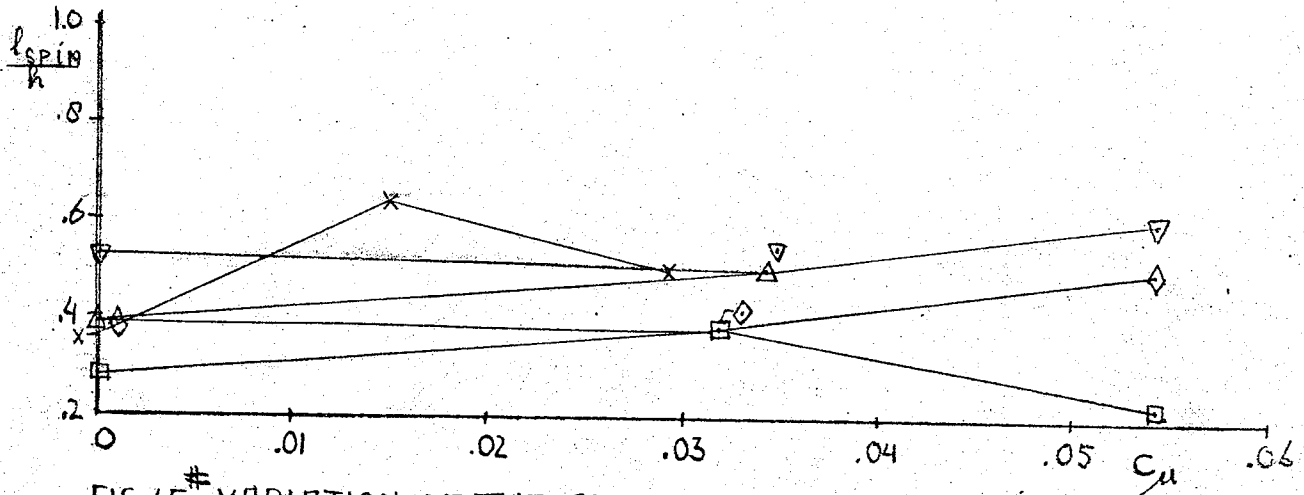


FIG.45# VARIATION OF THE SPINNING LENGTH WITH BLEED AND CYLINDERS WITH SPINES FOR MODEL I.

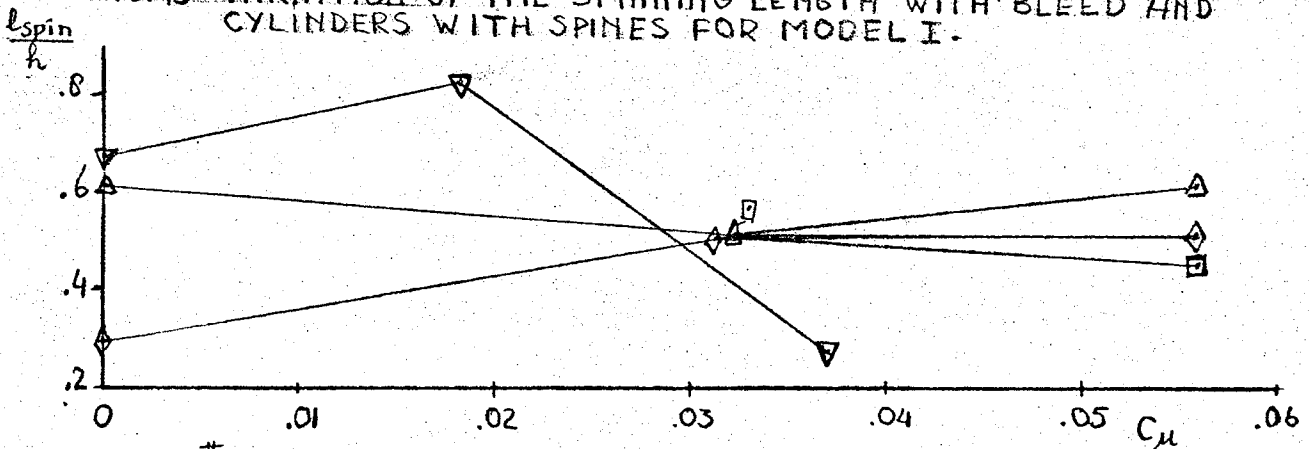


FIG.46# VARIATION OF THE SPINNING LENGTH WITH BLEED AND CYLINDERS WITH SPINES FOR MODEL II.

FOR NOMENCLATURE SEE FIG.40.

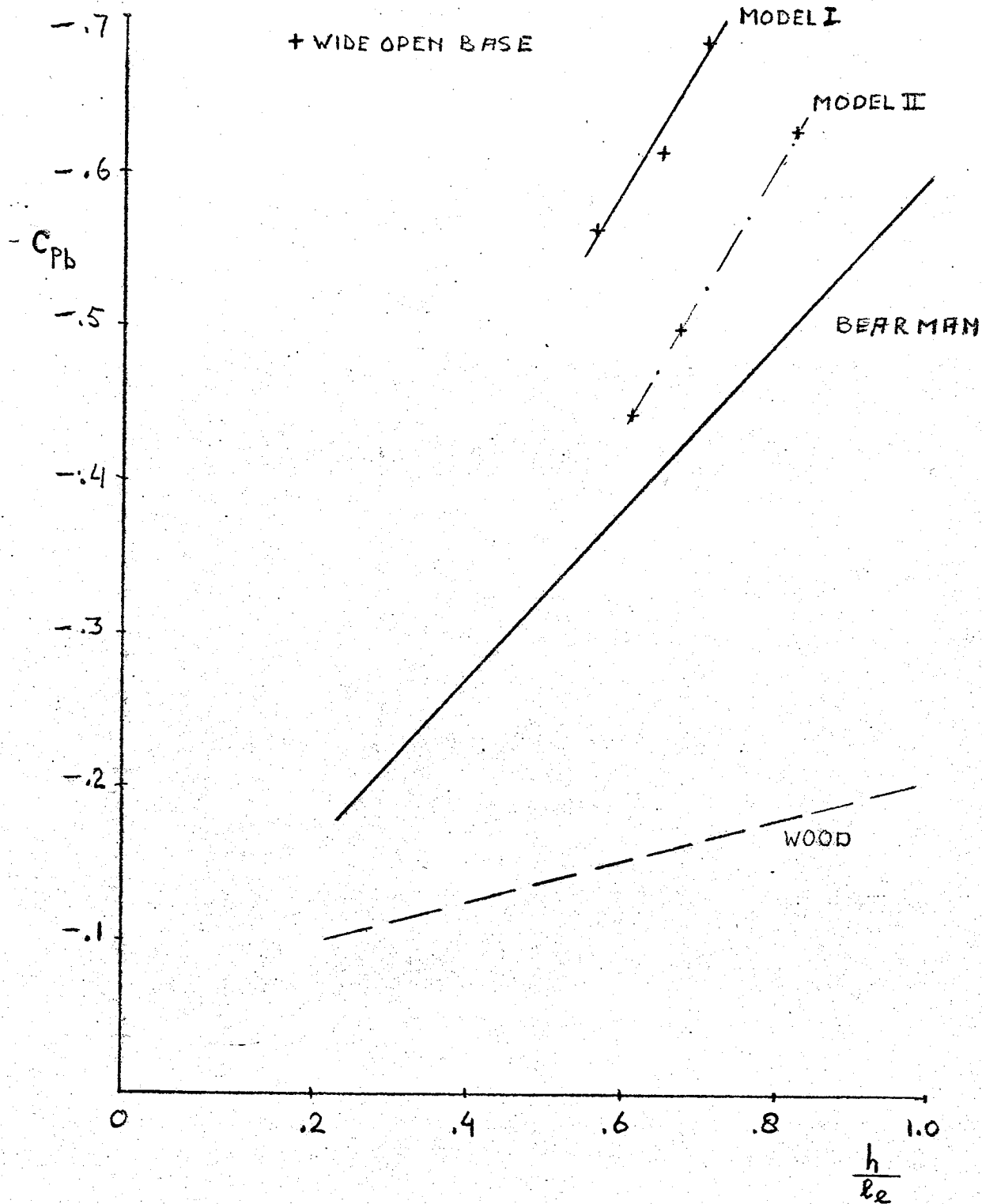


FIG 47^a CORRELATION OF BASE PRESSURE AND INVERSE OF THE ENTRAINMENT LENGTH.

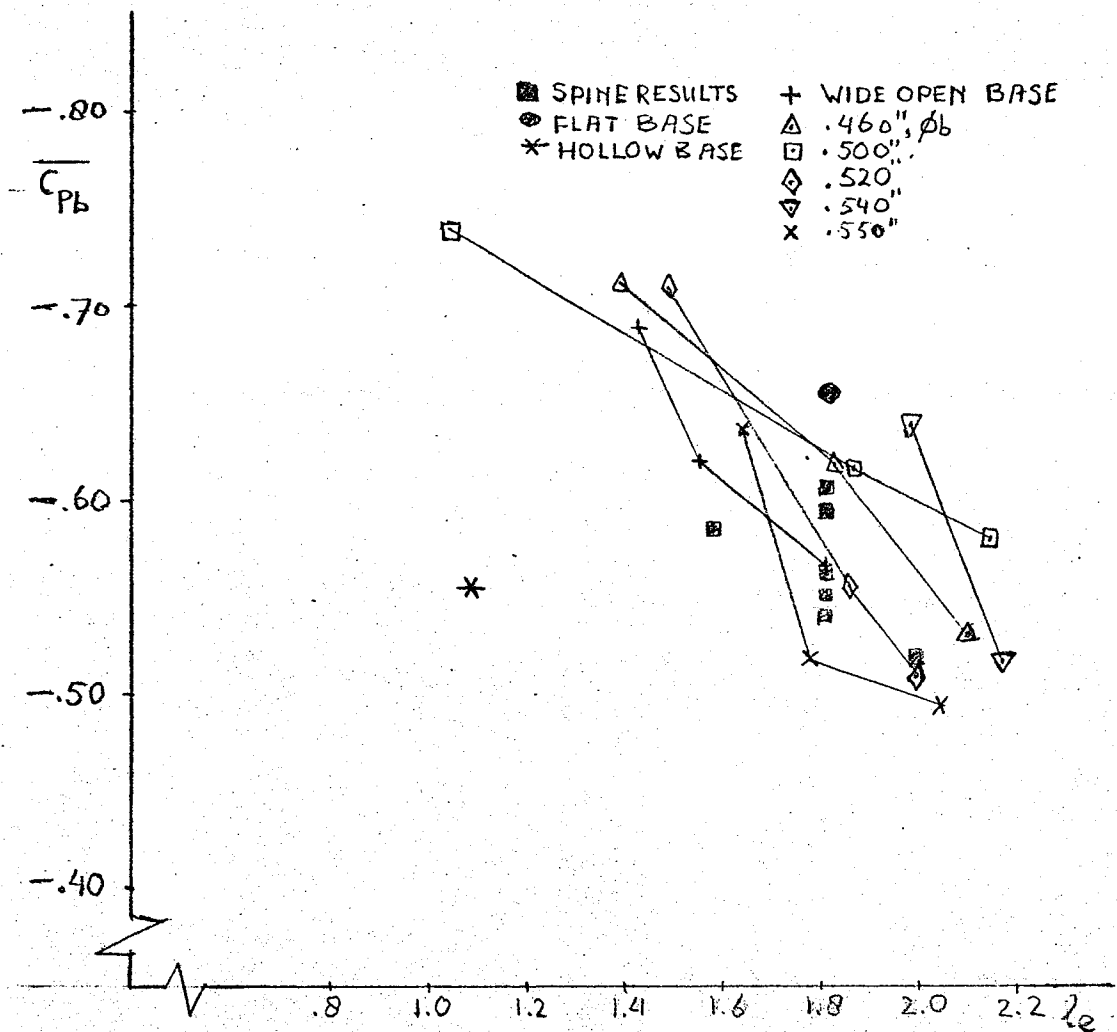


FIG. 47^b CORRELATION OF AVERAGE BASE PRESSURE AND THE ENTRAINMENT LENGTH FOR MODEL I.

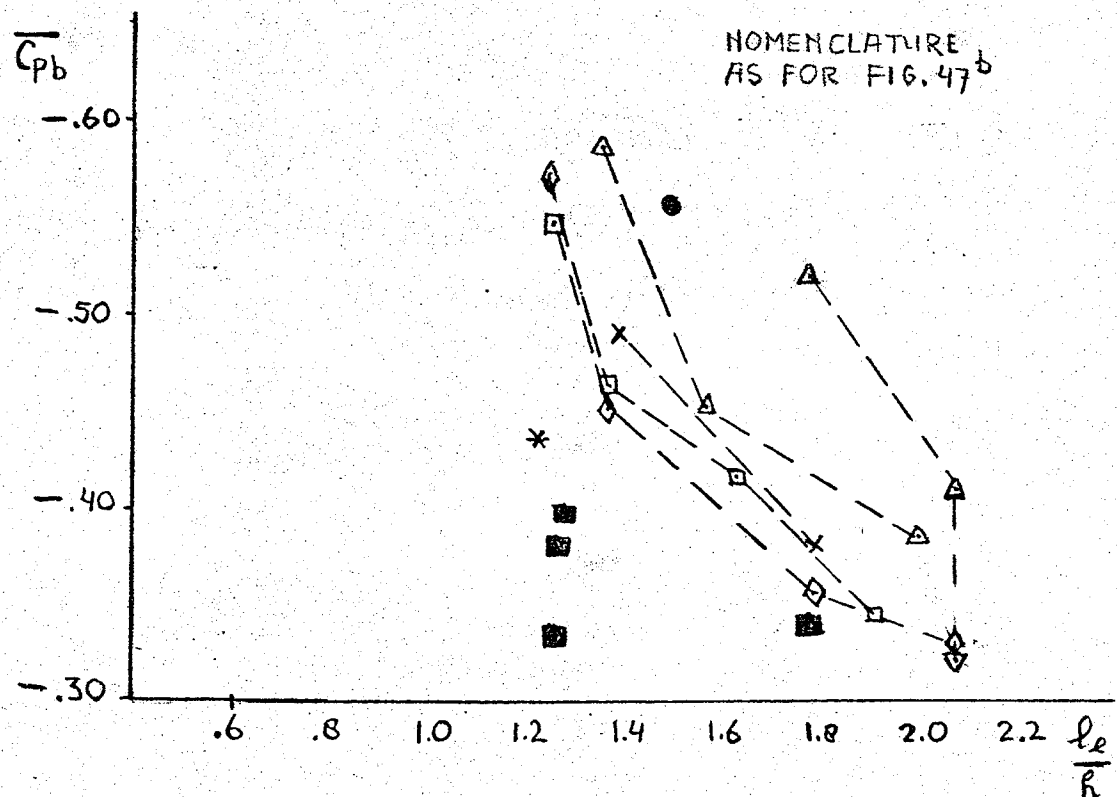


FIG. 47^c CORRELATION OF AVERAGE BASE PRESSURE FOR MODEL II.

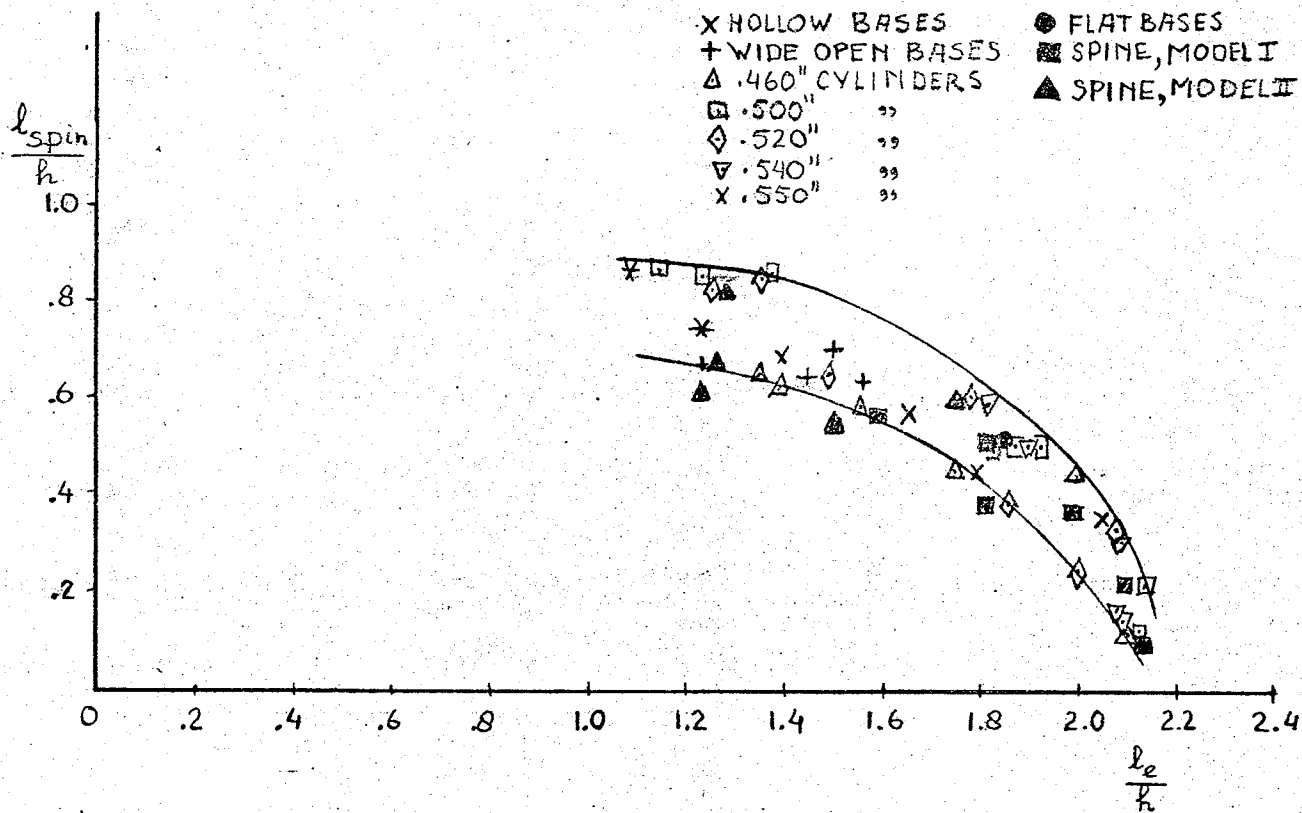


FIG.48 CORRELATION OF THE SPINNING LENGTH AND THE ENTRAINMENT LENGTH FOR ALL THE GEOMETRIES TESTED.

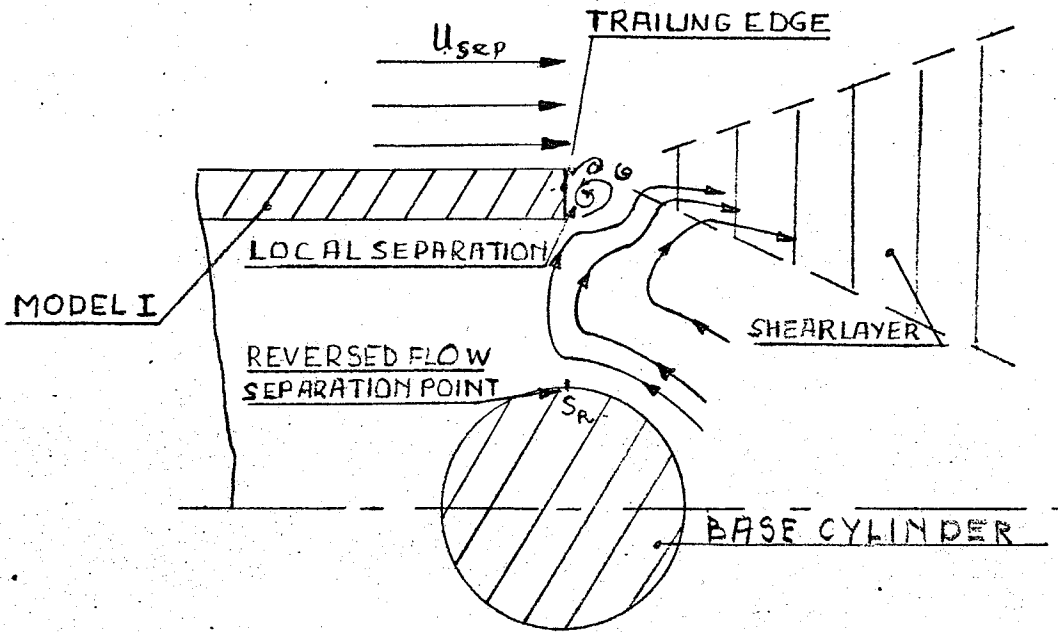


FIG. 49^a BLUNT TRAILING EDGE.

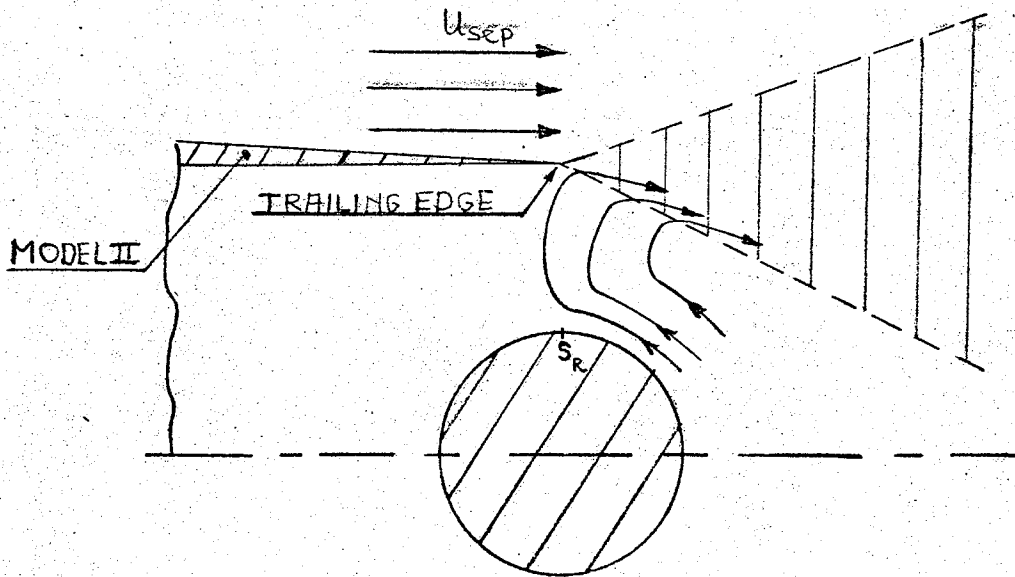


FIG. 49^b CHAMFERED TRAILING EDGE.

FIG. 49 THE "EDGE EFFECT".

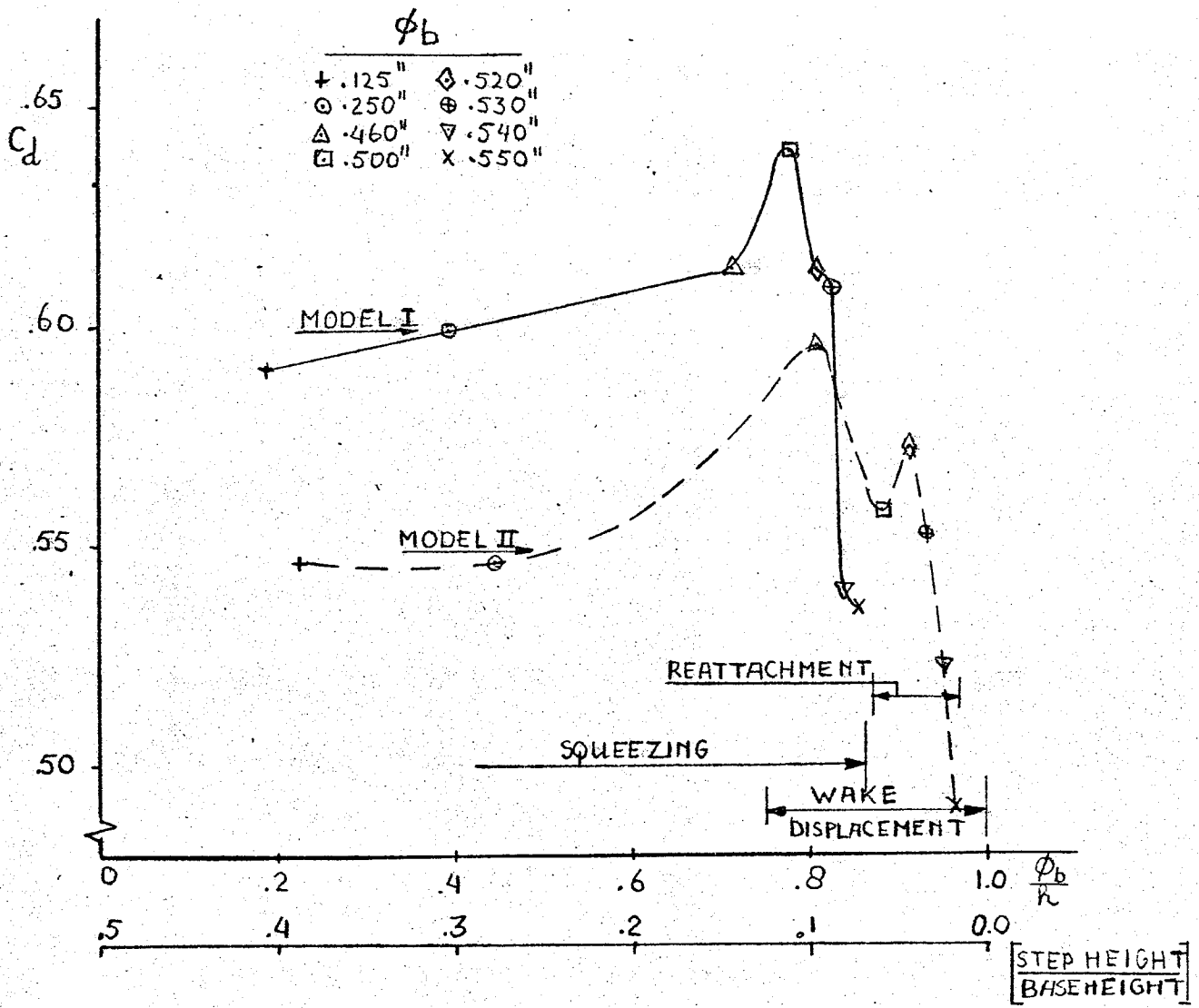


FIG.50 RELATION OF THE DRAG TO THE STEP HEIGHT.

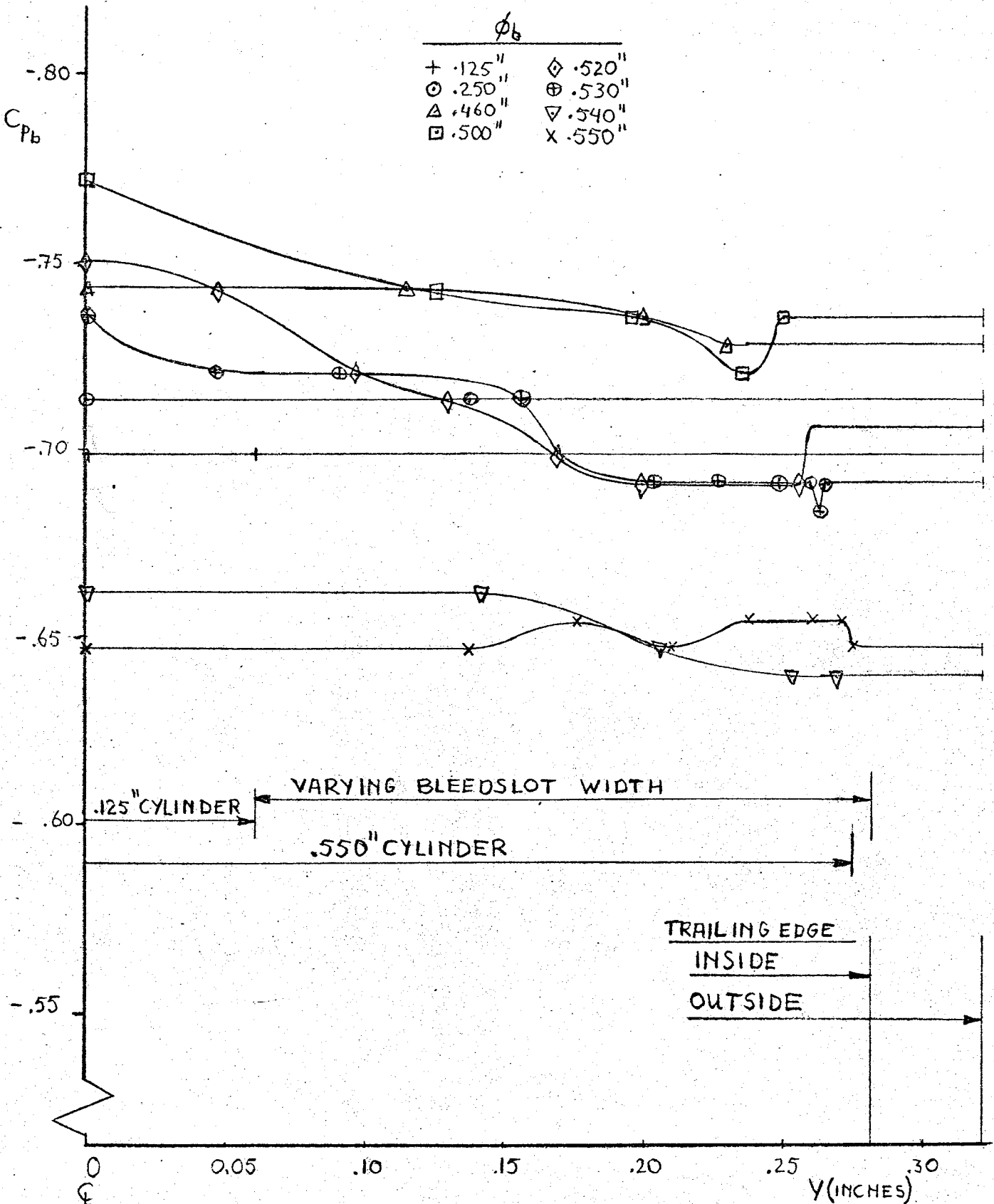


FIG. 51 PRESSURE DISTRIBUTIONS OVER BASE CYLINDERS FOR MODEL I AT ZERO BLEED.

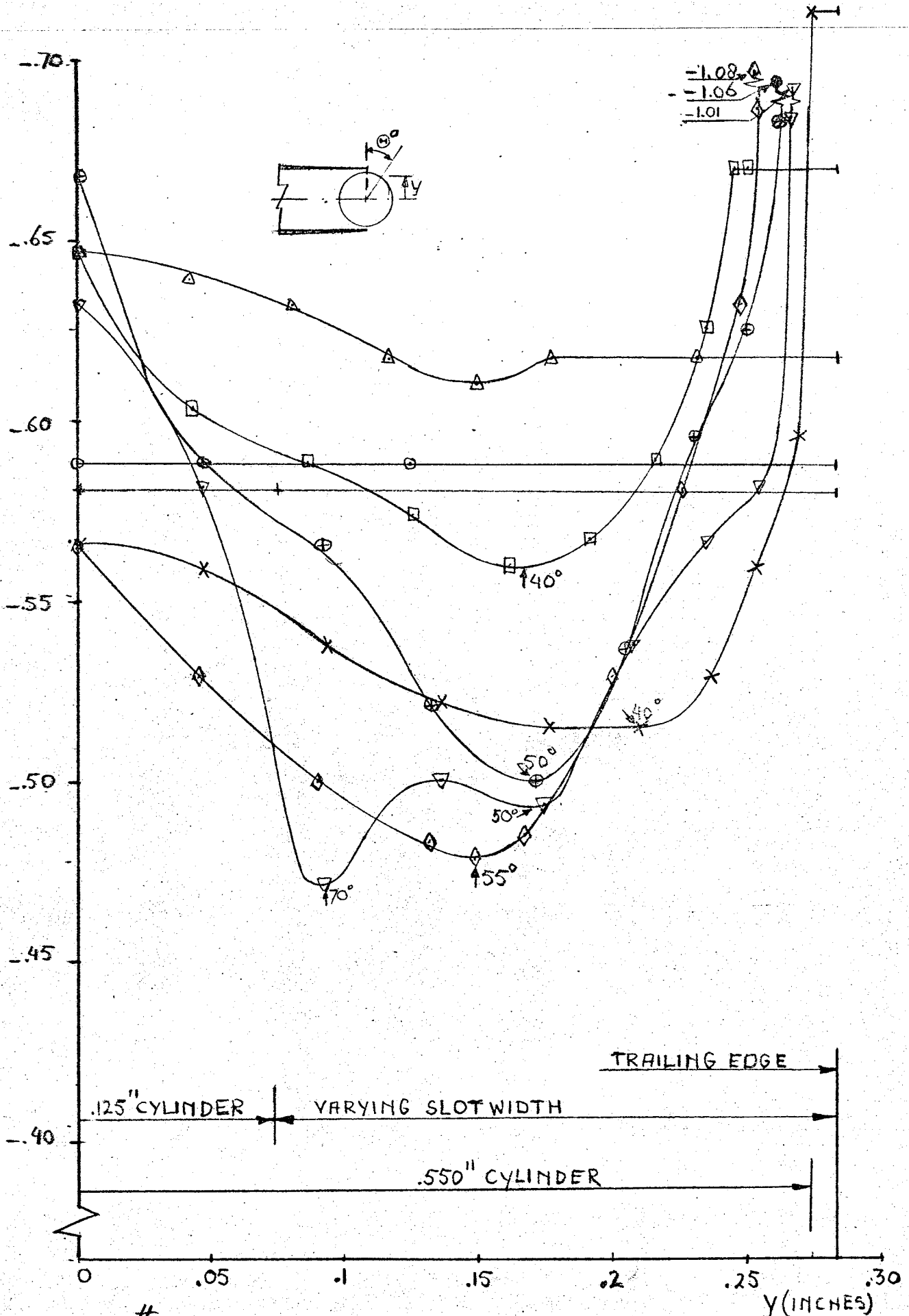


FIG.52 PRESSURE DISTRIBUTIONS OVER BASE CYLINDERS FOR MODEL II AT ZERO BLEED.

NOMENCLATURE QS FOR FIG.51.

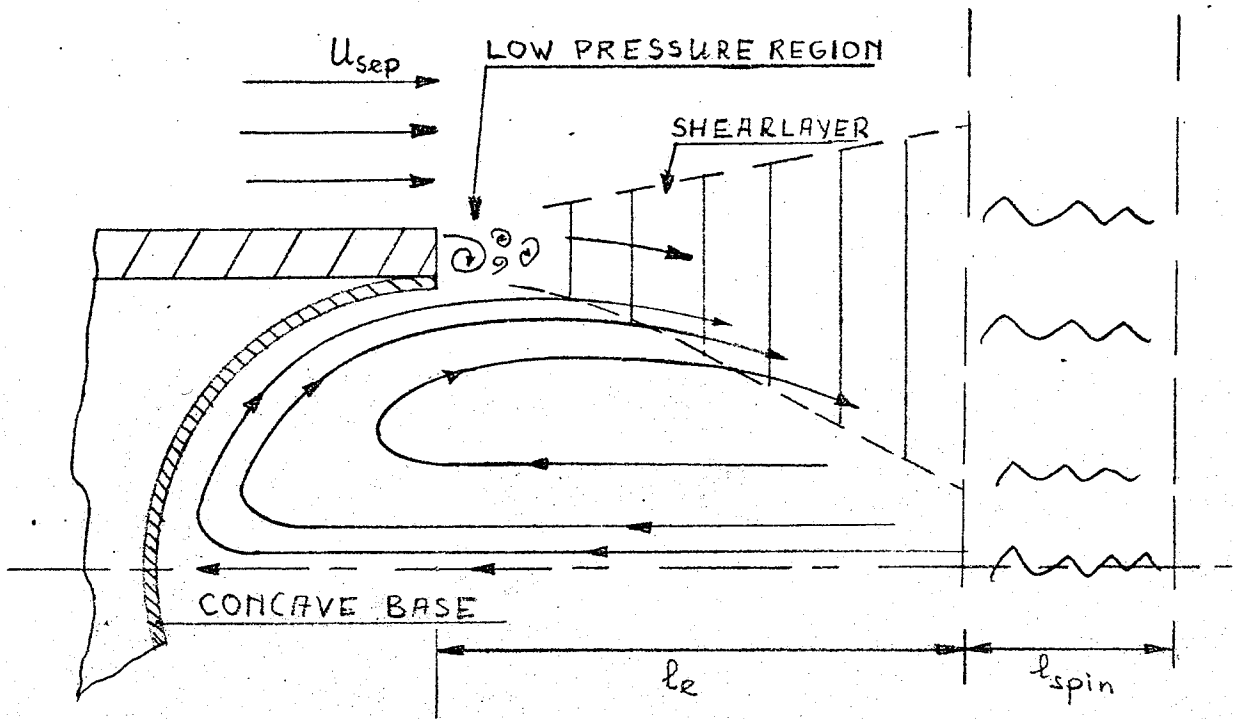


FIG. 53^a BLUNT TRAILING EDGE

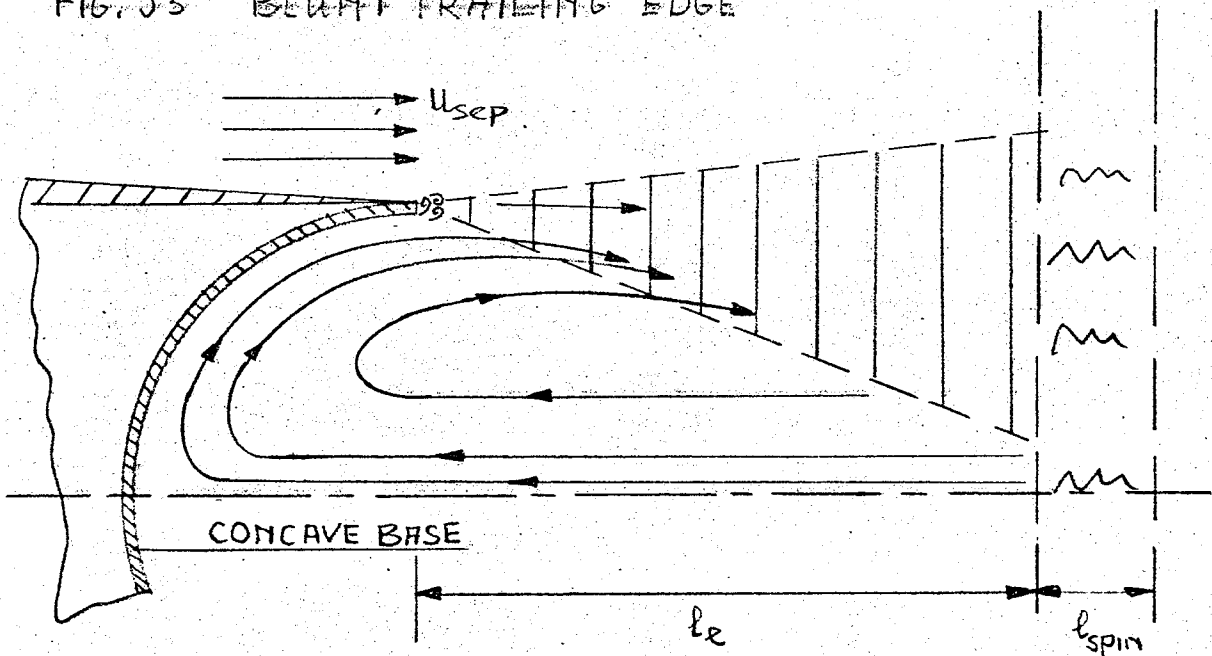


FIG. 53^b CHAMFERED TRAILING EDGE.

FIG. 53 FLOW PATTERN FOR A CONCAVE BASE.

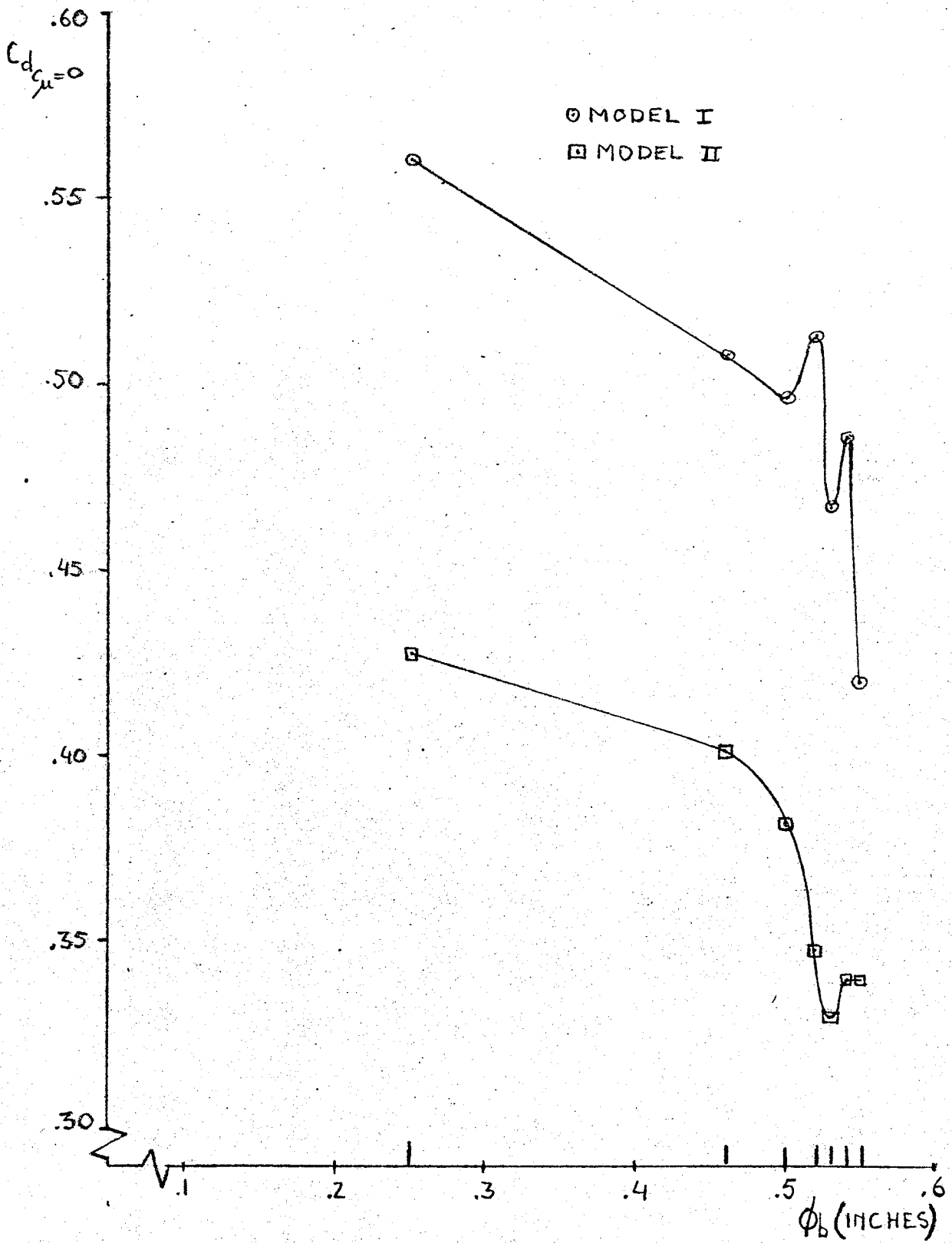


FIG. 54 VARIATION OF DRAG AT ZERO BLEED FOR SPINE CONFIGURATIONS.

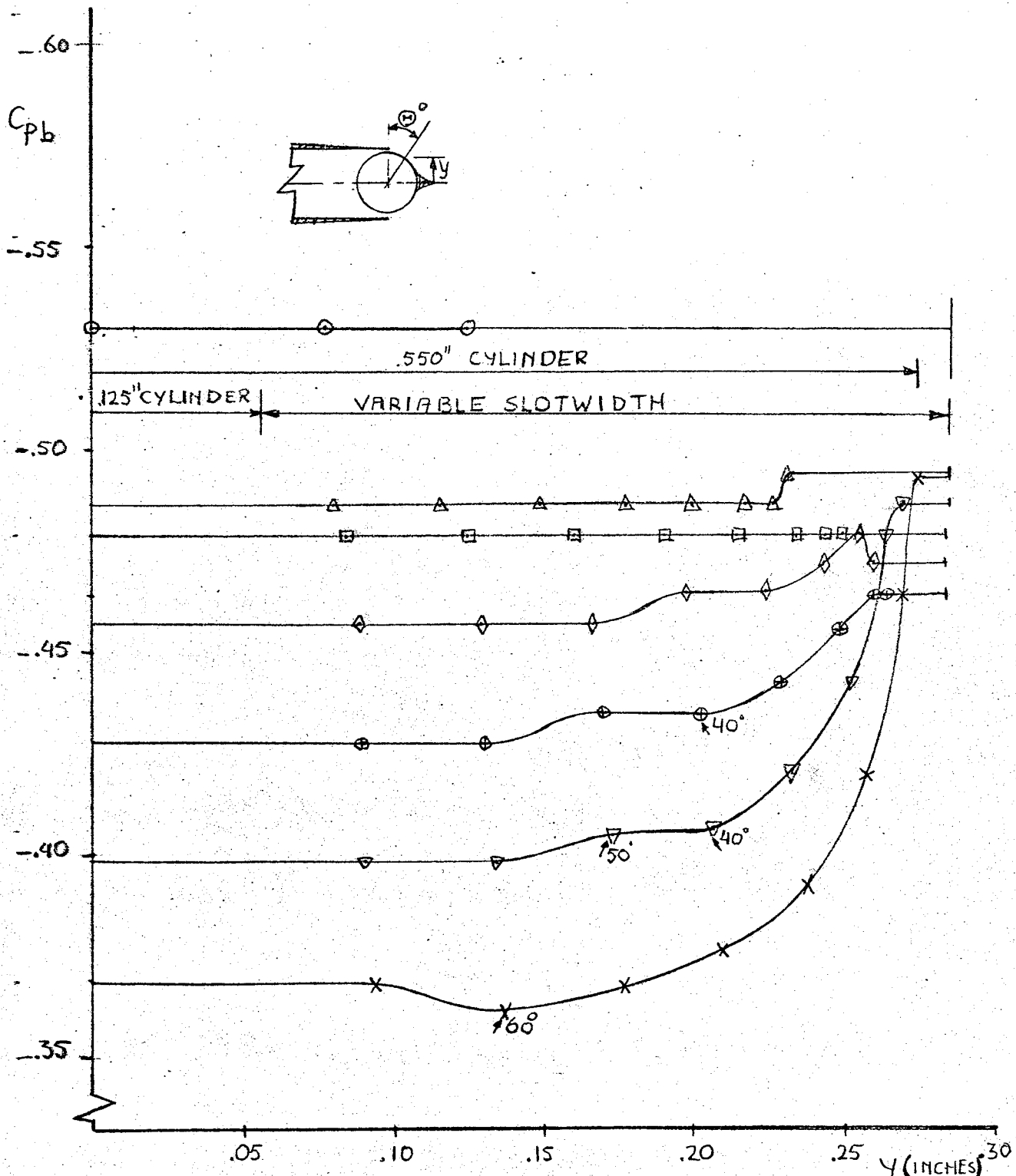


FIG. 55 BASE PRESSURE DISTRIBUTION FOR MODEL II WITH SPINES AT ZERO BLEED.

NOMENCLATURE AS FOR FIG. 51.

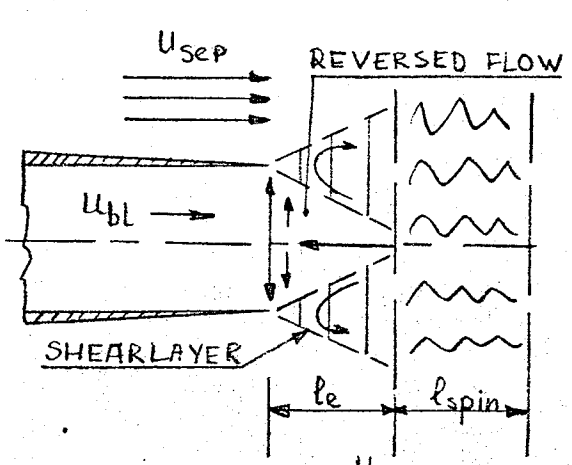


FIG. 56^a $C_\mu = 0, r = \frac{U_{bl}}{U_{sep}} = 0.0$

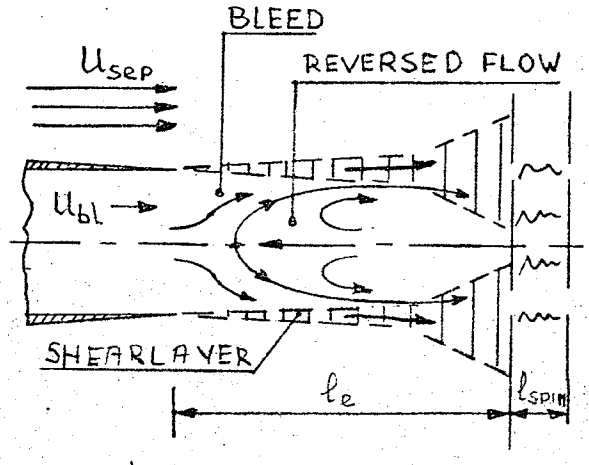


FIG. 56^b $C_\mu > 0.0, r > 0.0$

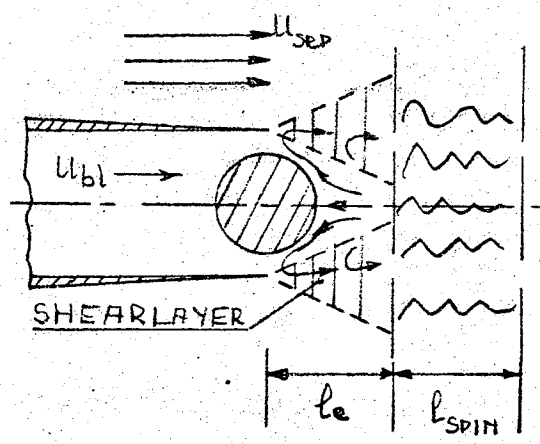


FIG. 56^c $C_\mu = 0.0, r = 0.0$

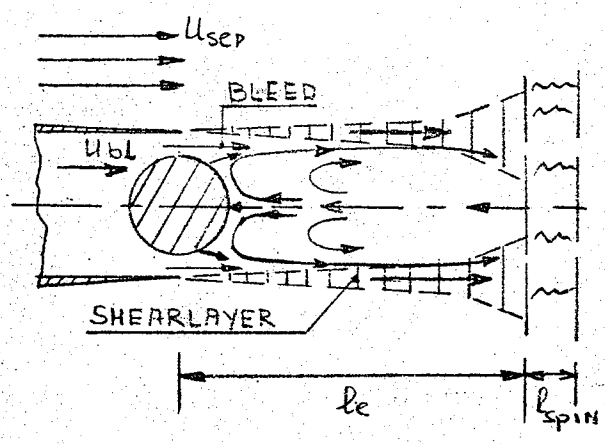


FIG. 56^d $C_\mu > 0.0, r > 0.0$

FIG. 56 THE EFFECT OF BLEED ON THE SHEAR LAYER DEVELOPMENT.

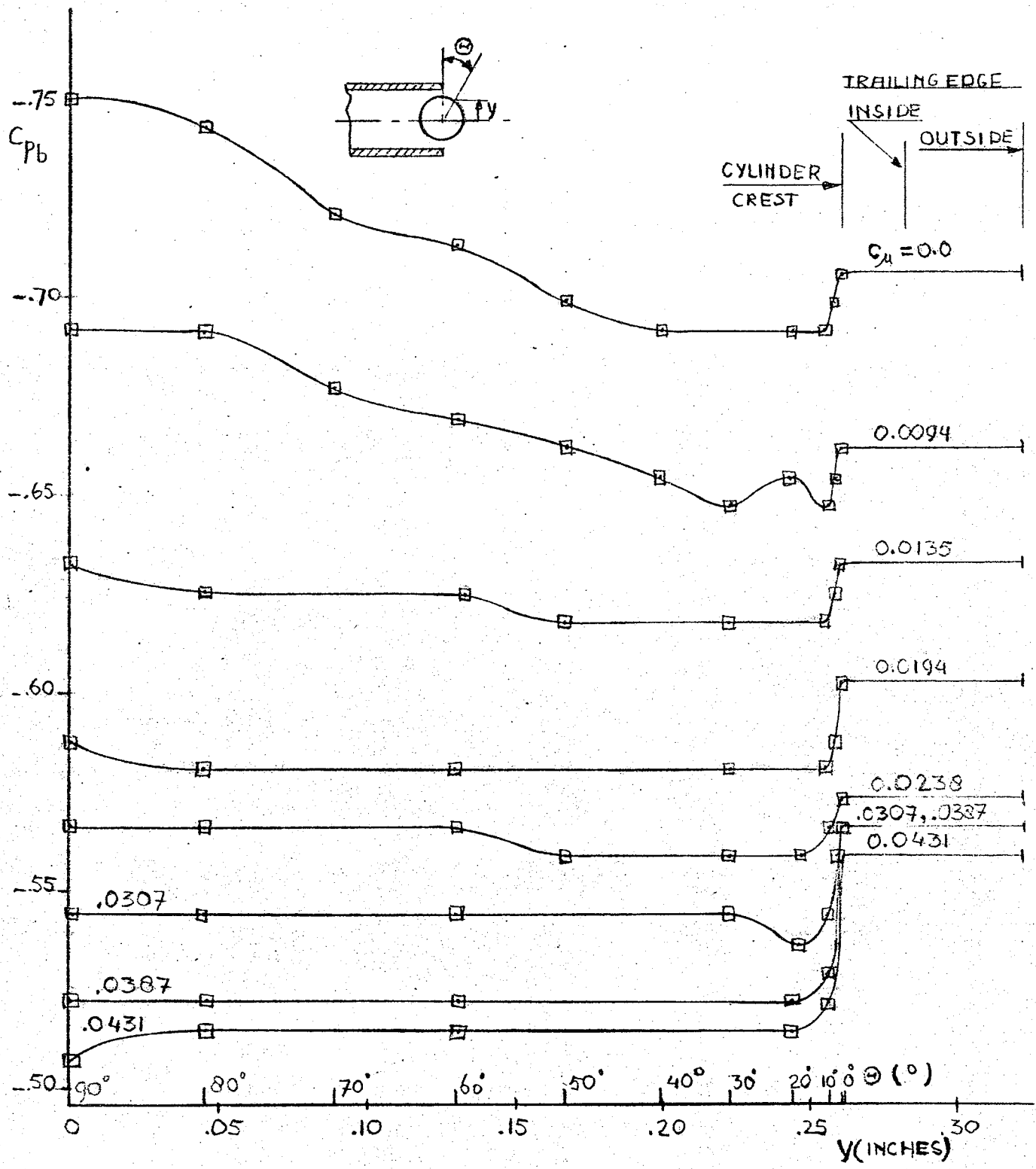


FIG.57 BASE PRESSURE DISTRIBUTIONS AT DIFFERENT BLEED RATES FOR MODEL I WITH $\phi_b = .520''$.

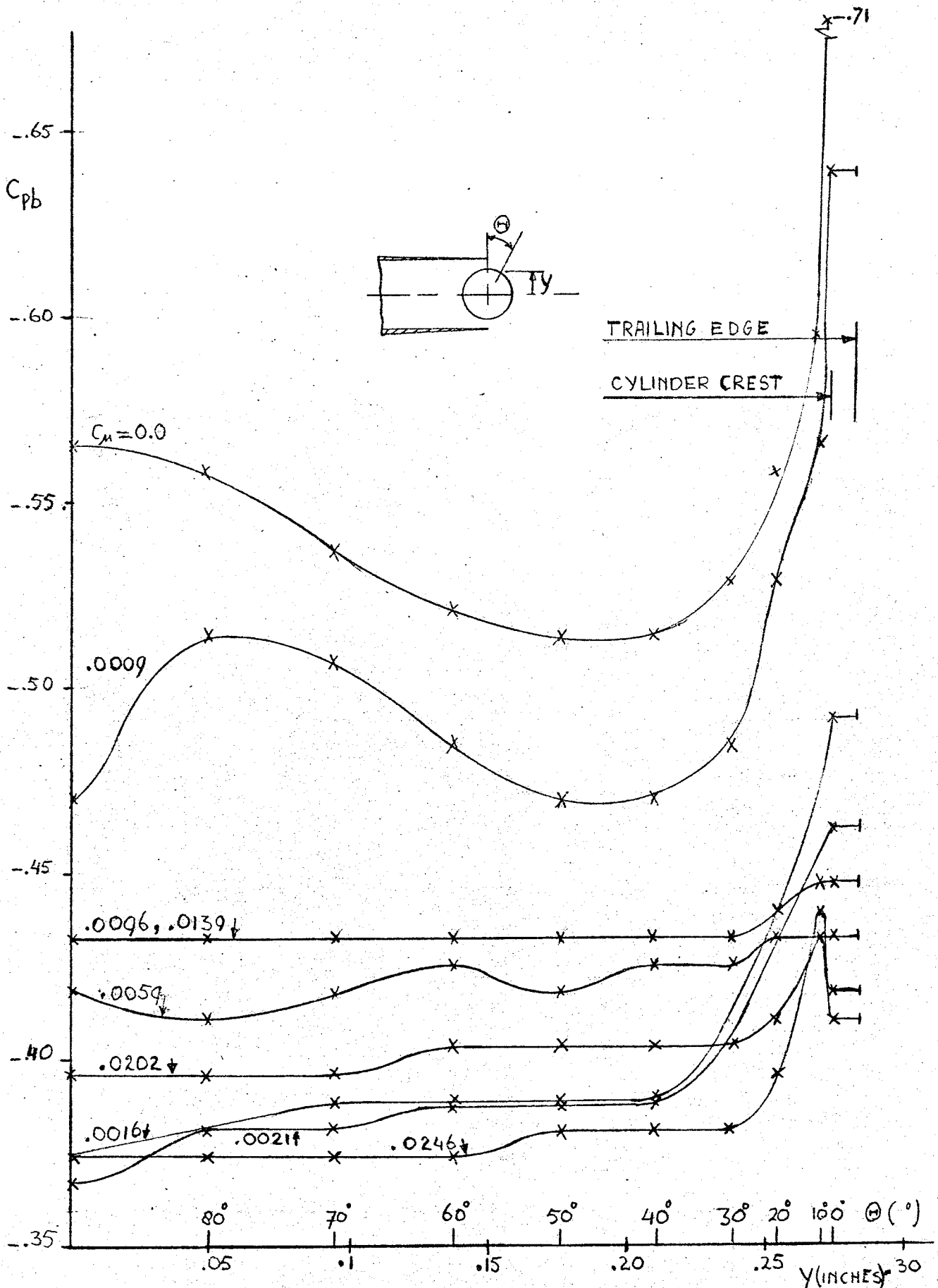


FIG. 58 BASE PRESSURE DISTRIBUTIONS AT DIFFERENT BLEED RATES FOR MODEL II WITH $\phi_b = .550$

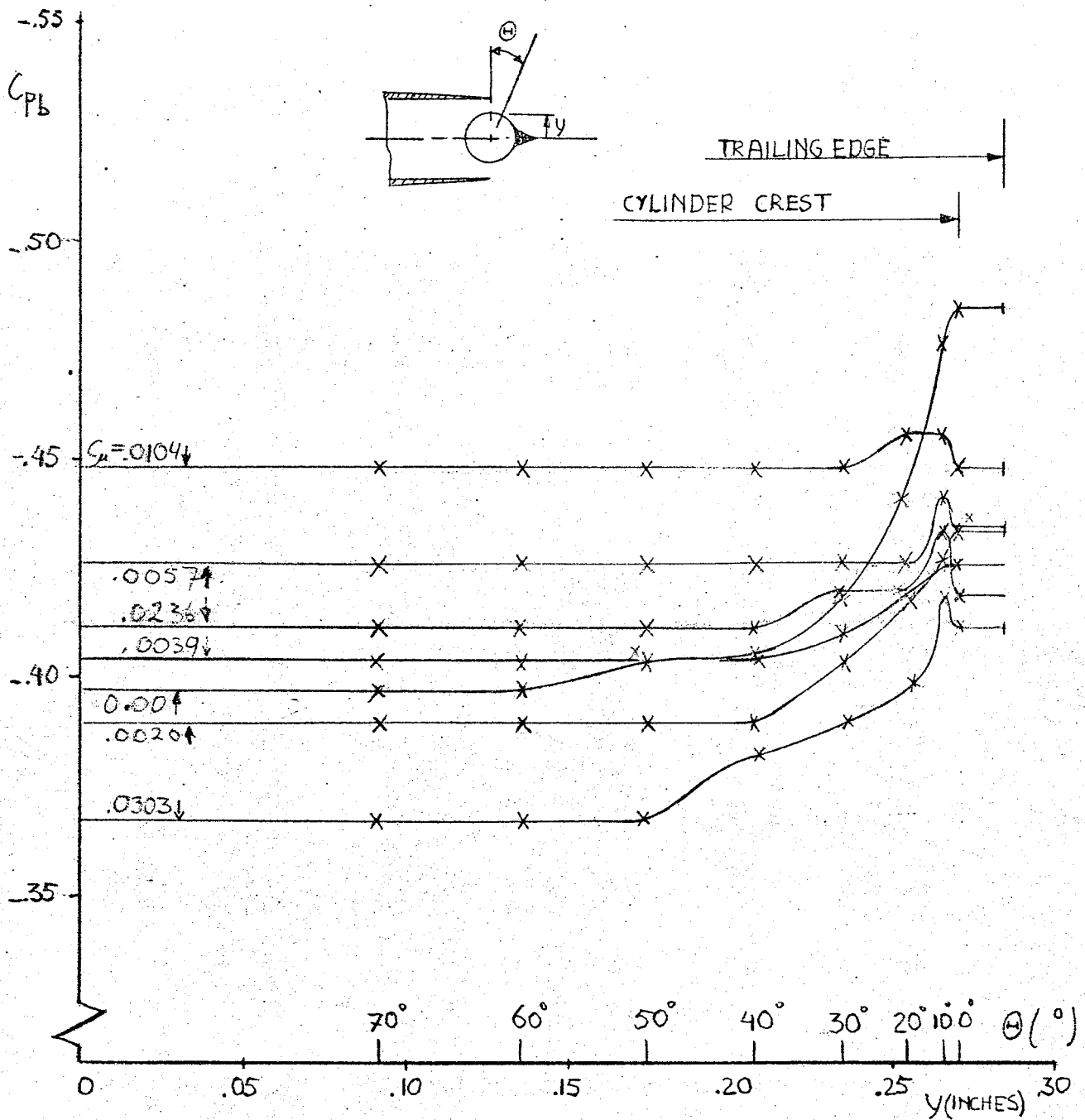


FIG.59 BASE PRESSUR DISTRIBUTIONS AT DIFFERENT BLEEDRATES FOR MODEL II, $\phi_b = .540$ " AND SPINE.